International Journal of Physical Sciences

Volume 9 Number 7 16 April, 2014
ISSN 1992-1950

Academic Journals

ABOUT IJPS

The **International Journal of Physical Sciences (IJPS)** is published weekly (one volume per year) by Academic Journals.

International Journal of Physical Sciences (IJPS) is an open access journal that publishes high-quality solicited and unsolicited articles, in English, in all Physics and chemistry including artificial intelligence, neural processing, nuclear and particle physics, geophysics, physics in medicine and biology, plasma physics, semiconductor science and technology, wireless and optical communications, materials science, energy and fuels, environmental science and technology, combinatorial chemistry, natural products, molecular therapeutics, geochemistry, cement and concrete research, metallurgy, crystallography and computer-aided materials design. All articles published in IJPS are peer-reviewed.

Contact Us

Editorial Office: ijps@academicjournals.org

Help Desk: helpdesk@academicjournals.org

Website: http://www.academicjournals.org/journal/IJPS

Submit manuscript online http://ms.academicjournals.me/.

Editorial Board

International Journal of Physical Sciences

Table of Contents: Volume 9 Number 7, 16 April, 2014

ARTICLES

academicJournals

Vol. 9(7), pp. 123-139, 16 April, 2014
DOI: 10.5897/IJPS2014.4108
Article Number: E60274244152
ISSN 1992 - 1950

http://www.academicjournals.org/IJPS

International Journal of Physical Sciences

Full Length Research Paper

Analysis of land development conformity obtained using photogrammetric and remote sensing methods with Geographic Information System (GIS) technology

Bogusława Kwoczyńska, Urszula Litwin, Bartosz Mitka*, Izabela Piech and Tomasz Salata

Faculty of Environmental Engineering and Land Surveying, Agricultural University in Krakow, Al. Mickiewicza 21, 31-120 Krakow, Poland.

Received 10 January, 2014; Accepted 24 February, 2014

Information regarding spatial management can be obtained using various methods, including satellite and photogrammetric technology. However, different methods give different results in terms of spatial resolution. Nowadays, photogrammetric data used for determining the spatial management usually employs pixels representing 0.25 m; still, the majority of the data are orthophotomaps with pixels representing 0.5 m; whereas the spatial resolution of most commonly used multispectral satellite images ranges from 20 to 30 m (for Landsat and SPOT satellites). This article presents the research results regarding the compatibility of spatial management descriptions based on photogrammetric and satellite sources. A supervised classification was conducted for two units, based on the multispectral satellite images. In this way, raster maps of spatial management were obtained. Also, vector maps of spatial management were made based on the orthophotomaps. Both kinds of description were integrated with each other in the GIS system by placing the data on separate layers. The compatibility analysis was conducted based on the analysis of two main layers representing the data obtained using the two methods. Due to the presence of raster and vector data, the value of each raster pixel was classified, and homogenous sets of data were obtained. The imaging, positioning and degree of generalization of the maps were compared, assuming parameters for the overlaying geometric objects, which was a sort of standardization.

Key words: Orthophotomaps, multispectral satellite images, image supervised classification, Geographic Information System (GIS) spatial analysis.

INTRODUCTION

Researches regarding the spatial management of both urban and rural areas have been conducted in Poland for many years. Most of them are propelled by various plans and designs that are meant to organize these areas. As years go by, the methods of data collection change as a result of access to new measurement and computer technologies. Spatial management data are most commonly collected from aerial photographs and their

*Corresponding author. E-mail: bartosz.mitka@ur.krakow.pl, Tel: +48 12 662 45 24. Fax: +48 12 662 45 03.

derivatives (the orthophotomaps) as well as from satellite images. However, different methods give different results in terms of spatial resolution. Photogrammetric products most commonly used for these purposes are orthophotomaps that have the spatial resolution of 0.25 m, while the images delivered by LANDSAT and SPOT satellites have spatial resolution ranging from 20 to 30 m. The use of orthophotomaps for many years has been very successful. It is a perfect solution providing topographical data for many users of various applications. It is current cartometric information about the area for use in managing and planning (Hsieh, 1996; Kerslen and O'Sullivan, 1996). In many countries, it became the basis for the creation of digital cadastral maps (Haumann, 1997; Triglav, 1998), and is now present on web geoportals at least as often as the topographic map; it is also a basic layer of information for Geographic Information System (GIS) (Pyka, 2009). Orthophotomap is also used to create tourist maps (enriched with information important for tourist purposes, such as location of monuments and churches, art galleries and museums, cinemas and theaters and public buildings; there are sketches of the most interesting tourist routes around the city) and the informative-tourist maps (applied to the planning and environmental monitoring, as well as the management of water resources for example, the creation of a water information system for monitoring the distribution of drinking water with integrated GIS using orthophoto, and also for optimization of business, industrial and service companies location) (Kerslen and O'Sullivan, 1996).

The aim of the study was to verify the results of supervised classification for public satellite imaging performed to extract the fundamental ways of land management. It was assumed that as the verification data will serve areas of management determined on the basis of orthophotomap vectorization, the authors of the study accepted the hypothesis, that such verification can be done using tools of the public GIS software packages operating under the Open Source license.

It should be noted that the aim of the elaboration was not to study the possibility of improving the spatial resolution of satellite images by integrating them with air imaging, but only a verification of the results obtained directly from satellite imaging on selected examples.

The following article presents the research on spatial management in two different settlement units- a rural and an urban one. This research allowed the authors to evaluate the compatibility of spatial data collected in different methods, using the GIS analytic tools.

METHODOLOGY

Characteristics of research objects

One of the researched objects was Kasinka Mala, in the community of Mszana Dolna (Figures 1 and 2), located in a valley, in the mountains of Beskid Wyspowy. Its area covers both the bottom of the valley, as well as its slopes. The diversity of terrain is the main factor contributing to its scenic qualities.

The next research object was Miechow, an urban unit (Figure 3). Miechow is a city located in southern Poland, in Malopolskie Voivodeship. It is the head of a rural and urban community in the Miechow District. Miechow has congested, in most cases low housing with dominating single family houses, while blocks of flats are in the minority. In the centre of town there is a medieval market square surrounded by historic buildings. Major parts of the community are arable lands.

Vectorization of utilized areas basing on an orthophotomap

In order to determine the utilized areas, an on-screen vectorization of the orthophotomaps was performed using Bentley Microstation V8i software, for three selected sheets of the orthophotomaps. Two of those sheets depicted the area of the Kasinka village. One of them showed the agricultural and wooded areas and the other covered the center of Kasinka, with typical rural housing. The third sheet covered the suburbs and a part of the center of Miechow. The sheets selected in this fashion represent various forms of spatial management in rural areas and small towns. All of the sheets have the resolution of 0.25 m per pixel, same DTM error used for creation of the orthophotomap equal to ±0.6 m and similar geometric precision of the orthophotomap of about 0.3 m. Thus, the data can be assumed to be homogeneous in terms of spatial precision and geometric resolution. However, the orthophotomaps of Kasinka involve colors, while for Miechow they are monochromatic. This results in possible differences in visual interpretation of green and agricultural areas. However, this fact is not relevant for the results, as for Miechow we are dealing mostly with urban and suburban areas, which involve an insignificant amount of agricultural lands. The characteristics of the source data taken from the Documentation Centre of Geodesy and Cartography (CODGIK) is shown below.

Characteristics of source data

For Kasinka area

Orthophotomap
Coordinate system: PUWG 1992
Module ID: M-34-77-C-c-3-1
Set ID: ORTO-M-34-77-C-c-3-1
Pixel size: 0.25 m
Date taken: 28.10.2009

Year of preparation of source materials:
Photos: 2009
Digital Terrain Model (DTM) Revised: October 2009

In order to generate the orthophotomaps, color aerial photos were employed. These were taken using the UltraCam Xp camera with the pixel size of 0.2 m. Also, the data obtained from aerotriangulation was used, which had been collected as a part of "Modernization and actualization of Land Parcel Identification System (LPIS) databases" project, for OB9.

The precision of the digital terrain model: ±0.6 m (for flat terrain with the average inclination <2°); ±0.9 m (for undulating and mountainous terrain).

Technology of orthophotomap creation: The orthophotomap was created using external orientation elements of the images, defined during aerotriangulation for a block, whose range corresponds to

Figure 1. Research area – Kasinka Mala. Source: Geoportal.gov.pl

Figure 2. Kasinka Mala. Source: own research.

Figure 3. Map of Miechow. Source: Geoportal.gov.pl

1:100 000 maps in Area 9.

Verification of geometric precision of the orthophotomap:
Number of points used: 16
Average error: 0.31 m

For the area of Miechow

Coordinate system: PUWG 2000
Module ID: 7.132.12.22
Set ID: 49/DEG/2004/2613_TBDORTO
Pixel size: 0.25 m
Date taken: 20.08.2004

Year of preparation of source materials:
Photos: 2004
DTM Revised: 2004

The map was generated using 1:13 000 images taken in March and April, 2003. The images were scanned with the pixel size of 14 µm. The map is also based on aerotriangulation data and DTM performed as a part of 49/DEG/2004/2613 project. The Digital Terrain Model precision is: ±0.6 m.

Technology of orthophotomap creation: The orthophotomap was created using external orientation elements of the images, defined during aerotriangulation for a block, whose range corresponds to a 5 LPIS object. The DTM in TTN structure covering the whole block was employed. The orthophotomap was created as a part of description covering the map sheets mentioned above. The orthorectification was performed using bilinear method in OrthoPro software. The tonal alignment was performed using PhotoShop, I/RAS C. Mosaicing and division into modules was performed in OrthoPro software.

Verification of geometric precision of the orthophotomap:
Number of used points: 5
Average error: 0.26 m

Determination of spatial management based on the orthophotomap

The following kinds of land use were defined:

i) Asphalt and dirt roads;
ii) Built-up areas;

iii) Waters;
iv) Forests, wooded areas
v) Areas covered with shrubs;
vi) Agricultural lands;
vii) Meadows, grasslands, green areas;
viii) Other areas

Vectorization was performed with the precision of ±1 pixel, which is equivalent to 30 cm in the researched area. Having in mind the terrain pixel of the satellite images, the areas determined using the orthophotomap can be used as a reference of precision of satellite image based classification. However, problems may occur during the photointerpretation of elements shown on the orthophotomap. Below, the most significant ones are listed.

i) Some of the borders between areas are not clear;
ii) High intensity of trees and shrubs obstructing the identification of the boundaries of areas under the crowns of trees and shrubs;
iii) Difficulty in distinguishing agricultural lands and grasslands because of the time in which the photos were taken.
iv) The radial movement of crowns of trees and roofs of buildings makes it difficult to identify the boundaries of areas - in particular, on the borders of dense forests;
v) The definition of a built-up area.

SATELLITE IMAGING IN SPATIAL MANAGEMENT EVALUATION

Color composite images

Supervised classification uses so-called "training fields" - selected parts of the image (their boundaries are defined in the form of a special vector file), which can be considered as representative for each category of land use, forming patterns of classes. This allows the interpreter "supervise" the course of the automatic classification process, based on all available information, acquired not only from the contents of the image, but also other sources (cartographic materials, aerial photos, text descriptions, field observations, etc). During classification for selected training fields and for each spectral ranges there are determined the main statistical parameters such, as: average, minimum and maximum values and additionally: standard deviation, variance and covariance. Then the image is analyzed, so that his every pixel is classified to the appropriate class.

The assignment of a pixel or group of pixels to a class (e.g. the deciduous forest) on the basis of the registration of only one channel (e.g. channel 1) is difficult or impossible. However, information on the second channel makes it easier to distinguish. Information from other channels increases the chance of correctly, automatically classifying the image contents. Therefore, supervised classification is the method that can be used to automatically carried out generalizations of the image according to the pattern adopted by the user.

There are three basic methods of classification:

a) The shortest distance method,
b) The maximum probability method,
c) The parallelograms method.

During the classification using the ‘shortest distance method,’ the pixel is assigned to the category for which the distance to the calculated mean value for the class is the smallest. However, the variability of pixel values for each class may vary significantly (for example the deciduous forest is characterized by high volatility and the desert areas by the low one), which means that there might arise errors in classification. To avoid this factor, so called standardized distances (normalized) are introduced, which are calculated by dividing distances from the mean by the standard deviation for a particular class.

During classification using the ‘maximum probability method’ for each pixel, the probability of belonging to each class is calculated and the pixel is assigned to the category for which the probability is the biggest. For each class, the average value and variance-covariance matrix are calculated which allows the assignment of the pixel to the class.

The fastest but also the least reliable method is the one that is virtually used only in didactics, the ‘method of parallelograms’. It consists in defining for each distinguished category and spectral range – the limits of the range of pixel values. For the analyzed two spectral channels, the pixels classified to the class must be found within the rectangle. When analyzing the three channels it will be a prism.

One of the most basic ways of getting information out of the measurement images is their direct interpretation. However, the image analysis and identification of the objects may be very time consuming. In order to make the process easier, and to allow getting more information out of the image, the image is saved in different spectral channels. Putting together three such images, saved in proper ranges of electromagnetic radiation, allows creating a color composite satellite image. The color composite images used in this study were created from three spectral extracts taken by Landsat 7 satellite using the multispectral scanner ETM+ in the years 2004 and 2009.

TM multispectral scanner records in seven spectral bands: four of these include the visible and near-infrared radiation, two - medium infrared range, one records the thermal radiation, thereby enabling the collection of information even in the dark. Imaging made with the scanner in the visible and near-infrared radiation have the resolving terrain power 30 × 30 m and allow the mapping of phenomena even in scale 1:25000, and terrain resolving power of infrared thermal radiation is 120 × 120 m (Mularz et al., 2000).

Color composite images are often used as the main source of information about an area. Despite their lower resolution when compared to panchromatic images, they are much more useful. The color composer images make the object recognition easier, due to their having colors and tones instead of shades of grey. Moreover, depending on the spectral ranges the composite image employs, other environmental objects of the area are exposed.

The composition of colour formed of channels 4, 5, 3 is primarily used to assess the vegetation areas coverage; it further emphasizes borders between regions used in different ways. A clear difference between the urban area and undeveloped ones can be observed. Moreover, we can clearly see the road network and development directions of urban space, differences in the layout and surface of arable land and permanent grasslands.

Channel 3 - detailed differentiation of vegetation
Channel 4 - distinguishing between surface waters
Channel 5 - estimating the moisture content in plants and soils.

Figures 4 and 5 present color composite images created using channels 4, 5 and 3. They are used mostly to distinguish between types of terrain coverage.

Classification of satellite image contents

The method of supervised classification of elements presented on the image allows a much greater interference of the user in the process of class creation. They are created by the user depending on the required precision, direction, and the goal of classification. This results from the fact, that in this method the pixels are assigned to the classes, and not the other way round. The principle

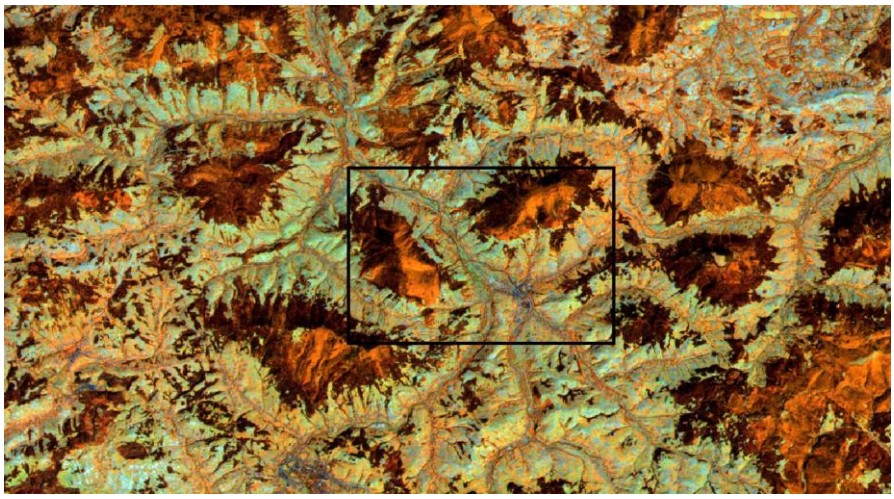

Figure 4. Color composite image created using the channels 4, 5 and 3, for the area of Kasinka Mala. Source: own research.

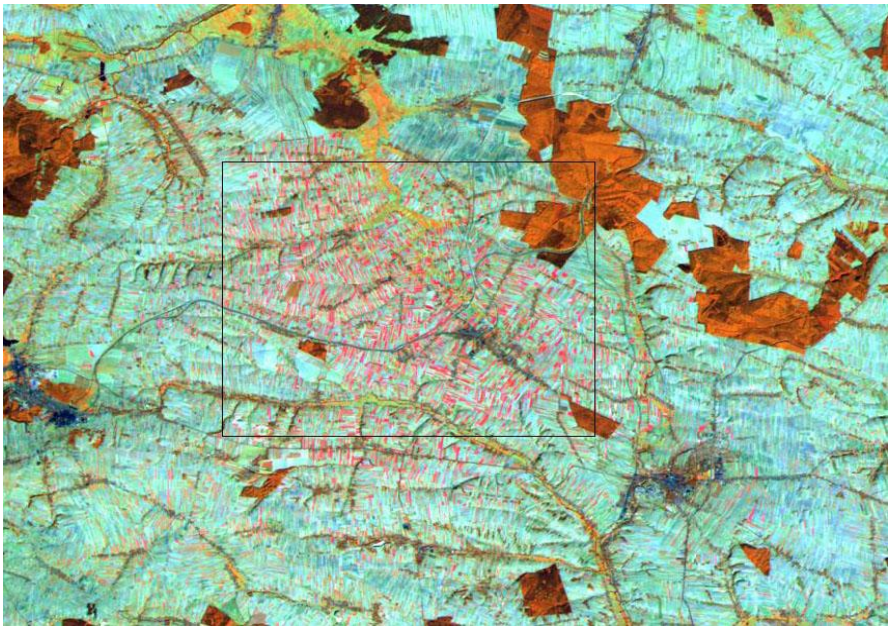

Figure 5. Color composite image created using the channels 4, 5 and 3, for the area of Miechow. Source: own research.

of this method is using the color composite image created using the least correlated channels to create the so called training fields. These are the areas that were chosen and assigned to particular classes. Thus, the supervised classification uses the terrain data in the process of class creation and assigning image elements to them.

The precision of classification depends mostly on the operator. The training fields must represent areas that are characteristic for particular kind of usage and should not contain elements assigned to another class. Thus, while selecting training fields, an area connected with a particular class should be selected with precision. After indicating the fields, statistical parameters were calculated and were later used in the process of classification. Every training field has an average value of brightness, standard deviation and also minimal and maximal value.

In order to obtain the most representative classification results, the number of classes was reduced to five. For Kasinka Mala area, the following areas were defined (Figure 6):

- Forests and wooded areas – green
- Green areas – brown
- Agricultural lands – yellow

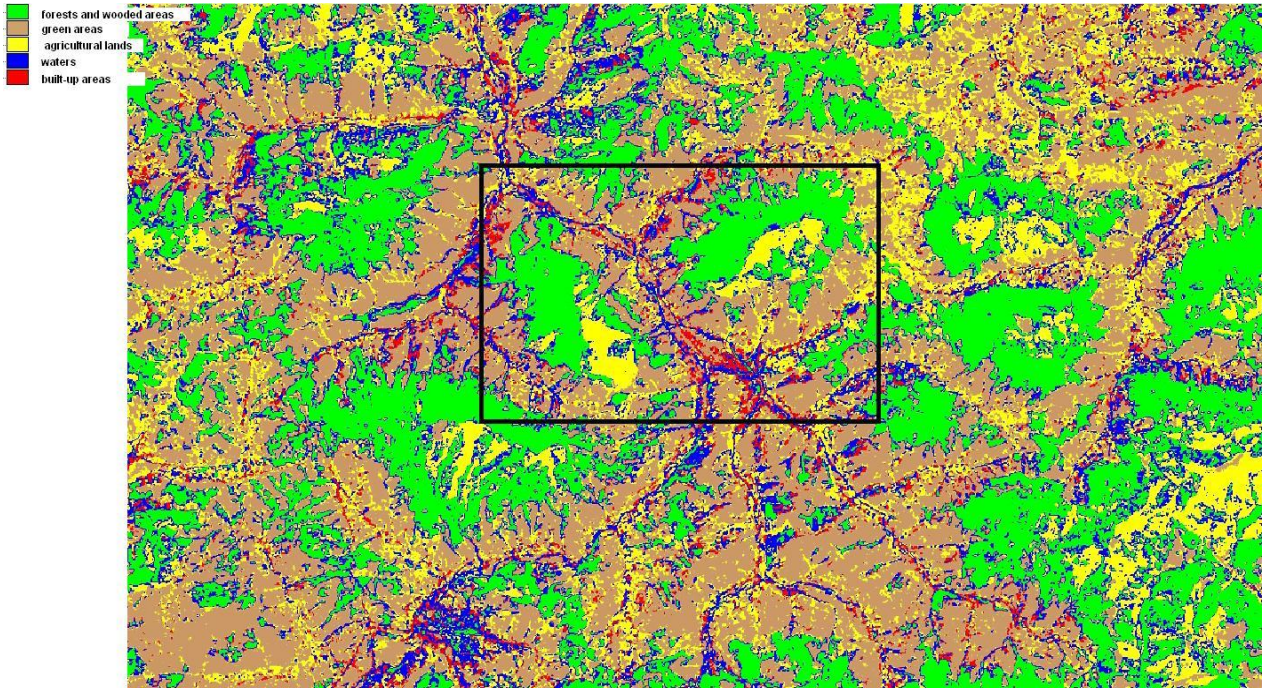

Figure 6. Supervised classification of Kasinka Mala. Source: own research.

Table 1. The list of numbers of pixels used in the study in Kasinka Mala.

Training fields	npix	Npixpct	pctnotund
Forests and wooded areas	8396181	13.88	23.29
Green areas	799229	1.32	2.22
Agricultural lands	7463547	12.34	20.70
Built-up areas	14748387	24.38	40.90
Waters	4649877	7.69	12.90

Source: own research.

- Waters – blue
- Built-up areas - red

Table 1 shows the list of numbers of pixels used in the definition of the training fields for supervised classification of the Kasinka Mala area.

In case of Miechow the following classes were defined (Figure 7):

- Forests and wooded areas – green
- Green areas – brown
- Agricultural lands – yellow
- Built-up areas – red
- Roads – black

There are four basic methods of conducting supervised classification: the parallelepiped method, the minimum distance method, the Mahalanobis distance method and maximum probability method (Eastman, 1992).

In the study area, several attempts of supervised classification were carried out using: the shortest distance, maximum probability and parallelograms methods. Satellite images from different time periods were used. For the selected areas (Kasinka Mala, Miechow), the shortest distance method gave the most promising results.

The minimum distance method was applied in the study. The spatial distribution of the pixels forms clusters that can be enclosed within an ellipse. Classes created in this way have different density and are created from the pixels of training fields described by the statistical parameters. The closer it is to the center of the class (ellipse), the higher the density. Also, the pixel brightness tends to the average value when going towards the center. During classification the pixels are analyzed in terms of Euclidean (geometric) distance from the centers of defined classes. The inspected element will be assigned to the nearest group. The distance is calculated from the formula (Adamczyk and Będkowski, 2005):

$$E_i = \sqrt{\sum_{j=1}^{N} (g_j - \mu_{ij})^2} \quad (1)$$

where: Ei – geometric distance of inspected pixel from the i^{th} class
N – number of classes
j – spectrum channel id
g – inspected pixel location
μ – i^{th} class center location

Supervised classification can also be the source of data regarding the spatial management of the Earth's surface. The freedom in class creation and the possibility of taking into account many terrain factors during classification is the main advantage of this method. Because of the simplicity of the process and relatively high precision of the results it is a good alternative for traditional

methods of satellite image interpretation. Supervised classification can be used in various stages of spatial planning, landscape architecture, investigating rate of change of urban areas, agricultural lands, forests, and many others.

APPLICATION OF THE SPATIAL DATA ANALYSIS METHOD

The aim of this stage was comparison of two layers obtained from the satellite and photogrammetric methods using geoprocessing tools from the GIS software. To perform the job, the whole software OpenSource was used: operating system OpenSUSE 12.1 and Desktop GIS including: Quantum GIS 1.7.4 and GRASS 6.4.

Comparison of the images originating from two sources could be performed under the condition of application of the same projection for different materials. In order to do this each photo was given an attribute EPSG of the projection and each photo was converted to the “2000” coordinates system (EPSG 2178) which is used in Poland for geodetic works (Figure 8).

Coordinate system “2000” for the whole geographic length is divided into four strips at intervals of 3° of length, which gives accuracy <7 cm on the edge of strips. After conversion, the images overlapped making the mosaic of lines, most often not overacting areas of similar use. It was necessary to convert to vector model, because in this model it is possible to link many descriptive attributes with each polygon representing the kind of land use (Coen, 2002; Hughes and Forsyth, 2006). For the orthophotomap, the vectorization was performed manually, while for color satellite image, values of pixels for all color channels were transformed to common feature value using the formula:

(sat_02@1*7+sat_02@2*17+sat_02@3*37+sat_02@4*53)/(sat_02@1 + sat_02@2 + sat_02@3 + sat_02@4) (2)

The formula had to join channels and preserve unique values of new pixels, therefore prime numbers were used as multiplier (Stones and Matthew, 2002), (Salata, 2008). Supervised classification of satellite image was performed in RGB colors, which caused pixels of particular color channels to have extreme values 0 or 255, so in numerator the value of any channel was multiplied by the prime number – the others were equal zero. Denominator was divided by total value of pixels in all channels of the raster. Thus, the image presented in Figure 9, in which values of pixels created groups corresponding with particular land use was obtained. The image was vectorized automatically in the next stage.

The next stage was automatic vectorization using functions enclosed in GRASS software, namely function „r.to.vect”:

r.to.vect [-svzbq] input=raster_*name* output=vector_*name* feature=*string* [--overwrite] [--verbose] [--quiet],

where parameters:
-s -- Smooth corners of area features
-v -- Use raster values as categories instead of unique sequence (CELL only)
-z -- Write raster values as z coordinate. Table is not created. Currently supported only for points.
-b -- Do not build vector topology (use with care for massive point export)
-q -- Quiet - Do not show progress
--overwrite -- Allow output files to overwrite existing files
--verbose -- Verbose module output
--quiet -- Quiet module output

After obtaining vector form with linked attributes table, which is a matrix of pixels values for areas of particular use, each area was assigned descriptive value: agricultural areas, waters, built-up, and so on. The talk is about areas, because adjacent pixels of the same value created one area, without borders inside (Figure 10).

At this stage it became possible to join thematic levels, their mutual analysis, multiplying objects situated on two layers. It became possible to separate areas which are unique in a scene of sum of sets of attributes for orthophotomap and satellite layers (Stones and Matthew, 2002). Each of separated areas possesses unique set of attributes, describing the land use way certified on the basis of orthophotomap and satellite image. Attributes were named „*_ortho" and „*_sat”, and they are products of consistent and inconsistent terrain functions. Presently, state area was calculated for each area and set together using application in Quantum GIS named GroupStat. Areas, where land uses are consistent have similar values of attributes, for example. „water_ortho”; „water_sat”; “buildings_ortho” and „buildings_sat”. Inconsistent configurations mean inaccuracy in interpretation of land use of areas by analyzed methods (Salata, 2012).

ANALYSIS OF COMPATIBILITY OF SATELLITE IMAGES WITH THE ORTHOPHOTOMAP BASED SPATIAL MANAGEMENT CLASSIFICATION

Because the geometric resolution of the orthophotomap is two orders of magnitude higher than the resolution of satellite images (0.30 m per pixel for the orthophotomap, 30 m per pixel for the satellite images), the spatial management obtained from the orthophotomap vectorization was taken as a reference for evaluation of the satellite image based classification.

For Kasinka area (rural area in mountainous terrain) the following results were obtained (Tables 2 and 3). Tabulation presented below presents inconsistencies in mutual interpretation of orthophotomaps and satellite imagery for each class obtained from the orthophotomaps. The decisive factor in the direction of the analysis is primarily much higher resolution of the air

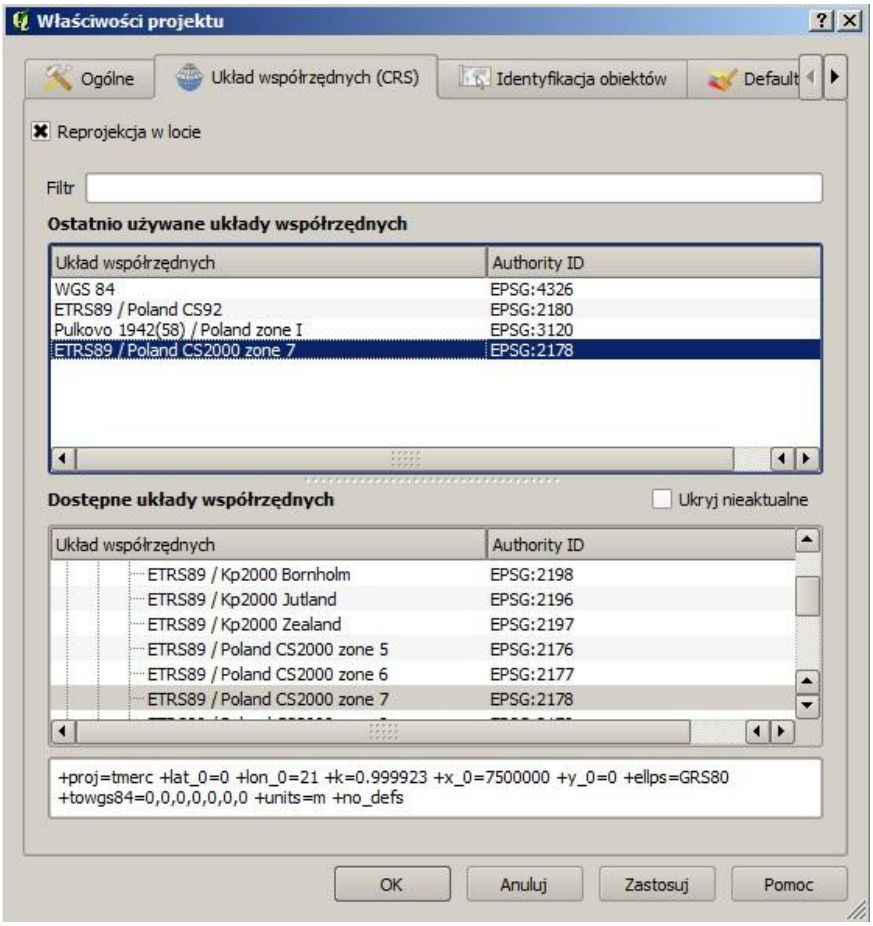

Figure 8. Choice and assignment of projection for layers in Quantum GIS program. Source: own research.

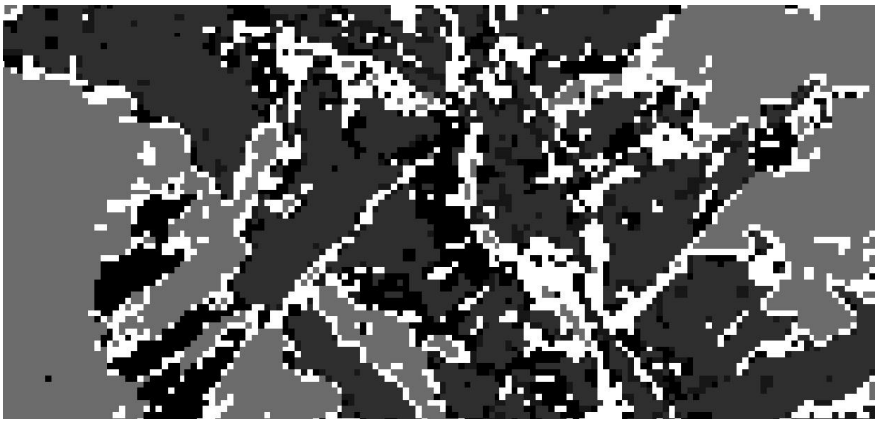

Figure 9. One channel image as an effect of joining color channels. Source: own research.

model, and also the possibility to determine a larger number of classes of land use. Presentation of Table 1 area approach should be more specific using the presentation of the percentages of selected non-compliances. Built-up areas in dispersed settlements do not reflect well on satellite imaging and are spread over

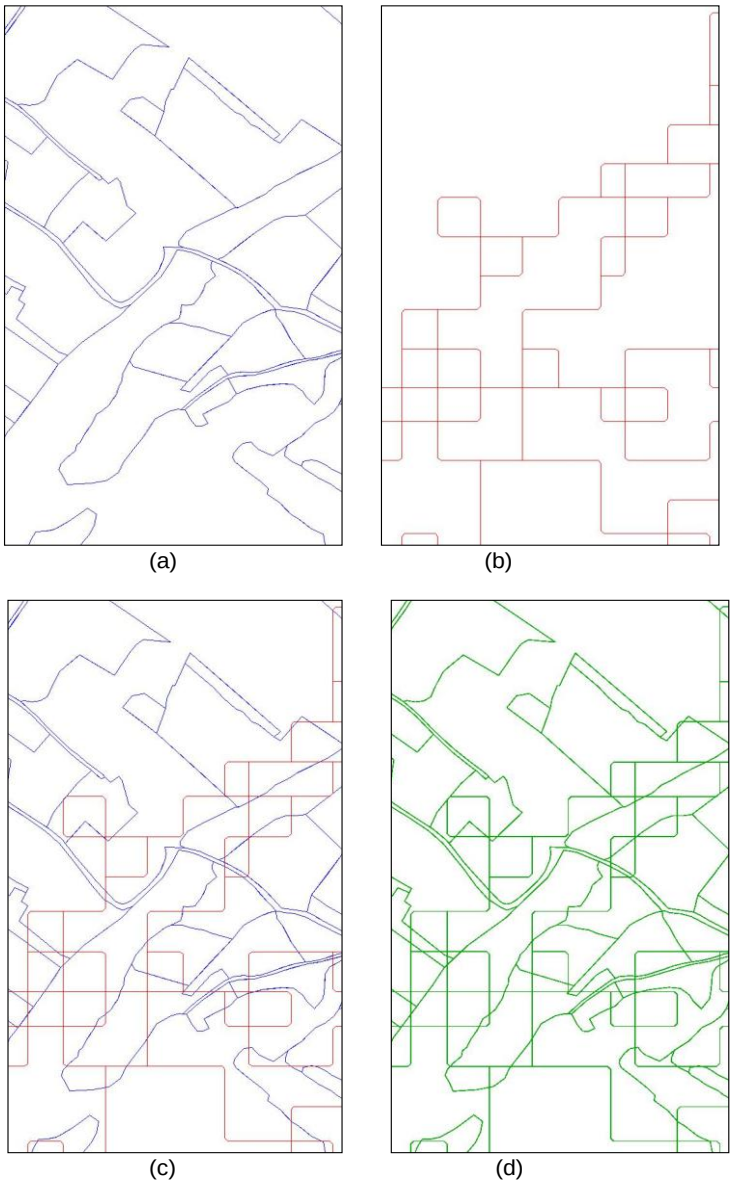

Figure 10. Methodology of spatial analysis performing: (a) Layer of vectorized orthophotomap, (b) Layer of vectorized areas classification on the basis of satellite image, (c) Overlapping layers from Figures a and b, and (d) Product of compared layers together with merging their attributes. Source: own research.

many classes marked with the suffix "_sat": buildings_sat (19.8%), forests_sat (0.9%), green_sat (32.0%), rural_sat (21.0%) and water_sat (26.4). Presentation of relative discrepancies in Figure 11, shows the areas where the interpretation should be as high as possible: "forests_ortho" ↔ "forests_sat" - compliance level 61.5%,"green_ortho" ↔ "green_sat" – low compliance level 33.3%, "rural_ortho" ↔ "rural_sat" - compliance level only 6.0%, "water_ortho" ↔ "water_sat" - compliance level 70.6%. On the examined object, some classes are also interpreted differently than one would assume. These are: agricultural areas interpreted in 80.8% as green areas, and green areas ("green_ortho") interpreted as: "water_sat" 29.0%, "rural_sat" - 14.4%, "green_sat" - 33.3%, "forests_sat" - 2.9% and "buildings_sat" - 20.3%. Linear features (roads) have been identified as scattered randomly and evenly over all satellite classes. Table 2 presents spatial data in terms of the absolute value of the surface in hectares. The table shows that areas with small-sized area, close to the limit

Table 2. Summary of areas (ha).

Classes	buildings_sat	forests_sat	green_sat	rural_sat	water_sat	Total	Portion %
Buildings_ortho	14.2093	0.6418	22.9972	15.0767	18.9442	**71.87**	**7.87**
Bushes_ortho	1.3301	1.1727	3.5742	2.4077	5.2757	**13.76**	**1.51**
Forests_ortho	4.9313	264.7488	7.4113	69.6986	83.8672	**430.66**	**47.16**
Green_ortho	1.5700	0.2235	2.5807	1.1168	2.2471	**7.74**	**0.85**
Roads_ortho	2.6742	0.0917	4.4129	2.6242	4.5034	**14.31**	**1.57**
Rural_ortho	11.8851	0.2273	125.6966	9.3724	8.4411	**155.62**	**17.04**
Wastelands_ortho	19.0366	2.4624	127.9011	30.5535	32.2640	**212.22**	**23.24**
Water_ortho	0.3594	1.1440	0.2881	0.2499	4.8990	**6.94**	**0.76**
Total	**56.00**	**270.71**	**294.86**	**131.10**	**160.44**	913.11	100.00
Portion %	**6.13**	**29.65**	**32.29**	**14.36**	**17.57**	100.00	

Source: Own research.

Table 3. Compatibility percentage for satellite classes.

Classes	Buildings_sat	Forests_sat	Green_sat	Rural_sat	Water_sat
Buildings_ortho	25.38	0.24	7.80	11.50	11.81
Bushes_ortho	2.38	0.43	1.21	1.84	3.29
Forests_ortho	8.81	97.80	2.51	53.16	52.27
Green_ortho	2.80	0.08	0.88	0.85	1.40
Roads_ortho	4.78	0.03	1.50	2.00	2.81
Rural_ortho	21.22	0.08	42.63	7.15	5.26
Wastelands_ortho	34.00	0.91	43.38	23.31	20.11
Water_ortho	0.64	0.42	0.10	0.19	3.05
Total	**100.00**	**100.00**	**100.00**	**100.00**	**100.00**

Source: Own research.

of satellite imaging resolution do not image there properly or do not at all, e.g. "roads_ortho" or "bushes_ortho" - the correctness of the interpretation of a few percent level. The increase in the surface of the compact area significantly improves efficiency of the imaging - the correctness of the interpretation at the level of 61.5% ("rural_ortho" ↔"rural_sat"). In Table 3, the color blue indicates classes of objects that should show the highest values of the coefficients of conformity in relative terms between them, but only forests proved to be clearly interpreted classes on two types of images: aerial and satellite. Red highlights definitely misclassified areas, and brown - classes ambiguous even in aerial photographs. These precise classes could take the high values, but remain at a level of 11.50 to 23.31% of satellite imaging incorrect classification. Analysis of the data above shows, that the compatibility between the orthophotomap and the satellite image is satisfactory only for forests (Figure 12).

Built-up areas were mainly in three kinds of land areas: housing, agricultural lands, and wastelands (in total 80.6% of the area classified as built-up). This is a result of scattered nature of housing in the area as well as the presence of fields and other non-built-up areas in very close neighborhood (Figure 13).

The areas classified on the satellite images as green areas are majorly agricultural lands and wastelands (together 86.0% of classified area). It happens, because the green areas are not much distinguishable from agricultural lands during vegetation period (Figure 14).

What is interesting for the area is the result of agricultural lands. Because of the mountainous terrain and the inclination of the slopes, large forests were classified as agricultural lands. This is an example of possible errors of the supervised classification algorithm, and a proof that the results need supervision (Figure 15). The result of water classification is also interesting (Figure 16). In the researched area, the border between the areas without trees and forests was classified as water. Also, the areas of low vegetation along roads and streams were assigned to this class. For the area of Miechow (urban area located on flat terrain) the following results were obtained (Tables 4 and 5). In Table 4 the list of overlapping areas with various methods of use is presented. To correctly interpret the list, analysis should

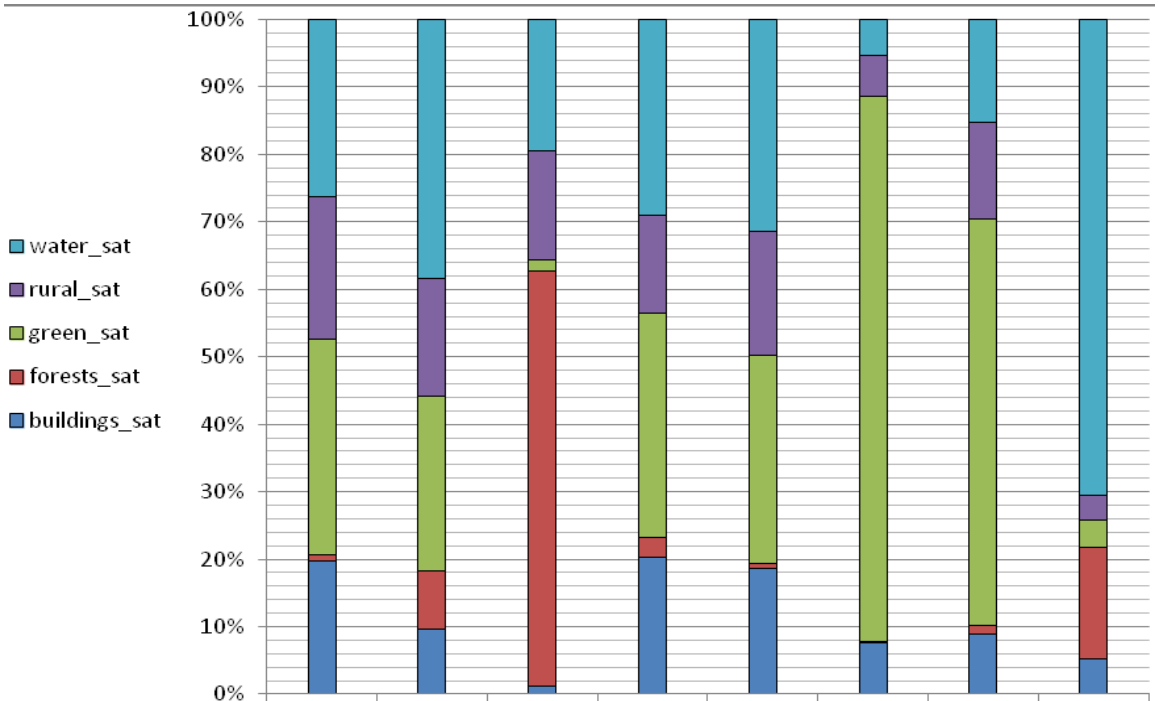

	buildings_ortho	bushes_ortho	forests_ortho	green_ortho	roads_ortho	rural_ortho	wastelands_ortho	water_ortho
water_sat	26.4%	38.3%	19.5%	29.0%	31.5%	5.4%	15.2%	70.6%
rural_sat	21.0%	17.5%	16.2%	14.4%	18.3%	6.0%	14.4%	3.6%
green_sat	32.0%	26.0%	1.7%	33.3%	30.8%	80.8%	60.3%	4.2%
forests_sat	0.9%	8.5%	61.5%	2.9%	0.6%	0.1%	1.2%	16.5%
buildings_sat	19.8%	9.7%	1.1%	20.3%	18.7%	7.6%	9.0%	5.2%

Figure 11. Relative compliance interpretation of classes use areas. Source: own research.

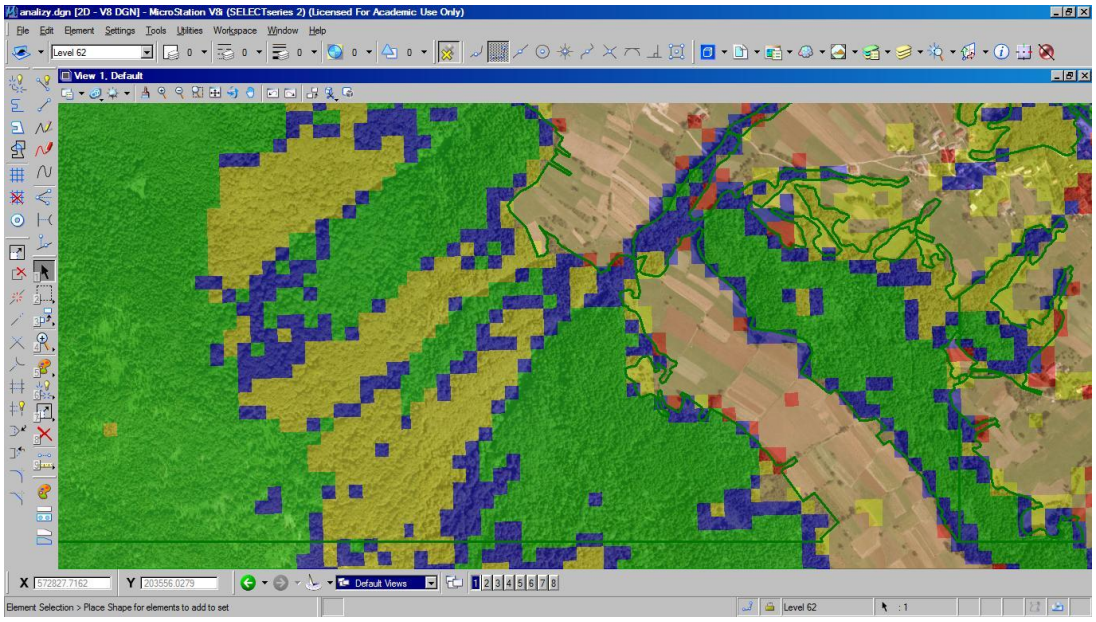

Figure 12. Compatibility of forest classification. Source: own research.

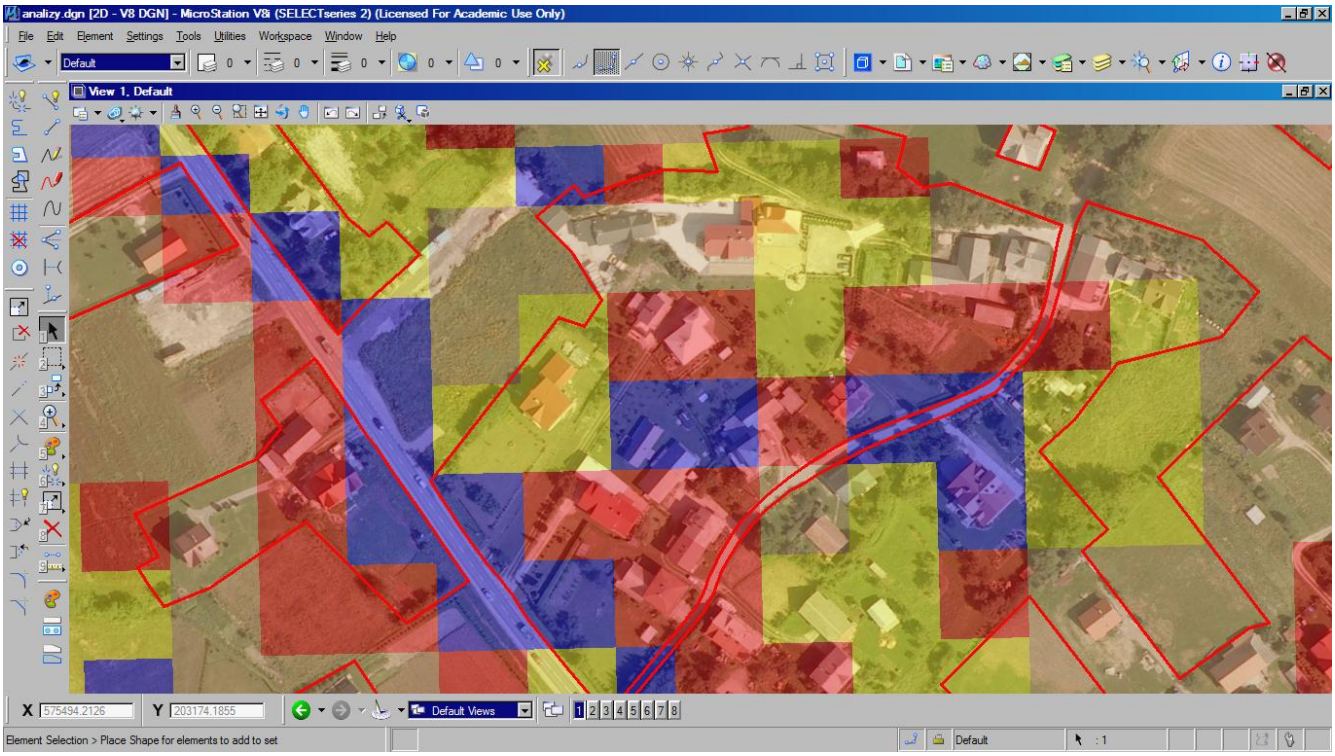

Figure 13. Compatibility of built-up area classification. Source: own research.

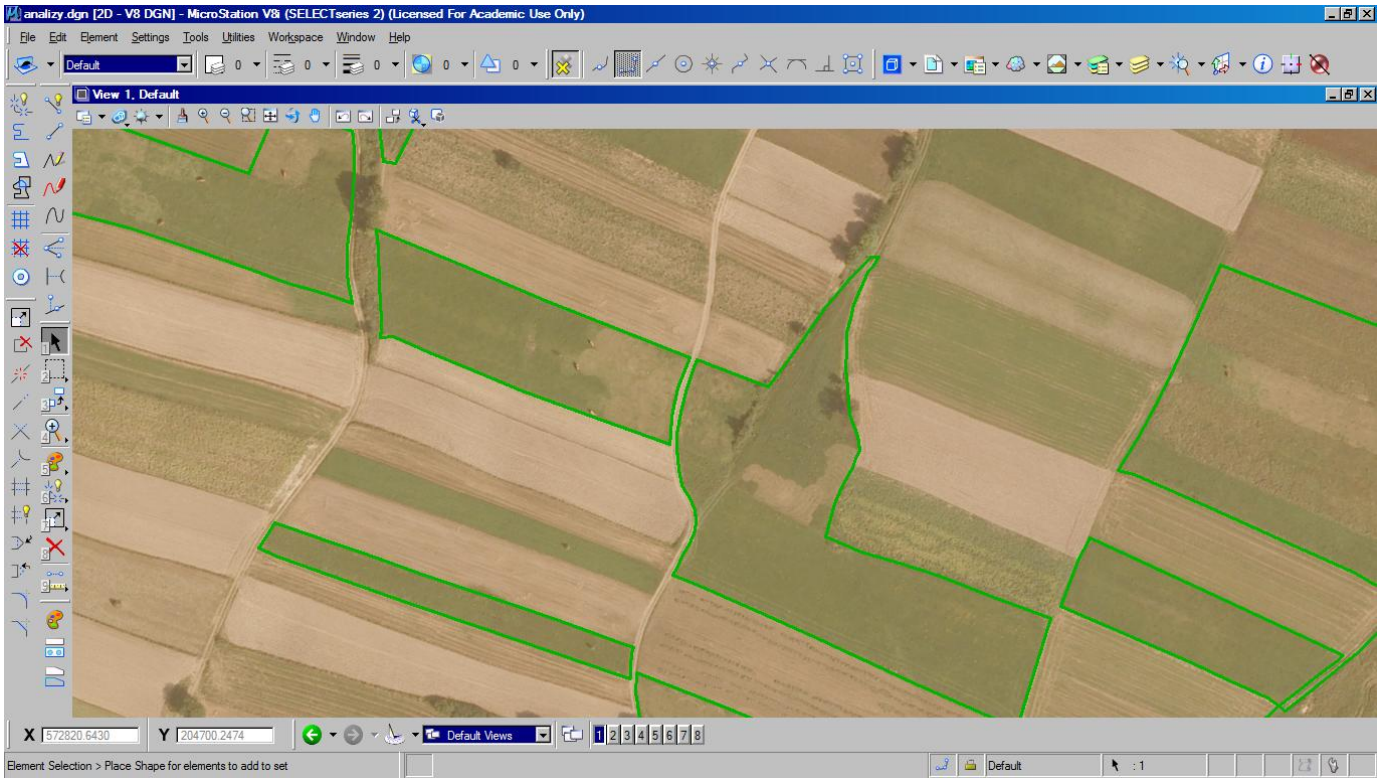

Figure 14. Compatibility of classification of green areas. Source: own research.

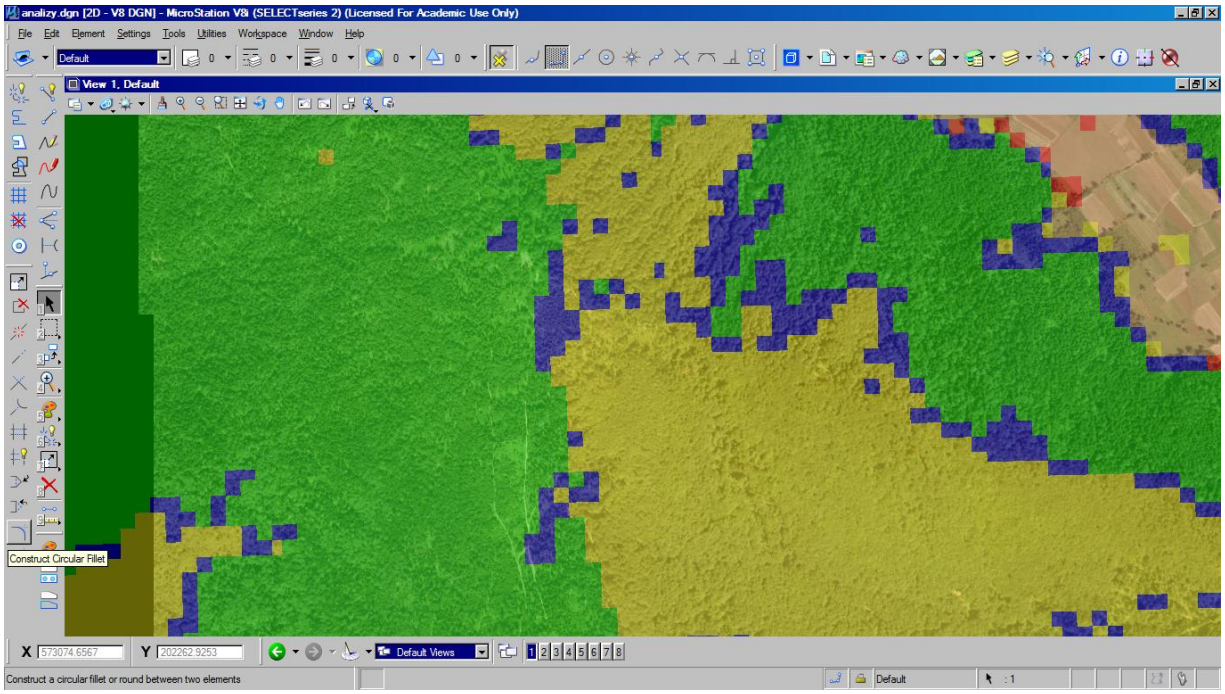

Figure 15. Compatibility of classification of agricultural lands. Misclassification of a forest as an agricultural land. Source: own research.

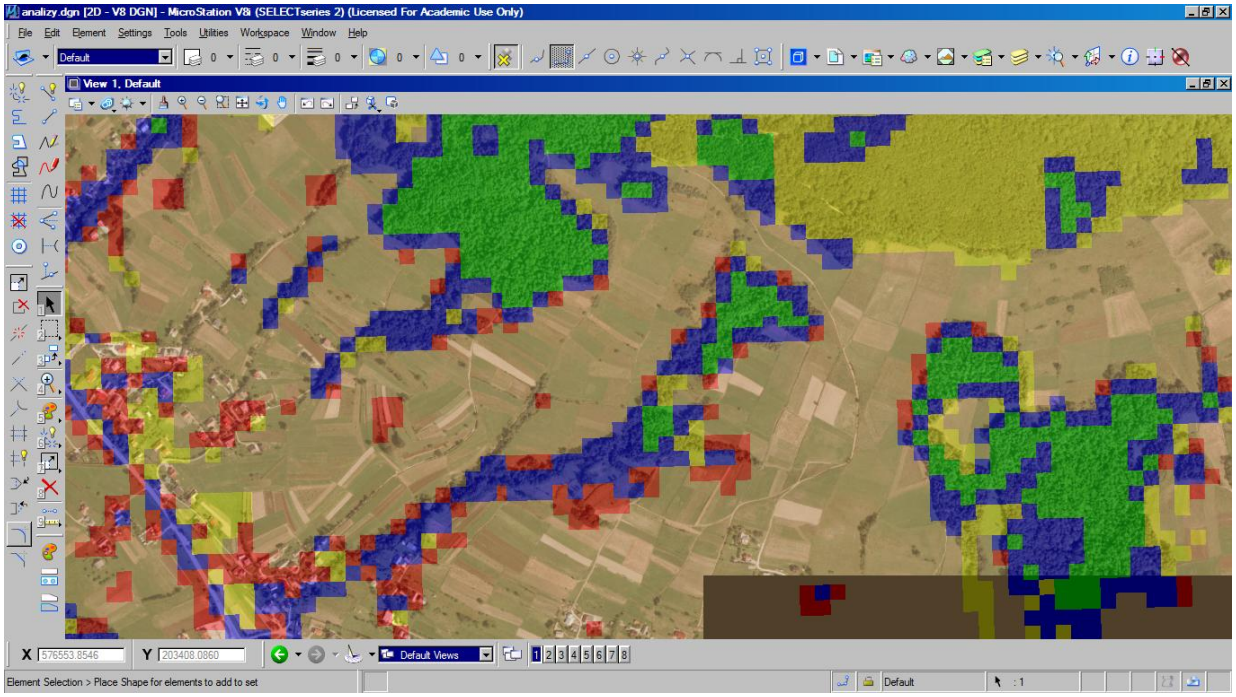

Figure 16. Compatibility of water classification. Source: own research.

be performed from the orthophotomap objects and areas covered on it. For two reasons: it is much more accurate (identification of the boundaries usage <1 m) and has more distinguishable classes. Satellite imaging has the

Table 4. Summary of areas (hectares).

Classes	Buildings_sat	Forests_sat	Rural_sat	Total	Portion %
Buildings_ortho	60.10	5.96	6.36	**72.42**	**45.31**
Bushes_ortho	2.51	1.02	0.57	**4.10**	**2.57**
Forests_ortho	1.76	0.11	0.02	**1.89**	**1.18**
Green_ortho	25.92	4.17	16.11	**46.20**	**28.90**
Roads_ortho	17.8	0.87	3.05	**21.72**	**13.59**
Rural_ortho	3.45	0.19	7.48	**11.12**	**6.96**
Wastelands_ortho	1.72	0.09	0.14	**1.95**	**1.22**
Water_ortho	0.32	0.12	0	**0.44**	**0.28**
Total	**113.58**	**12.53**	**33.73**	**159.84**	**100.00**
Portion %	**71.06**	**7.84**	**21.10**	**100.00**	

Source: own research.

resolution of 30 m, so in this case unilateral dependence of misinterpretation on the side of this material can be concluded.

The table presents the interpenetration of classes of built- up land uses determined in the table as "buildings_ortho" into three categories of satellite imaging, with the fact that the largest percentage (82.9%) accounted for the category labeled "buildings_sat" and areas "forests_sat" and "rural_sat" respectively 8.2 and 8.8% of the area. Areas covered with bushes are visible on the orthophotomap in more than half of the surface and distributed on satellite imaging to built-up areas (61.2%), forests (24.9%) and agricultural areas (13.9%). Forest areas in Miechow occupy a small area (1.89 ha),while almost all (93.1%) were classified as built-up areas on satellite imaging. The distribution of green areas on satellite imaging is as follows: 56.1% as "building_sat", 9.0% a "forests_sat" and 34.9% as "rural_sat". A similar situation exists for roads, wasteland and water - objects with a linear character – most often are interpreted as built-up areas "buildings_sat" respectively: 82.0, 88.2 and 72.7%. Agricultural areas on orthophotomap andsatellite imaging show interpretation compliance at the level of 67.3% and water areas in a high proportion (27.3%) are interpreted as "forests_sat".

Table 5 shows the matrix of relationships between the objects acquired from two sources: orthophotomap and satellite imaging blue color indicated theoretically the same nature of areas, with high relative compliance. For forest areas it takes a very low rate (8.8%), while the correlation is higher for built-up areas (52.91%) and poor for agricultural areas (22.18%). The color red indicates undesirable variation in the interpretation of test methods, namely: 47.57% of built-up areas (buildings_ortho) has been interpreted as forests (forests_sat), 18.86% as rural areas (rural_sat). Class "bushes_ortho", "roads_ortho" and "rural_ortho" are not directly visible in mapping satellite; therefore they were not marked in the table and are differently allocated to the classes of satellite imagery. Analysis of the data above shows, that the results were not satisfactory for any of the classes. This conclusion has been confirmed visually (Figure 17). Additionally, for the analyzed area there was no way of defining on the satellite images the remaining development classes marked on the orthophotomap.

Conclusions

Performing comparison by GIS methods, with application of geoprocessing and precise tools classifying areas on basis of the attribute tables enables quick and half automatic obtainment of quantitative data related to forms of land use. Based on the geometric models resulting from intersection of borders of similar classification, but using different methods, it became possible to gain analytic material, providing that comparison of effects of these methods is relevant.

Analytic accuracy is very high. Factors disturbing obtained accuracy are connected with mutual location of source data: orthophotomap and multispectral composition. The second aspect of performed analysis revealed the necessity of looking for adequate combination of channels and adjusting training fields for performing supervised classification. It turns out that for some areas (for instance forests) choice of channels set brings expected results, while for correct designation other forms of land use (covered with bush or wastelands) some other sets are needed.

Quantitative analysis shows, that bigger areas have a chance to have good reflection on satellite images, with pixel of dimension 30×30 m; then on the edges of those areas appear differences related to the location of the border and it depends on the size of pixel. On areas, where forms of land use are smaller than pixel dimension of satellite image, it is necessary to adjust set of channels from the composition after deep observation of land use based on orthophotomap.

Table 5. Compatibility percentage for satellite classes.

Classes	Buildings_sat	Forests_sat	Rural_sat
Buildings_ortho	52.91	47.57	18.86
Bushes_ortho	2.21	8.14	1.69
Forests_ortho	1.55	0.88	0.06
Green_ortho	22.82	33.28	47.76
Roads_ortho	15.67	6.94	9.04
Rural_ortho	3.04	1.52	22.18
Wastelands_ortho	1.51	0.72	0.42
Water_ortho	0.28	0.96	0.00
Total	**100.00**	**100.00**	**100.00**

Source: own research.

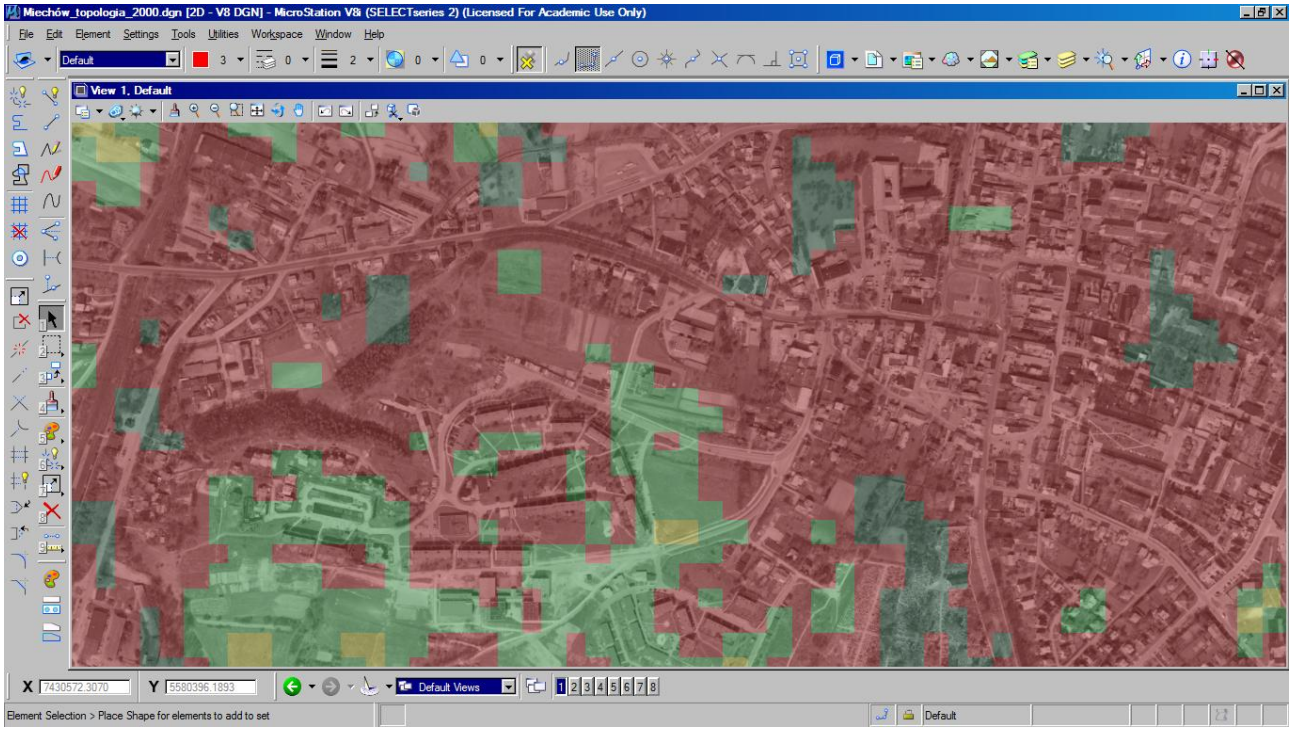

Figure 17. Results of supervised classification compared to the orthophotomap. Source: own research.

From the results, it can be concluded that high compatibility of satellite image based classification with the areas determined based on orthophotomap can be achieved only for forests. In other cases, the results diverged, which means the results supervised classification should be interpreted with caution, as they may be unreliable.

Conflict of Interests

The author(s) have not declared any conflict of interests.

REFERENCES

Adamczyk J, Będkowski K (2005). Digital methods in remote sensing. Publisher Agricultural University SGGW: 210-228.

Coen G (2002). Database Lexicography. Data and Knowledge Engineering 42. Boeing Phantom Works, Math. Comput. Technol. 293-314. http://dx.doi.org/10.1016/S0169-023X(02)00052-6, http://dx.doi.org/10.1016/S0169-023X(02)00052-6

Eastman JR (1992). IDRISI – Technical Reference. Clark University, Graduate School of Geography Worcester, USA.

Haumann DG (1997). The establishment of a multipurpose cadastre based on digital orthophoto techniques. All-Poland Symposium Modern orthophotography and GIS for the needs of land management.

Hsieh PY (1996). Development of digital ortophoto mapping. International Archives of Photogrammetry and Remote Sensing. XXXI(B4):368-372.

Hughes DA, Forsyth DA (2006). A generic database and spatial interface for the application of hydrological and water resource models. Comput. Geosci. 32:1389–1402. http://dx.doi.org/10.1016/j.cageo.2005.12.013, http://dx.doi.org/10.1016/j.cageo.2005.12.013

Kerslen T, O'Sullivan W (1996). Project Swissphoto – digital ortophotos for the entire area of Switzerland. International Archives of Photogrammetry and Remote Sensing. XXXI(B2):186-191.

Mularz S, Drzewiecki W, Pirowski T (2000). Merging Landsat TM images and airborne photographs for monitoring of open-cast mine area. Int. Archives Photogrammetry Remote Sensing. 33(B7):920-927.

Pyka K (2009). How to assess the photometric quality of the orthophotomap? Archiwum Fotogrametrii, Kartografii i Teledetekcji. 19:363-371.

Salata T (2008). Possibilities of the data interpretation in the databases Structures, AGH Electronic. J. Geomatics Environ. Eng. 2/2:81-86.

Salata T (2012). Implementation of geodesical measurement utilized for hydrological calculations, infrastructure and ecology of rural areas, Polish Academy of Sciences Cracow Branch, Commission of Technical Rural Infrastructure. 3/II:133-144.

Stones R, Matthew N (2002). Beginning Databases with Postgre SQL (Wrox Press 2001). Polish language edition by Helion.

Triglav J (1998). Slovenian approach to the geolocation of digital cadastral maps on the basis of digital orthophoto maps. Cadastral congress, Poland.

academicJournals

Vol. 9(7), pp. 140-145, 16 April, 2014
DOI: 10.5897/IJPS2013.4079
Article Number:63FC13844156
ISSN 1992 - 1950

http://www.academicjournals.org/IJPS

International Journal of Physical Sciences

Full Length Research Paper

On the Bishop curvatures of involute-evolute curve couple in E^3

Engin As and Ayhan Sarıoğlugil*

Department of Mathematics, Faculty of Science and Arts Ondokuz Mayis University, 55139-Kurupelit, Samsun, Turkey.

Received 24 November, 2013; Accepted 19 February, 2014

In this study, the relations between of the Bishop curvatures of involute-evolute curve couple were examined in E^3. Also, the relation between of the Bishop frames of these curves was given. Moreover, the relations between of curvature radii of these curves were investigated. Lastly, in the case of these curves were planar curves, some corollaries were obtained.

Key words. Bishop frame, Bishop curvatures, involute-evolute curve couple.

INTRODUCTION

The idea of a string involute is due to Christian Huygens (1658), who is also known for his work in optics. He discovered involutes while trying to build a more accurate clock (Boyer, 1968). The involute-evolute curve couple is a well-known concept in E^3 (Hacisalihoglu, 1995). The specific curve pairs are the most popular subjects in curve and surface theory and involute-evolute curve couple is one of them. We can see in most textbooks various applications not only in curve theory but also in surface theory and mechanics.

An evolute and its involute, are defined in mutual pairs. The evolute of any curve is defined as the locus of the centers of curvature of the curve. The original curves is then defined as the involute of the evolute. The simplest case is that of a circle, which has only one center of curvature (its center), which is a degenerate evolute. The circle itself is the involte of this point. There are extensive literature on this subject, for instance, Mustafa and Çalişkan (2002), Bükcü and Karacan (2007), Mustafa (2009), Boyer (1968), Hacisalihoglu (1995), and Turgut and Yilmaz (2008).

It is well-known that, if a curve differentiable in an open interval, at each point, a set of mutually orthogonal unit vectors can be constructed. These vectors are called Frenet frame or moving frame vectors. The rates of these frame vectors along the curve define curvatures of the curves. However, the Frenet-Serret frame is not defined for all points along every curve as curvature may vanish at some points on the curve; that is, second derivative of the curve may be zero. In this situation, we need an alternative frame. Therefore, in 1975, R.L. Bishop defined a new frame for a curve and he called it 'relatively parallel adapted frames' which is well defined even if the curve has vanishing second derivative in Euclidean 3-space. After Bishop's study, the ralatively parallel adapted frame have been called Bishop frame in other studies and also we will use the Bishop frame instead of the relatively parallel adapted frame. The advantages of Bishop frame

*Corresponding author. Email: sarioglugil@gmail.com

Mathematics Subject Classification: 53A04, 53A05.

and comparable Bishop frame with the Frenet frame in Euclidean 3-space were given by Bishop and by Hanson. After the invention of the Bishop frame, many studies were performed in Bükcü and Karacan (2008a, b, 2009), Andrew and Hui (1995), Bishop (1975), Yilmaz and Turgut (2010), and Yilmaz (2010).

In this paper, Bishop curvatures and curvatures radii of involute-evolute curve couple were obtained. The relations between Bishop curvatures and curvatures radii of these curve were computed and some results were given.

PRELIMINARIES

Let $\alpha: I \subset IR \to E^3$ be a differentiable curve with arc length parameter s and $\{t, n, b\}$ be the Frenet frame of α at the point $\alpha(s)$. These vectors are expressed by

$$t(s) = \alpha'(s), \quad n(s) = \frac{\alpha''(s)}{\|\alpha''(s)\|}, \quad b(s) = t(s) \wedge n(s)$$

where t, n and b are called tangent vector, principal normal vector and binormal vector, respectively. The Frenet formulas of α are

$$\begin{bmatrix} t' \\ n' \\ b' \end{bmatrix} = \begin{bmatrix} 0 & \kappa & 0 \\ -\kappa & 0 & \tau \\ 0 & -\tau & 0 \end{bmatrix} \begin{bmatrix} t \\ n \\ b \end{bmatrix} \quad (1)$$

Here κ and τ are called curvature and torsion of α (Hacisalihoglu, 1995).

Definition 1

Let α and β be two curves given by (I, α) and (I, β) coordinate neighbourhoods, respectively. Let Frenet frames of α and β be $\{t, n, b\}$ and $\{\bar{t}, \bar{n}, \bar{b}\}$, respectively. β is called the involute of α (β is called the evolute of α), if

$$\langle t, \bar{t} \rangle = 0.$$

Theorem 1

Let (β, α) be involute-evolute curve couple. Then, the relation between Frenet frames $\{t, n, b\}$ and $\{\bar{t}, \bar{n}, \bar{b}\}$ of α and β is given as follows, respectively:

$$\begin{bmatrix} \bar{t} \\ \bar{n} \\ \bar{b} \end{bmatrix} = \begin{bmatrix} 0 & 1 & 0 \\ cos\psi(s) & 0 & sin\psi(s) \\ -sin\psi(s) & 0 & cos\psi(s) \end{bmatrix} \begin{bmatrix} t \\ n \\ b \end{bmatrix}. \quad (2)$$

Here, ψ is angle between vectors t and $\bar{n}$ (Mustafa and Çalişkan, 2002).

Theorem 2

Let (β, α) be involute-evolute curve couple given by (I, α) and (I, β) coordinate neighbourhoods, respectively. Then,

$$d(\alpha(s), \beta(s)) = |c - s|$$

where, $\forall s \in I$ and $c = constant$ (Hacisalihoglu, 1995).

Theorem 3

Let (β, α) be involute-evolute curve couple and Frenet frames of α and β be $\{t, n, b\}$ and $\{\bar{t}, \bar{n}, \bar{b}\}$, respectively. Then, we have

$$\bar{\kappa}^2 = \frac{\kappa^2 + \tau^2}{\kappa^2 (c - s)^2}, \quad \bar{\tau}^2 = \frac{\kappa\tau' - \kappa'\tau}{\kappa(c - s)(\kappa^2 + \tau^2)}$$

Here, κ and τ are curvature and torsion of α and $\bar{\kappa}$ and $\bar{\tau}$ are curvature and torsion of β (Mustafa, 2009).

The Bishop frame (relatively parallel adapted frame) is an alternative approach to defining a moving frame that is well defined even when the curve has vanishing second derivative. We can parallelly transport an orthonormal frame along a curve by simply transporting each component of the frame parallelly. The parallel transport frame is based on the observation that, while t for a given curve model is unique, we may choose any convenient arbitrary basis (N_1, N_2) for the remainder of the frame, so long as it is in the normal plane perpendicular to t at each point (Yilmaz, 2010). Therefore, the type-1 Bishop (frame) formulas is expressed as

$$\begin{bmatrix} t' \\ N_1' \\ N_2' \end{bmatrix} = \begin{bmatrix} 0 & k_1 & k_2 \\ -k_1 & 0 & 0 \\ -k_2 & 0 & 0 \end{bmatrix} \begin{bmatrix} t \\ N_1 \\ N_2 \end{bmatrix} \quad (3)$$

Here, we shall call the set $\{t, N_1, N_2\}$ as Bishop frame and k_1 and k_2 as Bishop curvatures (Bükcü and Karacan, 2009; Bishop, 1975). The relation between Frenet and Bishop frames can be written as

$$\begin{bmatrix} t \\ n \\ b \end{bmatrix} = \begin{bmatrix} 1 & 0 & 0 \\ 0 & cos\theta(s) & sin\theta(s) \\ 0 & -sin\theta(s) & cos\theta(s) \end{bmatrix} \begin{bmatrix} t \\ N_1 \\ N_2 \end{bmatrix}. \quad (4)$$

Where

$$\theta(s) = acrtan\left(\frac{k_2}{k_1}\right), \quad (5)$$

$$\tau(s) = \theta'(s), \quad (6)$$

$$\kappa(s) = \sqrt{k_1^2 + k_2^2}. \quad (7)$$

Here, Bishop curvatures are defined by

$$\begin{cases} k_1 = \kappa cos\theta \\ k_2 = \kappa sin\theta \end{cases} \quad (8)$$

Definition 2

A regular curve $\alpha: I \to E^3$ is called a slant helix provided the unit vector $N_1(s)$ of α has constant angle θ with some fixed unit vector u; that is, $\langle N_1(s), u\rangle = cos\theta$ for all $s \in I$.

Theorem 4

Let $\alpha: I \to E^3$ be a unit speed curve with nonzero natural curvatures. Then α is a slant helix if and only if

$$\frac{k_1}{k_2} = const.$$

(Bükcü and Karacan, 2009).

ON THE BISHOP CURVATURES OF INVOLUTE-EVOLUTE CURVE COUPLE IN E^3

Let (β, α) be involute-evolute curve couple and Frenet frames of α and β be $\{t, n, b\}$ and $\{\bar{t}, \bar{n}, \bar{b}\}$, respectively. Let $\{t, N_1, N_2\}$ and $\{\bar{t}, \bar{N}_1, \bar{N}_2\}$ be Bishop frames of α and β, respectively. Moreover, let k_1, k_2 and $\bar{k}_1$, $\bar{k}_2$ be Bishop curvatures of α and β, respectively and κ and τ be curvature and torsion of α.

The relation between Frenet frame and Bishop frames of β is

$$\begin{bmatrix} \bar{t} \\ \bar{n} \\ \bar{b} \end{bmatrix} = \begin{bmatrix} 1 & 0 & 0 \\ 0 & cos\bar{\theta} & sin\bar{\theta} \\ 0 & -sin\bar{\theta} & cos\bar{\theta} \end{bmatrix} \begin{bmatrix} \bar{t} \\ \bar{N}_1 \\ \bar{N}_2 \end{bmatrix}.$$

Here, $\bar{\theta}$ is angle between vectors $\bar{n}$ and $\bar{N}_1$. By using the last equation and Equation (2), we obtain

$$\begin{bmatrix} t \\ n \\ b \end{bmatrix} = \begin{bmatrix} 0 & cos\psi cos\bar{\theta} + sin\psi sin\bar{\theta} & cos\psi sin\bar{\theta} - cos\bar{\theta} sin\psi \\ 1 & 0 & 0 \\ 0 & cos\bar{\theta} sin\psi - cos\psi sin\bar{\theta} & cos\psi cos\bar{\theta} + sin\psi sin\bar{\theta} \end{bmatrix} \begin{bmatrix} \bar{t} \\ \bar{N}_1 \\ \bar{N}_2 \end{bmatrix},$$

$$\begin{bmatrix} t \\ n \\ b \end{bmatrix} = \begin{bmatrix} 0 & cos(\psi - \bar{\theta}) & -sin(\psi - \bar{\theta}) \\ 1 & 0 & 0 \\ 0 & sin(\psi - \bar{\theta}) & cos(\psi - \bar{\theta}) \end{bmatrix} \begin{bmatrix} \bar{t} \\ \bar{N}_1 \\ \bar{N}_2 \end{bmatrix}$$

or

$$\begin{bmatrix} t \\ n \\ b \end{bmatrix} = \begin{bmatrix} 0 & \cos\sigma & -sin\sigma \\ 1 & 0 & 0 \\ 0 & sin\sigma & cos\sigma \end{bmatrix} \begin{bmatrix} \bar{t} \\ \bar{N}_1 \\ \bar{N}_2 \end{bmatrix}$$

Here, $\measuredangle(t, \bar{N}_1) = \sigma = \psi - \bar{\theta}$ and $\measuredangle(t, \bar{n}) = \psi$. Substituting Equation (4) into the last equation, we can write

$$\begin{bmatrix} 1 & 0 & 0 \\ 0 & cos\theta(s) & sin\theta(s) \\ 0 & -sin\theta(s) & cos\theta(s) \end{bmatrix} \begin{bmatrix} t \\ N_1 \\ N_2 \end{bmatrix} = \begin{bmatrix} 0 & \cos\sigma & -sin\sigma \\ 1 & 0 & 0 \\ 0 & sin\sigma & cos\sigma \end{bmatrix} \begin{bmatrix} \bar{t} \\ \bar{N}_1 \\ \bar{N}_2 \end{bmatrix}.$$

Then, the relation between Bishop frames of α and β is

$$\begin{bmatrix} t \\ N_1 \\ N_2 \end{bmatrix}. = \begin{bmatrix} 0 & cos\sigma & -sin\sigma \\ cos\theta & -sin\sigma sin\theta & -cos\sigma sin\theta \\ sin\theta & sin\sigma cos\theta & cos\sigma cos\theta \end{bmatrix} \begin{bmatrix} \bar{t} \\ \bar{N}_1 \\ \bar{N}_2 \end{bmatrix}. \quad (9)$$

From Figure 1,

$$\beta(\bar{s}) = \alpha(s) + \lambda(s)t(s) \quad (10)$$

for some function $\lambda(s)$. By taking the derivative of (10) with respect to s and applying the Bishop formulas, we have

$$\langle \bar{t}, t\rangle \frac{d\bar{s}}{ds} = (1 + \lambda')\langle t, t\rangle + \lambda k_1 N_1 + \lambda k_2 N_2.$$

Multiplying the last equation with t we get

$$\langle \bar{t}, t\rangle \frac{d\bar{s}}{ds} = (1 + \lambda')\langle t, t\rangle + \lambda k_1 \langle N_1, t\rangle + \lambda k_2 \langle N_2, t\rangle.$$

From the definition of the involute-evolute curve couple $\langle \bar{t}, t\rangle$, we obtain

$$\lambda = c - s, \quad c = constant \quad (11)$$

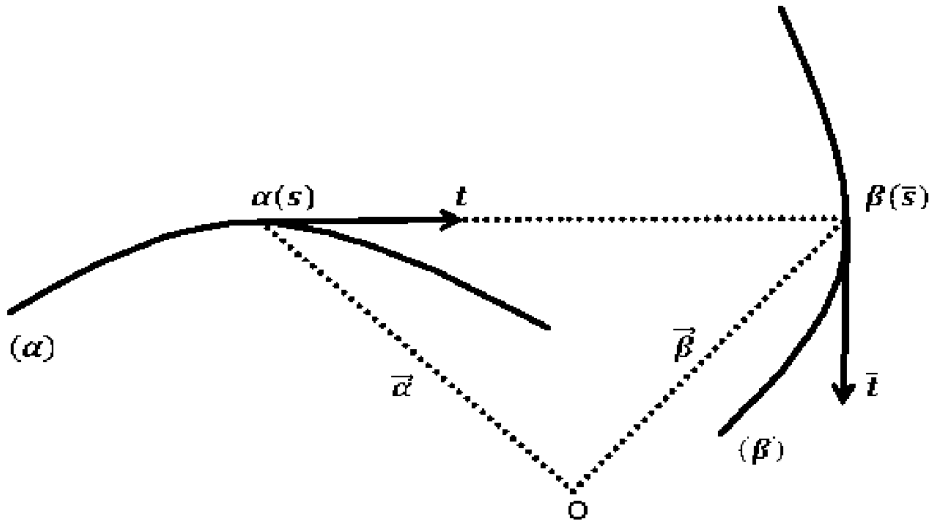

Figure 1. Involute-Evolute Curve Couple.

Then, from Equation (7) we can write

$$\bar{t}\frac{d\bar{s}}{ds} = \sqrt{k_1^2 + k_2^2}(c - s)n \tag{12}$$

Then, n and $\bar{t}$ are linearly dependent. Moreover, from Equation (2), we have

$$\frac{d\bar{s}}{ds} = \sqrt{k_1^2 + k_2^2}(c - s). \tag{13}$$

Theorem 5

Let (β, α) be involute-evolute curve couple. The relations between Bishop curvatures of α and β are given as follows:

$$\begin{cases} \bar{k}_1 = \dfrac{-cos\sigma\sqrt{k_1^2 + k_2^2} + \theta' sin\sigma}{(c - s)\sqrt{k_1^2 + k_2^2}} \\ \bar{k}_2 = \dfrac{-sin\sigma\sqrt{k_1^2 + k_2^2} + \theta' cos\sigma}{(c - s)\sqrt{k_1^2 + k_2^2}} \end{cases}$$

Proof

By taking the derivative of Equation (12) with respect to s, we have

$$\bar{t}\left(\frac{d\bar{s}}{ds}\right)^2 = \left[(c - s)\sqrt{k_1^2 + k_2^2}\right]' \tag{14}$$

By using the last Equations (1), (3), (6) and (13), we get

$$\bar{k}_1\bar{N}_1 + \bar{k}_2\bar{N}_2 = \frac{-1}{(c-s)^2(k_1^2+k_2^2)}\begin{bmatrix} (c-s)^2(k_1^2+k_2^2)t \\ +\dfrac{(k_1^2+k_2^2)-(k_1k_1'+k_2k_2')(c-s)}{\sqrt{k_1^2+k_2^2}}n \\ -(c-s)\theta'\sqrt{k_1^2+k_2^2}b \end{bmatrix}. \tag{15}$$

Multiplying the last equation with $\bar{N}_1$, we have

$$\bar{k}_1 = \frac{-cos\sigma\sqrt{k_1^2+k_2^2}+\theta' sin\sigma}{(c-s)\sqrt{k_1^2+k_2^2}} \tag{16}$$

Similarly, multiplying Equation (15) with $\bar{N}_2$, we have

$$\bar{k}_2 = \frac{-sin\sigma\sqrt{k_1^2+k_2^2}+\theta' cos\sigma}{(c-s)\sqrt{k_1^2+k_2^2}} \tag{17}$$

Thus, the following corollaries can be written.

Corollary 1

From Equations (16) and (17) it can be easily seen that

$$\bar{k}_1^2 + \bar{k}_2^2 = \frac{k_1^2+k_2^2+\theta'}{(c-s)^2(k_1^2+k_2^2)} \tag{18}$$

Corollary 2

From Equations (16) and (17), we can write

$$\tau = \theta' = (c-s)\sqrt{k_1^2 + k_2^2}\left(\bar{k}_1 sin\sigma + \bar{k}_2 sin\sigma\right),$$

$$\lambda = (c-s) = \frac{1}{-\bar{k}_1 cos\sigma + \bar{k}_2 cos\sigma}.$$

Corollary 3

If (β, α) is a planar curve, then we can write

$$\lambda = (c-s) = \pm\frac{1}{\sqrt{k_1^2+k_2^2}}. \quad (19)$$

Proof

From theorem 3, Equations (6) and (18) can be easily seen.

Theorem 6

Let (β, α) be involute-evolute curve couple. If α is a slant helix, then β is a slant helix⇔ σ = constant.

Proof

From theorem 4, Equations (8), (16) and (17), the proof is clear.

Theorem 7

Let (β, α) be involute-evolute curve couple. The relation between Bishop curvatures of α is

$$k_1^2 + k_2^2 = \frac{1}{2}(c-s)(k_1^2 + k_2^2)'. \quad (20)$$

Proof

Multiplying Equation (15) with $\bar{t}$, we have

$$k_1^2 + k_2^2 = (c-s)(k_1 k_1' + k_2 k_2')$$

and

$$k_1^2 + k_2^2 = \frac{1}{2}(c-s)(k_1^2 + k_2^2)'. \quad (21)$$

Corollary 4

Let (β, α) be involute-evolute curve couple. If α is a planar curve, then the relations between Bishop curvatures of α and β are

$$\left(\bar{k}_1^2 + \bar{k}_2^2\right)^{\frac{1}{2}} = \pm\frac{1}{2}\frac{(k_1^2 + k_2^2)'.}{k_1^2 + k_2^2}$$

Proof

From Equation (19) and (21), the proof is clear.

Theorem 8

Let (β, α) be involute-evolute curve couple and curvature radiuses of α and β be r and $\bar{r}$ at the points $\alpha(s)$ and $\beta(\bar{s})$, respectively. Then, the relation between r and $\bar{r}$ is given as follows:

$$\bar{r} = \frac{1}{r^2}\frac{|c-s|}{\sqrt{k_1^2 + k_2^2 + \theta'}}$$

Proof

Let M and $\bar{M}$ be curvature centers of α and β at the points $\alpha(s)$ and $\beta(\bar{s})$,, respectively. Then, we can write

$$r = \|\alpha M\| = \frac{1}{\kappa} = \frac{1}{\sqrt{k_1^2+k_2^2}} \quad (22)$$

$$\bar{r} = \|\beta\bar{M}\| = \frac{1}{\bar{\kappa}} = \frac{1}{\sqrt{\bar{k}_1^2+\bar{k}_2^2}}. \quad (23)$$

Substituting Equation (18) into Equation (23), we get

$$\bar{r} = \frac{|c-s|(k_1^2 + k_2^2)}{\sqrt{\bar{k}_1^2 + \bar{k}_2^2 + \theta'}}.$$

From Equation (22), we obtain

$$\bar{r} = \frac{1}{r^2}\frac{|c-s|}{\sqrt{k_1^2+k_2^2+\theta'}} \quad (24)$$

From Equations (6) and (24), the following corollary can be given.

Corollary 5

Let (β, α) be involute-evolute curve couple. If α is a planar curve, then the relation between curvature radii of α and β are

$$\bar{r} = \frac{1}{r}|c-s|.$$

Conflict of Interests

The author(s) have not declared any conflict of interests.

REFERENCES

Andrew JH, Hui M (1995). "Parallel Transport Approach To Curve Framing", Indiana University,Techreports- TR425, January 11.

Bishop RL (1975). There is more than one way to frame a curve. Am. Math. Monthly, 82(3):246-251. http://dx.doi.org/10.2307/2319846

Boyer C (1968). A History of Mathematics, New York: Wiley.

Bükcü B, Karacan MK (2007). On the ınvolute and evolute curves of the spacelike curve with a spacelike binormal in Minkowski 3-Space. Int. J. Math. Sci. 2(5):221-232.

Bükcü B, Karacan MK (2008a). On the slant helices according to Bishop frame of the timelike curve in Lorentzian Space, Tamkang. J. Math. 39:255-262.

Bükcü B, Karacan MK (2008b). Special Bishop motion and bishop darboux rotation axis of the space curve. J. Dyn. Syst. Geom. Theor. 6(1):27-34.

Bükcü B, Karacan MK (2009). The slant helices according to Bishop Frame. Int. J. Comput. Math. Sci. 3(2):67-70.

Hacisalihoglu HH (1995). "Differential Geometry I", Ankara University, Faculty of Science and Arts Publications, Ankara.

Mustafa B, Çalişkan M (2002). Some Characterizations for the pair of ınvolute-evolute curves in euclidean space E^3, Bulletin. Pure Appl. Sci. 21E(2):289-294.

Mustafa B (2009). On the timelike or spacelike ınvolute-evolute curve couples, Samsun, Doctorate Thesis.

Yilmaz S, Turgut M (2010). A new version of Bishop frame and an application to spherical ımages. J. Math. Anal. Appl. 371:764-776. http://dx.doi.org/10.1016/j.jmaa.2010.06.012, http://dx.doi.org/10.1016/j.jmaa.2010.06.012

Yilmaz S (2010). Bishop spherical ımages of a spacelike curve in Minkowski 3-Space. Int. J. Phys. Sci. 5:898-905.

Turgut M, Yilmaz S (2008). On The Frenet Frame and A Characterization of Space-Like Involute-Evolute Curve Couple in Minkowski Space-Time, Int. Math. Forum. 3(16):793-801.

academicJournals

Vol. 9(7), pp. 146-153, 16 April, 2014
DOI: 10.5897/IJPS2014.4117
Article Number:A408ABF44158
ISSN 1992 - 1950

http://www.academicjournals.org/IJPS

International Journal of Physical Sciences

Full Length Research Paper

Influence of pressure from compression textile bands: Their uses in the treatment of venous human leg ulcers

Bachir Chemani* and Rachid Halfaoui

Laboratory of Processing and Shaping of Fibrous Materials and Polymers, Department of Engineering Process, Faculty of Engineering Sciences, University M'Hamed BOUGARRA, Boumerdes 35000, Algeria.

Received 29 January, 2014; Accepted 21 March, 2014

The aim of study was to evaluate pressure distribution characteristics of the elastic textile bandages using two instrumental techniques: a prototype instrument and a load transference. The prototype instrument which simulates shape of real leg has pressure sensors which measure bandage pressure. Using this instrument, the results show that elastic textile bandages presents different pressure distribution characteristics and none produces a uniform distribution around lower limb. The load transference test procedure is used to determine whether a relationship exists between elastic textile bandage structure and pressure distribution characteristics. The test procedure assesses degree of load, directly transferred through a textile when loads series are applied to bandaging surface. A range of weave fabrics was produced using needle weaving machine and a sewing technique. A textile bandage was developed with optimal characteristics far superior pressure distribution than other bandages. From results, we find that theoretical pressure is not consistent exactly with practical pressure. It is important in this study to make a practical application for specialized nurses in order to verify the results and draw useful conclusions for predicting the use of this type of elastic band.

Key words: Textile, cotton, pressure, venous ulcers, elastic.

INTRODUCTION

The immobility for prolonged periods, the paralysis and other venous disorders contribute to the formation of leg ulcers. Compression bandaging is the most important single element in the conservative treatment of venous leg ulcers. The application of external compression by means of elasticity bandages serves to increase the velocity of blood flow within the veins by providing support to the calf muscles. The level of pressure exerted on the leg is a function of the tension induced into the compression bandage during application, the layers number used and the limb circumference (Van Der Molen and Kuiper, 2001).

Since the pressure produced is inversely proportional to the circumference of the limb then a pressure gradient is formed where higher pressures are exerted on the ankle than on the calf if the bandage is applied at constant tension (Moffatt, 2002, 2007). However, mis-use of compression bandages have in some instances led to further venous system complications, notably bandage induced ulcers (Zhang et al., 2002). Such ulcers may occur at the foot, fibula, and tibia regions of the leg where high compression bandage pressures are exerted over a

*Corresponding author. E-mail: chemani_ba@yahoo.fr, Tel/Fax: 213 24 81 91 53.

relatively small radius of curvature. In addition, because there is little subcutaneous tissue in this region, the likelihood of further complications is extended. The need to distribute the pressure equally on all points of the lower limb, whilst offering protection to the tibia and fibula regions is extremely important (Stacey et al., 2002). A variety of bandages are used beneath compression bandages as padding layers in order to evenly distribute pressure and give protection (Khokar, 2001). These include polyurethane foam bandages and nonwoven orthopedic waddings but there is little published material which defines their use for this particular problem or whether they have the performance criteria necessary to provide adequate pressure distribution (Onofrei et al., 2010). In order to distribute compression bandage pressure evenly around the limb it is essential that high pressures created at the tibia and fibula regions are absorbed by the padding bandage material (Radu et al., 2008). The load transference test procedure was developed so that a quick assessment of the pressure distribution characteristics of padding bandages can be made. We will also use the Laplace law to theoretically (Thomas, 2003), calculate the pressures applied, and then compare the results. This law is applied in many sectors of science, including medicine, to calculate the forces exercised on blood vessels and alveoli filled with fluid. It is necessary to use the conversion of the measuring units of measurement, that is to say, using the units pertaining to each other. According to Laplace's law, the sub-bandage pressure is directly proportional to the voltage of the latter, but inversely proportional to the radius of curvature of the body on which it is applied. In order to use Laplace's law to estimate the pressure under the bandage, it is also necessary to consider two other factors: the width *B* and number of layer applied *N*.

The calculated value of the sub-bandage pressure is the average pressure to be exerted by a bandage on one leg whose circumference is known. Calculated pressure values are significantly lower than the measured values, as shown in Figure 4, and so these results are very useful because it tells us about the behavior of the pressure applied and calculated. This leads us to say that it is therefore very important to pose elastic bands on the patient's limb in an efficient manner, hence the need to train the person responsible for this task. In second place, it has been reported that knowledge about bandages is poor and that sub-bandage pressures are largely inappropriate.

Community nurses care for the majority of patients with leg ulcers and hence it was decided to study the way in which community nurses apply bandages, and the extent to which their technique improves after training. It was also intended to test whether the bandage characteristics were a significant factor in aiding bandage application.

The main objective of this research was to produce a bandage material with far superior pressure distribution characteristics.

MATERIALS AND METHODS

The final properties of textiles depend more or less on many different technical and technological parameters, which should already be adjusted during the design phase of a textile. The fabric composed to warp yarns and weft, which mechanical properties and physical (count, strength and breaking elongation, fineness, the number of towers, the composition of raw materials, post-processing, etc.), have a significant influence (Kumar et al., 2013b, c).

To predict interfacial pressure induced by different textile structure on a curved surface of the human body, the relationship between the tensile properties of an elastic fabric, the curvature of the shaped surface, and the pressure of the skin and textile interfacial may be formulated into a mathematical expression. Pressure bandage are made from strong elastic fabric containing Lycra. Lycra several types can be used. The different degrees of elasticity and strength of materials with different degrees of tissue tension can induce different degrees of pressure on patients.

The five bandages were given identification codes (MT1, MT2, MT3, MT4 and MT5) prior to pressure distribution testing; a description of the bandages is given in Table 1. Throughout this investigation a standard high compression bandage was used in order to exert the required level of pressure 38 mmHg. A constant bandage tension of 450 cN was introduced into the compression bandage during application.

An elastic textile fabrics number were produced using weaving needle looms and sewing techniques. These fabrics were subsequently tested on load transference. It was found that the load transference performances of a fabric are reduced as a result of sewing technique. Therefore, a variety of samples were adopted until an optimum bandage will produce. The optimum bandage MT4 composed of Polyester 30%, Lycra 20%, cotton 50%, distributes pressure throughout its unique structure due to the weaving technique used. Textile fabric and padding is assembled using seam.

The theoretical method pressure calculation

Using the Laplace law to estimate the pressure under the bandage, it is also necessary to take into account two other factors: the bandage width *B* and the number of layers applied *N*. The calculated value of sub-bandage pressure is the average pressure to be exerted by a bandage on one leg whose circumference is known. To reduce the pressure variations in a given area under the bandage, padding can be used under compression bandages. Many types of tissues are composed of woven yarn, each thread composed of a plurality of fibers or yarn twisted together. Other, more advanced, the yarn cross sections may be elliptical, lenticular or racetrack.

However, in order to maintain a reasonable degree of simplicity, the banding pressure can be formulated by mathematical expression:

$$Pi - Pe = \frac{T1}{R} + \frac{T2}{R} \quad (1)$$

$$P = Pi - Pe = \frac{2T}{R} \quad (2)$$

Where: Pi - The internal pressure, Pe -The external pressure, T1 - The positive tension of textile, T2 - The negative tension of textile, R - The curvature radius, T- Tension of bandage.

Equation (2) shows that pressure inside of a spherical surface is always greater than external pressure, but the difference tends

Table 1. Sample of elastic textile bandages used in study.

Sample	Composition		Elongation (%)	Relaxed linear density, yarns/10 cm		Weave	Pending bandage material
	Warp yarns (%)	Weft yarns (%)		Weft	Warp		
MT1	Polyester 42 Lycra 8 Coton 50	Coton 100%	70	75	120	Weave plain	Polyurethane 2
MT2	Polyester 38 Lycra 12 Coton 50	Coton 100%	90	90	120	Weave plain	Polyurethane 2
MT3	Polyester 34 lycra 16 Coton 50	Coton 100%	110	110	120	Weave plain	Polyurethane 2
MT4	Polyester 30 lycra 20 Coton 50	Coton 100%	160	120	120	Weave plain	Polyurethane 2
MT5	Polyester 34 lycra 24 Coton 50	Coton 100%	190	135	120	Weave plain	Polyurethane 2

towards zero when the radius tends to infinity (when the surface becomes flat). However, pressure difference increases if the radius becomes smaller and tends to infinity as R tends to zero. When the wall is perfectly cylindrical, simply use the following Equation (3).

$$P = \frac{T}{R} \quad (3)$$

This law is applied in many sectors of science, including medicine, to calculate the forces exercised on blood vessels and alveoli filled with fluid. It is necessary to use the measuring unit's conversion of measurement, that is to say, using units pertaining to each other. The most common unit used is Pascal for measuring the pressure and Newton unit as measure of force, but in medical field often used following units. To reduce errors due to measurement units, it is important to consider a constant coefficient of conversion of measurement units *K* and Equation (3) takes following form:

$$P = \frac{T\,K}{R} \quad (4)$$

$$P = \frac{F}{2\pi RB} \quad (5)$$

In case of a single bandage layer applied to a member, the pressure is exerted on surface covered by the textile. This pressure will be determined by total force applied to fabric and the width the bandage in relation to the definition of pressure. Pressure applied is proportional to force on the textile and inversely proportional to application surface. Total tension developed by an elastic band is equal to sum of warp yarn tensions. The result is that number of layers, applied with a constant tension, is proportional to number of warp yarn in a point of application on surface of leg. Thus it is essential to consider number of layers in the calculations. The original formula to calculating pressure is expressed as Equation (5).

$$P = \frac{T\,.\,N}{L\,.\,B} \quad (6)$$

To move from one measurement unit to another and to avoid significant errors due to conversion of measurement units, it is useful to consider a constant K in final equation, the equation gives a *K* value of 4620. So we get the following expression (Thomas, 2003):

$$P(mmHg) = \frac{T(Kgf).N.4620}{L(cm).B(cm)} \quad (7)$$

Where: P - Pressure (mmHg), T - Tension (Kgf), L - The circumference (cm), B - Width (cm),
N - Number of layers applied.

The experimental study techniques pressure's measuring

Method of load transference

The load transference instrumental technique is based on the same type of strain gauge measurement system adopted for the prototype instrument. The load transference test-rig is used in conjunction with a Fabric Thickness Tester (Figure 1). Different loads of increasing magnitude 0 to 900 cN are applied on to surface of padding bandage single layer material and the degree of load transferred through padding bandage structure is measured by the instrument. To calibrate load transference instrument, a range of known loads 0 to 900 cN with 100 cN intervals were applied via the large contact area diameter 10 cm directly on to smaller contact area diameter 1 cm and the corresponding measured loads were recorded. The relationship between known and measured loads provides the calibration line by which load transference of padding bandages is assessed. When a load is applied onto the surface of a padding bandage material the load proportion which is transferred

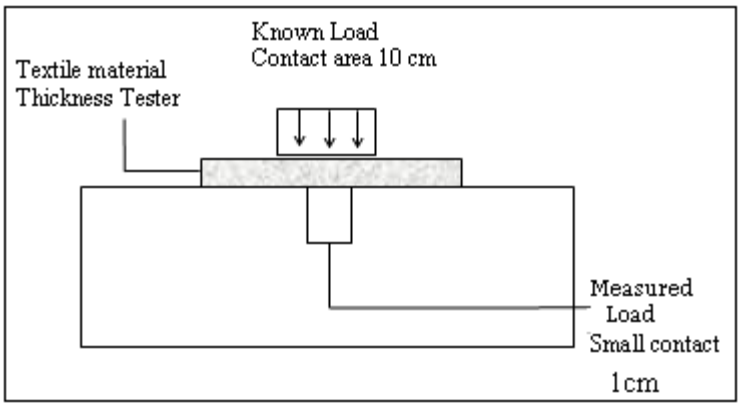

Figure 1. Load transference instrument.

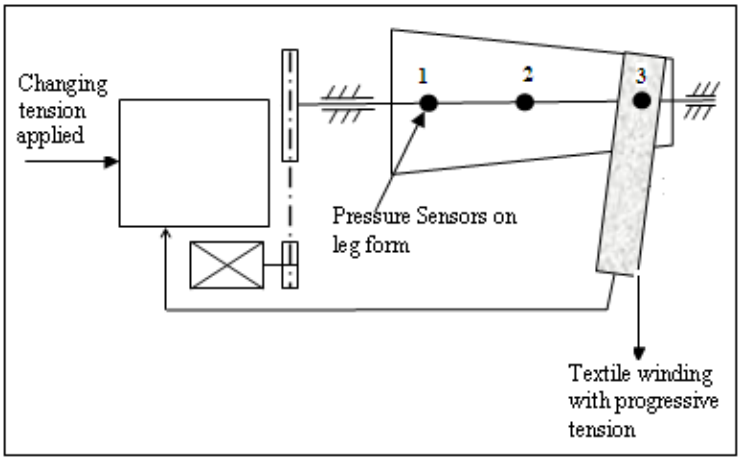

Figure 2. Prototype instrument.

through material is governed by bandage structure. Constant load transference for each increase in applied load signifies that the padding bandage material has ability to absorb high loads throughout its structure.

Using prototype instrument

The prototype instrument (Figure 2) developed in this work consists of using a mannequin leg which has eight strain gauges located inside the leg so that pressure measurements can be made at ankle, calf and positions below knee. The strain gauges are strategically positioned so that pressure measurements can be made at tibia, front and back of leg. Bandage pressure is detected by means of pressure pins which are connected to each strain gauge and protrude from inside of the leg to outer surface. To determine the pressure distribution characteristics of the bandages on the prototype instrument, one end of the bandage was attached to instrument. The prototype instrument was then rotated so that two layers of the bandage were applied. A double layer of the compression bandage, applied at a constant tension of 450 cN was placed over the padding layers and the pressure was recorded by the pressure sensors.

Each bandage was tested five times at each pressure sensor location and the recordings averaged in order to map the pressure around the instrument. Pressure measurements were taken from the application of the compression bandage to the prototype instrument without any padding layers. These pressure measurements serve to assess the pressure distribution characteristics of the padding bandages. Figure 2 illustrated a line diagram of the prototype instrument showing location of the pressure sensors numbered from smallest to largest diameter.

Practical application

Five district and practice nurses attended study days on the management of leg ulcers and were recruited as a convenience sample. The pressure produced by the nurses using each of the three selected bandages on the investigator's leg was measured using sensors and an oscillograph recording. Measurement sites were the lateral aspect of the leg, 40 mm above the center of the lateral malleolus and at the widest point of the leg, along a line joining the lateral malleolus and the tibia tuberoses. Training in compression bandaging was provided using feedback from pressure at the first study day. Nurses were also provided with

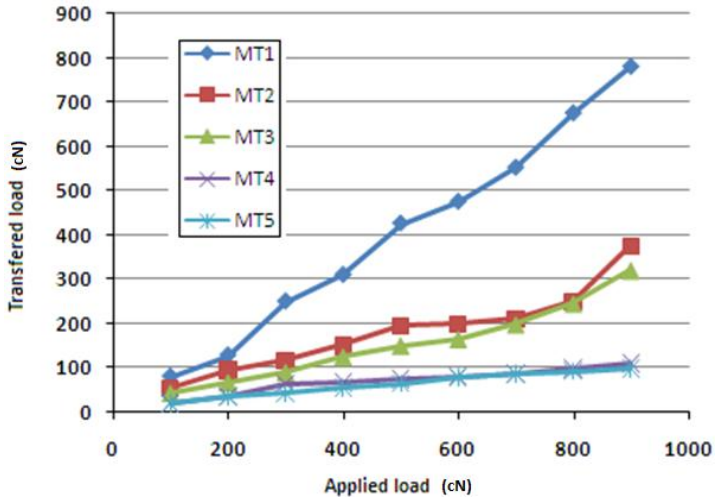

Figure 3. Transmitted load depending the applied load.

Table 2. Measured load depending the applied load.

Applied load (cN) applied	MT1	MT2	Measured load (cN) MT3	MT4	MT5
0	0	0	0	0	0
100	80	54	43	20	20
200	128	95	67	36	34
300	250	115	90	65	42
400	310	150	125	67	56
500	426	195	150	75	64
600	475	200	165	80	78
700	552	210	198	87	86
800	675	250	245	98	92
900	780	375	320	110	98

bandages to practice at home. Post-training bandaging technique was reassessed after two weeks. Immediately after their returning for a second study day, the nurses reapplies all three bandages and the result of sub-bandage pressures were recorded. The same leg, sensor sites and pressure monitor were used as at initial assessment and results are shown in Table 5.

RESULTS AND DISCUSSION

The load transference of all the bandages is shown in Figure 3. The results demonstrate that bandages exhibit different load transference properties and effectiveness of each bandage is determined by its relative position to calibration line. With textile sample MT1, the load transference line is positioned close to calibration line which indicates that the high degree of known load is directly transferred through bandage structure.

Therefore, the composite bandage is unable to dissipate loads throughout its structure and offers little support to application of known load. The MT2 and MT3 bandages sample exhibit similar load transference performances. The initial load transference, in the known load range 0 to 500 cN, is relatively low (Table 2). Throughout this range, both bandages have demonstrated their ability to support and distribute load since the degree of load transferred through the structure is minimal. At load range 500 to 900 cN, it can be seen that load transference bandage changes. The degree of load which is transferred through the bandage structure increases indicating that ability to support and distribute load rapidly, diminishes as the known load is increased. With the MT4 and MT5 bandages, the load transferred through the bandage structure remains constant throughout the load range 0 to 900 cN. Therefore, both bandages are able to absorb high loads and dissipate the load through their entire structure while load transferred through is minimal. The pressure distribution characteristics of the bandages obtained using the

Table 3. Pressure Distribution using prototype instrument.

Textile pressure using pressure sensor (mmHg)	Ankle	Leg area	Below knee
		Calf	
Theoretical	52.4	30.2	32.6
Compression MT1	60.9	24.6	49.2
Compression MT2	49.0	33.6	42.6
Compression MT3	62.3	33.2	42.8
Compression MT4	53.2	32.4	34.6
Compression MT5	48.1	25.2	37.8

Table 4. Calculation results on five different humans subjects using MT5.

Human subject (S)	1			2			3			4			5		
Z	Z1	Z2	Z3	Z1	Z2	Z3	Z1	Z2	Z3	Z1	Z2	Z3	Z1	Z2	Z3
Cm (cm)	31.7	29.3	26.5	33.5	31.1	27.6	31.4	26.1	23.2	31.0	27.1	24.1	33.0	31.8	28.2
Pm (mm Hg)	21.4	21.3	20.5	21.2	20.5	18.6	19.6	23.2	19.4	18.9	20.2	21.3	20.8	21.5	19.5

Cm - Circumference of each measuring location on the low limb (cm), Pm - pressure calculated (mm Hg), S - Human subject: Z1 (Ankle), Z2 (Calf), Z3 (Below knee).

prototype instrument is shown in Table 3. The theoretical pressures calculated from the leg circumference at ankle, calf, and below knee positions are lower than pressures exerted by the compression bandage when no padding layer was used. High compression bandage pressures are exerted on the tibia. We note importance of prototype instrument, sensors 1 and 3 which results in an uneven pressure distribution at the ankle and below knee positions. However, around circumference of the calf an even pressure distribution maintained since the tibia at this position, is less pronounced and therefore, pressure exerted by the compression bandage is low. The bandages do not produce uniform pressure distributions around circumferences of the ankle, calf, and below knee positions of the prototype instrument.

The results show that the MT5 bandage performs better and its application both is reducing the tibia pressures and provides even pressure distributions around circumferences of the ankle, calf, and knee. From Table 4, we observed the results of calculations to five real pressures on the MT5 elastic band.

If we compare these results with the experiment results on the prototype, we observe that there is some difference, amounting to approximately 60% at the ankle, 5% at the calf and 38% above the knee. The main problem with bandaging technique is production of a reverse pressure gradient and ankle pressures are being too high or too low in 20% of bandages. Thus pressure gradient and ankle pressure will be the dependent variables in the impact analysis of training on bandaging. Pressures obtained according to the bandages applied by nurses are shown in Table 5.

The pressures generated by compression bandage must be equal any points in the leg around a given circumference. The application of padding bandages should provide an even pressure distribution by reducing high pressures exerted on tibia and fibula prominences. The results obtained demonstrate that excessive pressures are not significantly reduced by the bandages investigated in this study. The relationships which exist between large and small curvatures radius of leg are directly responsible for these non-uniform pressure distributions. High pressures are generated over a relatively small radius of curvature.

The instrumental test procedures used in study confirm that bandages have different pressure distribution characteristics. The results show that MT5 bandage is the most performance and this can be attributed to its ability to absorb as well as dissipate high compression bandage pressures. This ability is largely determined by the bandage structure governed by arrangement and interaction of the constituent fibers. The MT5 bandage has a better load transference due to its complex structure which consists of a large number of fibers which are formed during weaving. The fibers are positioned perpendicular to the bandage plane within the structure and support loads which are applied onto the bandage surface.

Resistance and support to the applied load is provided by a combination of both number of fiber contained within structure and relative stiffness of each fiber. The overall fiber system of the MT5 bandage is able to provide support to any load within the range to 0-900 cN. A small proportion of applied load is directly transferred through while the remainder is dissipated throughout the bandage structure. This unique property contributes to superior pressure distribution characteristic of this bandage. The MT4 bandage has a similar load transference performance to the MT5 bandage but has inferior pressure distribution characteristic. This can be attributed

Table 5. Practical Pressures obtained.

Bandage	Ankle *Theoretical pressure* (mmHg)	Ankle *Practical pressure* (mmHg)	Below knee *Theoretical pressure* (mmHg)	Below knee *Practical pressure* (mmHg)
MT1	60.9	24.02	49.2	25.19
MT2	49.0	29.04	42.6	25.02
MT3	62.3	29.02	42.8	24.95

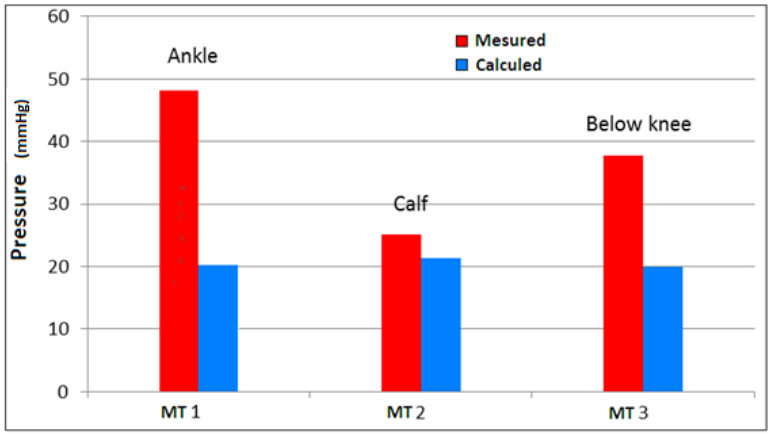

Figure 4. Pressure measured and calculated.

to its high flexural rigidity which makes it less conformable than fiber-based bandages and is more likely to crease when applied around the limb. Following the result, high compression bandage pressures are generated over areas that have become large. The MT2 and MT3 bandages are able to dissipate low loads throughout their structures.

However, this ability decreases quickly when applied load is increased 500 to 900 cN. A greater proportion load is transferred through the padding bandage. Therefore, the high compression bandage pressures which are generated over a small radius of curvature are not absorbed by the bandages. The band structure MT1 is a little less complex and consists of loose fibers found primarily on horizontal plane of bandage. The application of loads to padding bandage surface culminates in the displacement of the fibers relative to one another. The increase in the load resulting from the large number of fibers displaced which reducing the degree support and a higher proportion of applied load is transferred through while the load dissipated is minimal. The fibers contained within the MT1 bandage form a segregated structure in which individual fibers are not combined to enhance the bandage properties. Resistance and support to applied loads is not provided by this segregated structure since the fibers have no direct inter relationship relative to one another and leads to poor pressure distribution characteristic.

The load transference bandage can be used to determine its pressure distribution characteristics. The bandages having high load transference, as the MT1 bandage, are unable to absorb high compression bandage pressures and produce uniform pressure distributions. In practical the pressures of ankle were lower than calf pressures ($p<0.05$) for three bandages, the gradient is greater than 1.0 (Figure 4). The change in the pressure gradient was achieved by decreasing the calf pressure rather than increasing the ankle pressure. The ankle pressure remained marginally low throughout the study to around 25 to 30 mmHg compared to recommended value 40 mmHg.

Conclusions

None of bandages investigated in this work provides uniform pressure distributions around the limb. The structure of bandage is regarded as important factor to producing uniform pressure distribution. The load transference test procedure has shown that each bandage has completely different load transference. The results confirm that bandage structure has greatly

influences overall pressure distribution characteristics. Bandages having good load transference performance are able to absorb and dissipate loads throughout their structure.

The optimum bandage MT5 developed in this study has better performance of load transference than the fiber bandage. These results give a superior pressure distribution characteristic. A limited number of field trials have also been carried out for comparative performance of newly developed bandage MT5 and a commercially available product. Trials have confirmed that the MT5 bandage possesses superior pressure distribution characteristics when applied around lower limb. The results also indicate that this new bandage structure enables reduction of pressure experienced by the patient on certain parts of the leg and also assists to achieving more uniform pressure distributions. The nurses perform extremely poorly initially and their technique improved after training. There is no statistically significant difference between numbers of nurses applying the strips correctly.

ACKNOWLEDGEMENT

This topic is carried out within framework of national research projects funded by the Directorate General of Scientific Research and Technological Development

Conflict of Interests

The author(s) have not declared any conflict of interests.

REFERENCES

Khokar N (2001). 3D-weaving: theory and practice. J. Text. Inst. 92(2):193-207. http://dx.doi.org/10.1080/00405000108659570

Kumar B, Das A, Alagirusamy R (2013b). Effect of material and structure of compression bandage on interface pressure variation over time. Phlebology. http://dx.doi.org/10.1177/0268355513481772 PMid:23571751

Kumar B, Das A, Alagirusamy R (2013c). Study of the effect of composition and construction of material on sub-bandage pressure during dynamic loading of a limb *in vitro*. Biotheology 50:83-94. PMid:23619155

Moffatt CJ (2007). Compression therapy in practice. Aberdeen: Wounds UK Publishing.

Moffatt CJ (2002). Four-layer bandaging: From concept to practice. Int. J. Low Extrem. Wounds. 1(1):13-26. http://dx.doi.org/10.1177/153473460200100103 PMid:15871948

Onofrei E, Rocha A, Catarino MA (2010). Thermal comfort properties of knitted fabrics made of elastane and bioactive yarns. In: Proceedings of the Fiber Society Spring. Int. Conf. Fibrous Mater. Bursa, Turkey. pp. 145–146.

Radu CD, Popescu V, Manea LR, Harpa R (2008). Behavior of Medical Stockings Used In Chronic Venous Failure of Leg. Book of Abstracts: 8th AUTEX Conference.

Stacey MC, Falanga V, Marston W, Moffatt C (2002). The use of compression therapy in the treatment of venous leg ulcers. EWMA J. 2(1):9-13.

Thomas S (2003). The use of the Laplace equation in the calculation of sub-bandage pressure, EWMA. J. 3(1):21-23.

Van Der Molen H, Kuiper JH (2001). Mesure de la compression en thérapeutique phlébologie et notamment de pression permanente efficace après réduction de l'œdème. Phlébologie. 13:105-112.

Zhang X, Yeung KW, Li Y (2002). Numerical simulation of 3D dynamic garment pressure. Text. Res J. 72(3):245-252. http://dx.doi.org/10.1177/004051750207200311

academicJournals

Vol. 9(7), pp. 154-173, 16 April, 2014
DOI: 10.5897/IJPS2014.4121
Article Number:075DCA344159
ISSN 1992 - 1950

http://www.academicjournals.org/IJPS

International Journal of Physical Sciences

Full Length Research Paper

Theoretical spin assignment and study of the A~100 – 140 superdeformed mass region by using ab formula

A. S. Shalaby[1,2]

[1]Applied Physics Department, Faculty of Applied Science, Taibah University, Saudi Arabia.
[2]Physics Department, Faculty of Science, Beni Suef University, Egypt.

Received 31 January, 2013; Accepted 2 April, 2014

Using an empirical formula of rotational spectra which consists of two parameters a and b (known as ab formula) and derived from the Bohr-Hamiltonian, we extract the spins of fifteen superdeformed bands observed in the A~ 100-140 mass region. The two parameters "a" and "b" were determined by using a search program to fit the proposed transition energies with their observed values. The calculated transition energies depend sensitively on the prescribed spins. The agreement between the calculated and observed transition energies is incredibly well when a correct spin assignment is made. The quality of the fit is generally good in the proposed nuclei, namely: ^{104}Pd(b1), ^{132}Ce(b1), ^{134}Nd(b1), ^{136}Nd(b2), ^{142}Sm(b1), ^{148}Eu(b1, b2), ^{131}Ce(b1, b2), ^{133}Ce(b1, b2), ^{133}Pr(b1, b3), ^{137}Sm(b1), ^{143}Eu(b1). Also, a good agreement is achieved between the extracted spin values in this paper with other theoretical models and also with the available experimental data.

Key words: Superdeformed nuclei, Even-A and Odd-A Nuclei of the superdeformed Mass Region 100-140, ab formula.

INTRODUCTION

The topic of Superdeformation has been at the forefront of nuclear structure physics since the observation of the first superdeformed band in ^{152}Dy (Twin et al., 1986; Bently et al., 1987). Experimental data on SD rotational bands are now available in different parts of the periodic table, namely; in the A~ 190, ~ 150, ~ 130, and ~ 80 mass regions (Hu and Zeng, 1997; Sevensson, 1999; Singh et al., 1996; Afanasjev et al., 1996).

Specially, the superdeformed mass region A~ 100-140 is of particular interest (Szymanski , 1996; Laird, 2002; Leoni et al., 2001; Khazov et al., 2005; Khazov et al., 2006) because of limited number of particles in these nuclei. Moreover, the poor study of these SD nuclei theoretically. The vast majority of the SD bands in this mass region show similar behavior of their dynamic moment of inertia, $\theta^{(2)}$, with the rotational frequency, $\hbar\omega$, in that, they exhibit a smooth decrease as $\hbar\omega$ increases.

For the SD bands, gamma ray energies are unfortunately the only spectroscopic information universally available. Because of the non-observation of the discrete linking transitions between the SD states and the low lying states at normal deformation (ND), the

*E-mail: ashalaby15@yahoo.com

experimental data for the spin of the rotational bands is poor and the only way to obtain the value of the spin is doing theoretically. Several approaches for assigning spins to SD states have been proposed (Draper et al., 1990; Stephens, 1990; Becker et al., 1990; Wu et al., 1992; Hegazi et al., 1999; Khalaf et al., 2002; Shalaby, 2004). These approaches involve direct and indirect methods for assigning spin to the states in SD bands.

In the direct method like Bohr-Mottelson I (I+1) expansion (Bohr and Mottelson, 1975), ab formula (Wu et al., 1989; Holmberg and Lipas, 1968) and the abc formula (Wu et al., 1989), the energies of the states of rotational bands are expressed as a function of spin based on two or more parameters formula. Assuming various values for the spin I_0 of the lowest state in the SD bands, the two or more parameters can be adjusted to obtain a minimum root mean square deviation of the calculated and measured energies. On the other hand, the indirect methods rely mainly on the fitting of the experimental dynamical moment of inertia values with Harris formula (Stephens, 1990; Becker et al., 1990a; Hegazi et al., 1999; Shalaby, 2004; Becker et al., 1990b; Harris, 1964). The parameters obtained from the fit are then used to calculate the spin. In such a parameterization, the spin may be expressed as an expansion in the rotational frequency ħω. Such available approaches are usually referred to the best-fit method (BFM). There are two main problems within this method. On one hand, neither dynamic moment of inertia ($\theta^{(2)}$) nor rotational frequency (ħω) is quantities directly measured in experiment. One can estimate their values. On the other hand, this procedure contains an integration constant, which is in some way an additional parameter.

The method used in the present paper is a direct method based on a formula connecting directly spin and energy of a same level. To our opinion, this method has two advantages than the Harris three-parameter approach (Harris, 1964) done in our previous work (Shalaby, 2004) and others (Hegazi et al., 1999; Khalaf, 2002), where we study in our previous work (Shalaby, 2004) the SD mass region 60-90. First, it is rather general and is obtained within different approaches. Second, it is not necessary to introduce quantities, which are not directly measured in experiment. Spin assignment can be done by using only the transition energies. Unlike the rotational frequency employed in our previous work (Shalaby, 2004), the angular momentum is a directly measured quantity, hence the parameters exist in the present formula connecting the energy and spin, can be determined very easily from the observed rotational spectrum. A theory used to determine the spins of the considered superdeformed rotational bands in the A~ 100-140 mass region with the present ab approach was given. All the data on the fifteen SD bands observed in the A~ 100-140 region are analyzed by making use of this approach. The spins of all these SD bands are determined and the results seem reasonable. With the spin values thus assigned, the energy spectra of these SD bands were calculated and the results turned out unexpectedly well.

THEORY

The simple and effective method used to determine the spin values of the SD rotational bands is the ab-method (also called ab fitting) (Wu et al., 1992). In this method, the two parameter empirical expression for the rotational energy is given as:-

$$E(I) = a\left[\sqrt{1+bI(I+1)} - 1\right] \quad (1)$$

Which may be derived from the Bohr Hamiltonian for a well deformed nucleus with small axial symmetry. According to Equation (1), the transition energy from levels I to I-2 is:-

$$\begin{aligned} E_\gamma(I) &= E_\gamma(I \to I-2) \\ &= a\left[\sqrt{1+bI(I+1)} - \sqrt{1+b(I-2)(I-1)}\right] \end{aligned} \quad (2)$$

For an SD cascade:

$$I_0 + 2n \to I_0 + 2n - 2 \to ..... \to I_0 + 4 \to I_0 + 2 \to I_0, \quad (3)$$

The observed transition energies:

$$E_\gamma(I_0+2n), E_\gamma(I_0+2n-2), ...E_\gamma(I_0+4) \text{ and } E_\gamma(I_0+2)$$

Can be least-squares fit by Equation (2) (ab fit) with fitting parameters a and b. It is found that, in general, the agreement between the calculated and observed transition energies depends sensitively on the prescribed level spins. When a correct "I_0" value is assigned, the calculated transition energies were found to coincide with the observed ones relatively well. However, if I_0 is shifted away from the correct ones even merely by ±1, the root mean square (rms) deviation:

$$\sigma = \left[\frac{1}{n}\sum_{i=1}^{n}\left|\frac{E_\gamma^{cal.}(I_i) - E_\gamma^{\exp.}(I_i)}{E_\gamma^{\exp.}(I_i)}\right|^2\right]^{1/2} \quad (4)$$

n which is the number of transitions involved in the fitting will increase drastically. Therefore, the spin value of the lowest (proposed) spin and hence all the spin values of the SD band levels can be determined. This quantity "σ" used in Wu et al. (1992) was taken to fit because the experimental error bars in determination of the level energies are used not reported. As the spin value of the lowest spin I_o is known, all the spin values of the SD band levels can be determined, it is clear that this fitting procedure is quite easy and straight forward and is much simpler than that using the Harris ω^2 - expansion (Hegazi et al., 1999; Khalaf, 2002; Shalaby, 2004).

We now remind the reader that a three-parameter Harris expansion of the cranking model (Harris, 1964) gives rise to the expression of energy:

$$E(\omega) = \alpha\omega^2 + \beta\omega^4 + \gamma\omega^6 \quad (5)$$

Which leads to the dynamic moment of inertia (Shalaby, 2004)

$$\theta^{(2)}(\omega) = 2\alpha + 4\beta\omega^2 + 6\gamma\omega^4 \ (\hbar^2 \text{ MeV}^{-1}) \quad (6)$$

Table 1. involves the three fitting parameters and the bandhead spin resulting from our present calculations, other works and the available experimental data for the assumed even-A and odd-A SD bands.

SD band	$E_\gamma(I_0+2\rightarrow I_0)$ (KeV)	Parameter			Band head spin or proposed spin (I_0)		
		ax10^5 (KeV)	b x 10^{-4}	$J_0=\hbar^2/ab$ ($\hbar^2$/MeV^{-1})	Present work	Previous works [Ref.]: [1](Singh et al., 1996), [2](Singh et al., 2002), [3](Shalaby et al., 2012)	Exp.data[Ref.] (Singh et al., 1996)
^{104}Pd(b1)	1263.0	1.93	2.01	25.78	15	22^2, 21^3	-
^{132}Ce(b1)	808.0	1.61	1.42	43.74	15	17^2, 18^1, 28^3	-
^{134}Nd(b1)	663.9±0.5	0.72	3.21	43.57	13	$15^{2,3}$	14
^{136}Nd(b2)	888.0±1.0	5.57	0.325	55.24	23	30^3	23
^{142}Sm(b1)	680.0	1.14	1.75	50.13	15	23^2, 22^3	-
^{148}Eu(b1)	748.0	1.24	1.40	57.60	20	30^2, 31^3	-
^{148}Eu(b2)	844.0	1.27	1.38	57.06	23	26^2, 35^3	-
^{131}Ce(b1)	591.0	1.61	1.37	45.34	11.5	12.5^2, 16.5^3	-
^{131}Ce(b2)	847.0	1.43	1.54	45.41	17.5	21.5^2, 26.5^3	-
^{133}Ce(b1)	748.0	1.44	1.50	46.30	15.5	19.5^2, 21.5^1, 24.5^3	-
^{133}Ce(b2)	720.3	1.49	1.46	45.97	14.5	16.5^2, 18.5^1, 21.5^3	-
^{133}Pr(b1)	871.0	1.81	1.16	47.62	19.5	$25.5^{1,2}$, 22.5^3	-
^{133}Pr(b3)	821.0	1.51	1.51	43.86	16.5	25.5^2, 24.5^3	-
^{137}Sm(b1)	379.0	1.99	0.98	51.43	9.5	8.5^1, 6.52, 8.5^3	-
^{143}Eu(b1)	483.0	2.31	0.73	59.14	12.5	$14.5^{2,3}$	15.5

This equation can be rewritten as: -

$$\theta^{(2)} = A + B\omega^2 + C\omega^4 \quad (\hbar^2\ \text{MeV}^{-1}) \tag{7}$$

The spin can be predicted by integrating $\theta^{(2)}$ (Equation 7) with respect to ω

$$\hbar\hat{I} = A\omega + \left(B/3\right)\omega^3 + \left(C/5\right)\omega^5 + i_0 \quad (\hbar) \tag{8}$$

where the constant of integration (i_0) is called the aligned spin (resulting from the alignment of a pair of high-j particles) and it is always equal to zero.

RESULTS AND DISCUSSION

All the transition energies in the fifteen SD bands observed in the A~ 100-140 mass region have been least-squares fit by Equation (2) and the results are encouraging. We have obtained the values of the expansion coefficients a, b by using the Levenberg-Marquardt method (Flannery et al., 1992), to fit the proposed transition energies with their observed values. These fitting were done for the SD bands ^{104}Pd(b1), ^{132}Ce(b1), ^{134}Nd(b1), ^{136}Nd(b2), ^{142}Sm(b1), ^{148}Eu(b1, b2), ^{131}Ce(b1, b2), ^{133}Ce(b1, b2), ^{133}Pr(b1, b3), ^{137}Sm(b1), ^{143}Eu(b1) in the A~ 100-140 mass region, where b1, b2 and b3 refer to band 1, 2 and 3, respectively.

The spin assignments for each SD bands and also the corresponding fitting parameters are given in Table 1. For most of the fifteen SD bands, the spin assignments relatively coincide with the results of another theoretical results (Singh et al., 2002), our previous work (Shalaby et al., 2012), and also with the available experimental data (Singh et al., 1996).

We have two types of superdeformed nuclei

Even-A nuclei (7 nuclei)

As a first illustrative example, the results of the least-squares fitting of ^{104}Pd(b1) are listed in Table 2. It is seen that the E_2-transition energies can be reproduced relatively well when I_0 = 15, that is, E(17>15) = 1263.0 MeV. The deviations between the calculated and observed E(I) values are mostly less than 30 MeV. However, if I_0 is assumed to be 14 or 16, the rms deviation immediately increases (Figures 1 to 7). Therefore, the assignments of I_0 = 14 or 16 are completely unacceptable.

Similarly, we have obtained the results of the least-squares fitting of the other 6 even – A nuclei and these are listed in Tables 3 to 8.

Odd-A nuclei (8 nuclei)

As a first illustrative example, the results of the least-squares fitting of ^{131}Ce(b1) are listed in Table 9. It is seen

Table 2. Spin determination for the SD band ^{104}Pd(b1). I_0 is the spin value prescribed to the lowest level observed. $E_\gamma(I) = E_\gamma(I \rightarrow I-2)$ is the transition energy from level I to I-2. $\delta = E_\gamma^{exp.}(I) - E_\gamma^{cal.}(I)$. σ is the rms deviation defined by Equation 4.

Observed[a] E_γ(I) values (KeV)	Calculated E_γ(I) values (KeV)								
	I_0=14[b]			I_0=15[c]			I_0=16[d]		
	I	E_γ(I)	δ	I	E_γ(I)	δ	I	E_γ(I)	δ
2079.0	28	2034.6	44.4	29	2050.1	28.9	30	1897.2	181.8
1919.0	26	1914.3	4.7	27	1924.6	-5.6	28	1794.5	124.5
1763.0	24	1788.7	-25.7	25	1795.5	-32.5	26	1687.3	75.7
1638.0	22	1657.9	-19.9	23	1663.0	-25.0	24	1575.6	62.4
1511.0	20	1522.2	-11.2	21	1527.2	-16.2	22	1459.6	51.4
1381.0	18	1381.5	-0.51	19	1388.3	-7.3	20	1339.3	41.7
1263.0	16	1236.2	26.8	17	1246.4	16.6	18	1214.9	48.1
σ		1.38×10^{-2}			1.19×10^{-2}			5.16×10^{-2}	

[a]Reference (Singh et al., 2002): [b]a = 1.22×10^{5} KeV, b = 3.40×10^{-4}; [c]a = 1.93×10^{5} KeV, b = 2.01×10^{-4}; [d]a = 1.13×10^{5} KeV, b = 3.22×10^{-4}.

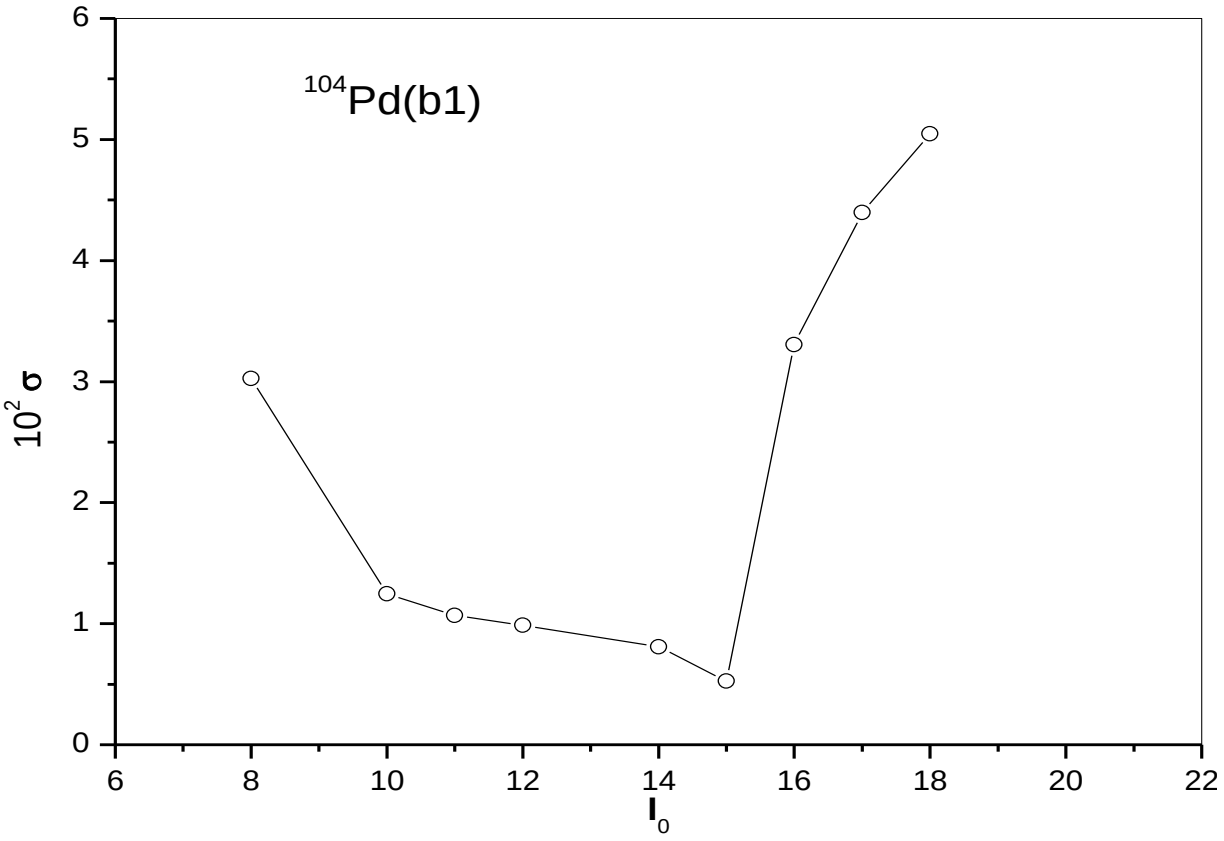

Figure 1. The rms deviation for various spin assignments in ^{104}Pd(b1). I_0 is the value prescribed to the lowest level observed [E $\gamma(I_0 + 2 \Longrightarrow I_0)$ = 1263 KeV].

that the E_2-transition energies can be reproduced relatively well when I_0 = 11.5, that is, E(13.5→11.5) = 591.0 MeV. The deviations between the calculated and observed E(I) values are mostly less than 81 MeV. However, if I_0 is assumed to be 10.5 or 12.5, the rms deviation immediately increases (Figures 8 to 15). Therefore, the assignments of I_0 = 10.5 or 12.5 are completely unacceptable.

Similarly, we have obtained the results of the least-squares fitting of the other 7 odd – nuclei and these are

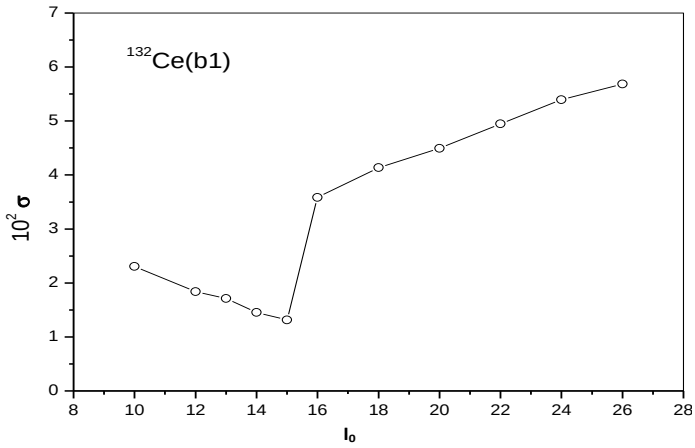

Figure 2. The rms deviation for various spin assignments in ^{132}Ce(b1). I_0 is the value prescribed to the lowest level observed [E $\gamma(I_0 + 2 ==> I_0)$ = 808 KeV].

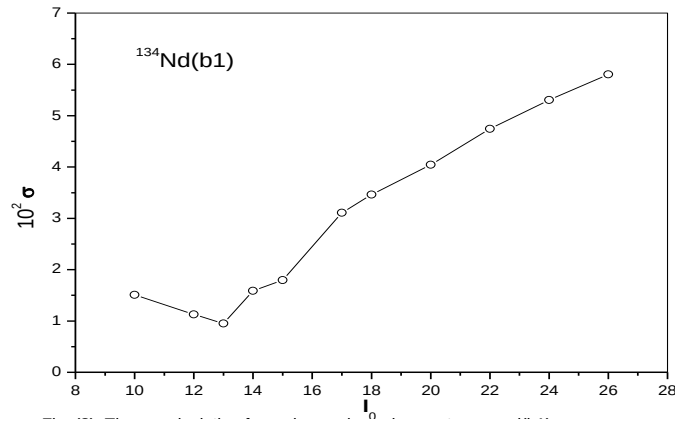

Figure 3. The rms deviation for various spin assignments in ^{134}Nd(b1). I_0 is the value prescribed to the lowest level observed [E $\gamma(I_0 + 2 ==> I_0)$ = 663.9 KeV].

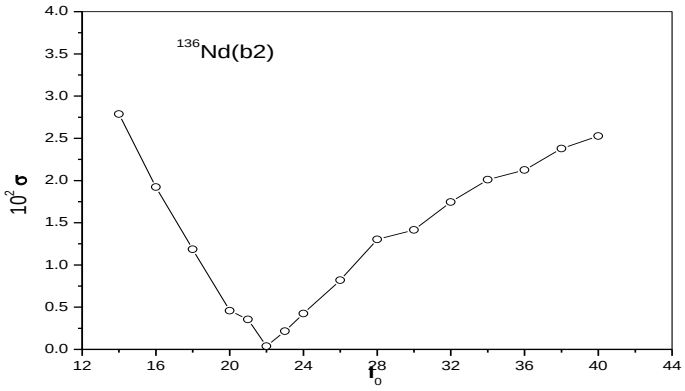

Figure 4. The rms deviation for various spin assignments in ^{136}Nd(b2). I_0 is the value prescribed to the lowest level observed [E $\gamma(I_0 + 2 ==> I_0)$ = 888 KeV].

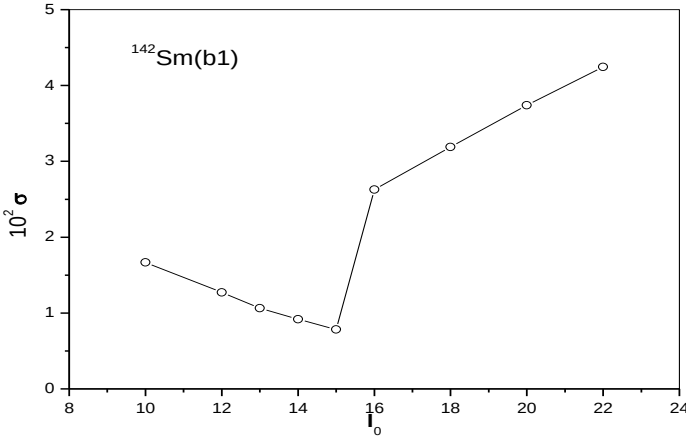

Figure 5. The rms deviation for various spin assignments in ^{142}Sm(b1). I_0 is the value prescribed to the lowest level observed [E $\gamma(I_0 + 2 ==> I_0)$ = 680 KeV].

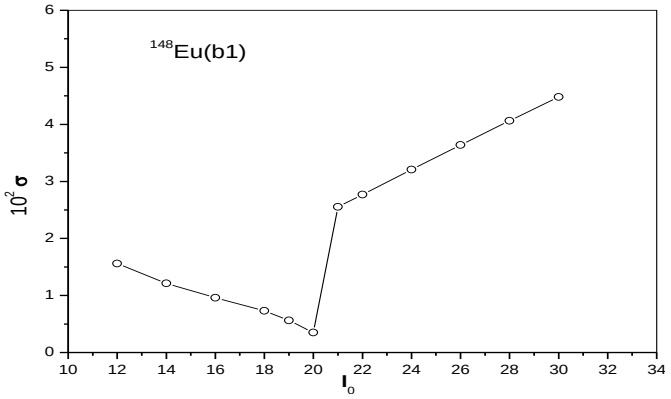

Figure 6. The rms deviation for various spin assignments in ^{148}Eu(b1). I_0 is the value prescribed to the lowest level observed [E $\gamma(I_0 + 2 ==> I_0)$ = 748 KeV].

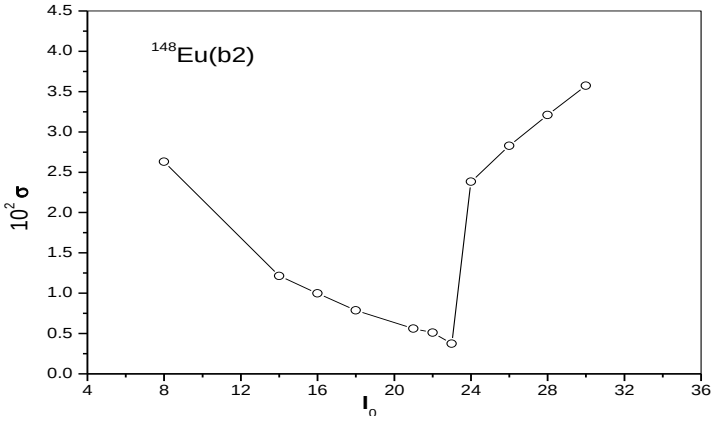

Figure 7. The rms deviation for various spin assignments in ^{148}Eu(b2). I_0 is the value prescribed to the lowest level observed [E $\gamma(I_0 + 2 ==> I_0)$ = 884 KeV].

Table 3. Spin determination for the SD band ^{132}Ce(b1). I_0 is the spin value prescribed to the lowest level observed. $E_\gamma(I) = E_\gamma(I \rightarrow I-2)$ is the transition energy from level I to I-2. $\delta = E_\gamma^{exp.}(I) - E_\gamma^{cal.}(I)$. σ is the rms deviation defined by Equation 4.

Observed[a] E_γ(I) values (KeV)	Calculated E_γ(I) values (KeV)								
	I_0=14[b]			I_0=15[c]			I_0=16[d]		
	I	E_γ(I)	δ	I	E_γ(I)	δ	I	E_γ(I)	δ
2030.0	48	1908.3	121.7	49	1920.0	110.0	50	1730.1	299.9
1930.0	46	1851.9	78.1	47	1859.7	70.3	48	1690.2	239.8
1836.0	44	1793.2	42.8	45	1797.6	38.4	46	1648.1	187.9
1739.0	42	1732.2	6.8	43	1733.6	5.4	44	1603.7	135.3
1650.0	40	1669.0	-19.0	41	1667.7	-17.7	42	1556.8	93.2
1565.0	38	1603.4	-38.4	39	1599.9	-35.0	40	1507.5	57.5
1484.0	36	1535.5	-51.5	37	1530.4	-46.4	38	1455.6	28.4
1406.0	34	1465.2	-59.2	35	1458.9	-52.9	36	1401.0	5.0
1333.0	32	1392.6	-59.6	33	1385.7	-52.7	34	1343.7	-10.7
1262.0	30	1317.7	-55.7	31	1310.6	-48.6	32	1283.5	-21.5
1193.0	28	1240.4	-47.4	29	1233.9	-40.9	30	1220.5	-27.5
1126.0	26	1160.9	-34.9	27	1155.4	-29.4	28	1154.6	-28.6
1059.0	24	1079.3	-20.3	25	1075.3	-16.3	26	1085.8	-26.8
993.0	22	995.5	-2.5	23	993.7	-0.65	24	1014.1	-21.1
928.0	20	909.8	18.2	21	910.5	17.5	22	939.5	-11.5
864.0	18	822.1	41.9	19	826.0	38.0	20	862.2	1.8
808.0	16	732.8	75.3	17	740.2	67.8	18	782.2	25.8
σ		4.04×10^{-2}			3.61×10^{-2}			6.06×10^{-2}	

[a]Reference (Singh et al., 2002): [b]a = 1.21×10^{5} KeV, b = 2.00×10^{-4}; [c]a = 1.61×10^{5} KeV, b = 1.42×10^{-4}; [d]a = 7.19×10^{4} KeV, b = 3.26×10^{-4}.

Table 4. Spin determination for the SD band ^{134}Nd(b1). I_0 is the spin value prescribed to the lowest level observed. $E_\gamma(I) = E_\gamma(I \rightarrow I-2)$ is the transition energy from level I to I-2. $\delta = E_\gamma^{exp.}(I) - E_\gamma^{cal.}(I)$. σ is the rms deviation defined by Equation 4.

Observed[a] E_γ(I) values (KeV)	Calculated E_γ(I) values (KeV)								
	I_0=12[b]			I_0=13[c]			I_0=14[d]		
	I	E_γ(I)	δ	I	E_γ(I)	δ	I	E_γ(I)	δ
1450.0	36	1393.3	56.7	37	1402.2	47.8	38	1370.2	79.8
1367.3	34	1341.8	25.5	35	1347.0	20.3	36	1318.4	48.9
1289.9	32	1287.1	2.8	33	1289.1	0.76	34	1264.0	25.9
1216.0	30	1229.0	-13.0	31	1228.5	-12.5	32	1207.0	9.0
1143.8	28	1167.5	-23.7	29	1165.1	-21.3	30	1147.4	-3.6
1074.8	26	1102.5	-27.7	27	1098.8	-24.0	28	1085.1	-10.3
1007.4	24	1033.9	-26.5	25	1029.7	-22.3	26	1020.1	-12.7
942.2	22	961.7	-19.5	23	957.8	-15.6	24	952.4	-10.2
876.5	20	886.0	-9.4	21	883.2	-6.7	22	882.1	-5.6
807.8	18	806.7	1.1	19	806.0	1.8	20	809.3	-1.5
736.7	16	724.1	12.6	17	726.3	10.4	18	734.0	2.7
663.9	14	638.2	25.7	15	644.1	19.8	16	656.4	7.5
σ		2.26×10^{-2}			1.86×10^{-3}			2.11×10^{-2}	

[a]Reference (Singh et al., 2002): [b]a = 5.43×10^{4} KeV, b = 4.53×10^{-4}; [c]a = 7.15×10^{4} KeV, b = 3.21×10^{-4}; [d]a = 6.93×10^{4} KeV, b = 3.17×10^{-4}

listed in Tables 10 to 16. The results for the transition energies in fifteen superdeformed bands observed in A~ 100-140 mass region are given in Tables 17 to 24, where the experimental data for the transition energies (labeled Exp[a]) are taken from Ref. (Singh et al., 2002) and the calculated transition energies (labeled Cal[b]) are done at

Table 6. Spin determination for the SD band ^{142}Sm(b1). I_0 is the spin value prescribed to the lowest level observed. $E_\gamma(I) = E_\gamma(I \rightarrow I-2)$ is the transition energy from level I to I-2. $\delta = E_\gamma^{exp.}(I) - E_\gamma^{cal.}(I)$. σ is the rms deviation defined by Equation 4.

Observed[a] $E_\gamma(I)$ values (KeV)	Calculated $E_\gamma(I)$ values (KeV)								
	$I_0=14$[b]			$I_0=15$[c]			$I_0=16$[d]		
	I	$E_\gamma(I)$	δ	I	$E_\gamma(I)$	δ	I	$E_\gamma(I)$	δ
1733.0	50	1665.5	67.5	51	1675.4	57.6	52	1539.8	193.2
1668.0	48	1621.7	46.3	49	1628.7	39.3	50	1506.1	161.9
1603.0	46	1576.0	27.0	47	1580.3	22.8	48	1470.6	132.4
1538.0	44	1528.2	9.8	45	1530.1	7.9	46	1433.2	104.8
1475.0	42	1478.4	-3.4	43	1478.1	-3.1	44	1393.8	81.2
1411.0	40	1426.5	-15.5	41	1424.3	-13.3	42	1352.4	58.6
1348.0	38	1372.5	-24.5	39	1368.8	-20.8	40	1308.8	39.2
1286.0	36	1316.2	-30.2	37	1311.4	-25.4	38	1263.0	23.0
1224.0	34	1257.8	-33.8	35	1252.2	-28.2	36	1215.0	9.0
1163.0	32	1197.2	-34.2	33	1191.3	-28.3	34	1164.6	-1.6
1102.0	30	1134.3	-32.3	31	1128.5	-26.5	32	1111.8	-9.8
1041.0	28	1069.3	-28.3	29	1064.0	-23.0	30	1056.6	-15.6
981.0	26	1002.1	-21.1	27	997.8	-16.8	28	998.9	-18.0
920.0	24	932.8	-12.8	25	929.9	-9.9	26	938.9	-18.9
860.0	22	861.5	-1.5	23	860.4	-0.40	24	876.4	-16.4
800.0	20	788.1	11.9	21	789.4	10.6	22	811.5	-11.5
739.0	18	713.0	26.0	19	716.9	22.1	20	744.3	-5.3
680.0	16	636.1	43.9	17	643.2	36.8	18	675.0	5.0
σ		2.70×10^{-2}			2.26×10^{-2}			4.77×10^{-2}	

[a]Reference (Singh et al., 2002): [b]a = 9.05×10^{4} KeV, b = 2.33×10^{-4}; [c]a = 1.14×10^{5} KeV, b = 1.75×10^{-4}; [d]a = 6.51×10^{4} KeV, b = 3.10×10^{-4}.

Table 7. Spin determination for the SD band ^{148}Eu(b1). I_0 is the spin value prescribed to the lowest level observed. $E_\gamma(I) = E_\gamma(I \rightarrow I-2)$ is the transition energy from level I to I-2. $\delta = E_\gamma^{exp.}(I) - E_\gamma^{cal.}(I)$. σ is the rms deviation defined by Equation 4.

Observed[a] $E_\gamma(I)$ values (KeV)	Calculated $E_\gamma(I)$ values (KeV)								
	$I_0=19$[b]			$I_0=20$[c]			$I_0=21$[d]		
	I	$E_\gamma(I)$	δ	I	$E_\gamma(I)$	δ	I	$E_\gamma(I)$	δ
1555.0	51	1520.09	34.91	52	1526.89	28.11	53	1396.12	158.88
1499.0	49	1478.05	20.95	50	1482.96	16.04	51	1366.33	132.67
1443.0	47	1434.44	8.56	48	1437.65	5.35	49	1334.95	108.05
1388.0	45	1389.21	-1.21	46	1390.95	-2.95	47	1301.93	86.08
1331.0	43	1342.36	-11.36	44	1342.84	-11.84	45	1267.17	63.83
1276.0	41	1293.86	-17.86	42	1293.33	-17.33	43	1230.62	45.38
1220.0	39	1243.69	-23.69	40	1242.40	-22.40	41	1192.20	27.80
1165.0	37	1191.85	-26.85	38	1190.06	-25.06	39	1151.84	13.16
1111.0	35	1138.34	-27.34	36	1136.34	-25.34	37	1109.50	1.50
1057.0	33	1083.16	-26.16	34	1081.23	-24.23	35	1065.12	-8.12
1004.0	31	1026.33	-22.33	32	1024.77	-20.77	33	1018.64	-14.64
951.0	29	967.87	-16.87	30	966.99	-15.99	31	970.05	-19.05
900.0	27	907.82	-7.82	28	907.91	-7.91	29	919.31	-19.31
848.0	25	846.23	1.77	26	847.58	0.42	27	866.43	-18.43
798.0	23	783.15	14.85	24	786.06	11.94	25	811.41	-13.41
748.0	21	718.65	29.347	22	723.41	24.59	23	754.29	-6.29
σ		1.92×10^{-2}			1.71×10^{-2}			4.60×10^{-2}	

[a]Reference (Singh et al., 2002): [b]a = 1.01×10^{5} KeV, b = 1.80×10^{-4}; [c]a = 1.24×10^{5} KeV, b = 1.40×10^{-4}; [d]a = 5.96×10^{4}, KeV, b = 3.02×10^{-4}.

Table 8. Spin determination for the SD band ^{148}Eu(b2). I_0 is the spin value prescribed to the lowest level observed. $E_\gamma(I) = E_\gamma(I \rightarrow I\text{-}2)$ is the transition energy from level I to I-2. $\Delta = E_\gamma^{exp.}(I) - E_\gamma^{cal.}(I)$. σ is the rms deviation defined by Equation 4.

Observed[a] $E_\gamma(I)$ values (KeV)	Calculated $E_\gamma(I)$ values (KeV)								
	I_0=22[b]			I_0=23[c]			I_0=24[d]		
	I	$E_\gamma(I)$	δ	I	$E_\gamma(I)$	δ	I	$E_\gamma(I)$	δ
1544.0	50	1514.4	29.6	51	1522.4	21.6	52	1406.3	137.7
1489.0	48	1470.8	18.3	49	1477.1	11.9	50	1376.1	112.9
1434.0	46	1425.5	8.5	47	1430.4	3.6	48	1344.2	89.8
1378.0	44	1378.6	-0.60	45	1382.3	-4.3	46	1310.6	67.4
1322.0	42	1330.1	-8.1	43	1332.8	-10.8	44	1275.1	46.9
1269.0	40	1279.9	-11.0	41	1281.9	-12.9	42	1237.8	31.2
1212.0	38	1228.2	-16.1	39	1229.6	-17.6	40	1198.4	13.6
1158.0	36	1174.7	-16.7	37	1175.8	-17.8	38	1157.0	0.96
1104.0	34	1119.6	-15.6	35	1120.7	-16.7	36	1113.5	-9.5
1051.0	32	1062.9	-11.9	33	1064.2	-13.2	34	1067.8	-16.8
998.0	30	1004.5	-6.5	31	1006.4	-8.4	32	1019.9	-21.9
946.0	28	944.6	1.4	29	947.3	-1.3	30	969.7	-23.7
895.0	26	883.1	11.9	27	886.9	8.1	28	917.3	-22.3
844.0	24	820.1	23.9	25	825.2	18.8	26	862.5	-18.5
σ		1.31×10^{-2}			1.17×10^{-2}			4.19×10^{-2}	

[a]Reference (Singh et al., 2002): [b]$a = 1.05 \times 10^5$ KeV, $b = 1.74 \times 10^{-4}$; [c]$a = 1.27 \times 10^5$ KeV, $b = 1.38 \times 10^{-4}$; [d]$a = 5.76 \times 10^4$ KeV, $b = 3.23 \times 10^{-4}$.

Table 9. Spin determination for the SD band ^{131}Ce(b1). I_0 is the spin value prescribed to the lowest level observed. $E_\gamma(I) = E_\gamma(I \rightarrow I\text{-}2)$ is the transition energy from level I to I-2. $\delta = E_\gamma^{exp.}(I) - E_\gamma^{cal.}(I)$. σ is the rms deviation defined by Equation 4.

Observed[a]	Calculated $E_\gamma(I)$ values (KeV)								
	I_0=10.5[b]			I_0=11.5[c]			I_0=12.5[d]		
$E_\gamma(I)$ values (KeV)	I	$E_\gamma(I)$	δ	I	$E_\gamma(I)$	δ	I	$E_\gamma(I)$	δ
1822.0	44.5	1727.5	94.5	45.5	1741.0	81.0	46.5	1565.5	256.5
1732.0	42.5	1670.3	61.7	43.5	1678.6	53.4	44.5	1522.7	209.3
1640.0	40.5	1610.8	29.2	41.5	1614.4	25.6	42.5	1477.7	162.3
1550.0	38.5	1549.0	0.99	39.5	1548.4	1.6	40.5	1430.4	119.6
1464.0	36.5	1484.8	-20.8	37.5	1480.6	-16.6	38.5	1380.6	83.4
1381.0	34.5	1418.1	-37.1	35.5	1411.2	-30.2	36.5	1328.3	52.7
1301.0	32.5	1349.1	-48.1	33.5	1340.0	-39.0	34.5	1273.4	27.6
1225.0	30.5	1277.6	-52.6	31.5	1267.1	-42.1	32.5	1215.9	9.1
1151.0	28.5	1203.8	-52.8	29.5	1192.6	-41.6	30.5	1155.8	-4.8
1080.0	26.5	1127.6	-47.6	27.5	1116.5	-36.5	28.5	1092.9	-12.9
1011.0	24.5	1049.2	-38.2	25.5	1038.9	-27.9	26.5	1027.4	-16.4
943.0	22.5	968.5	-25.5	23.5	959.8	-16.8	24.5	959.1	-16.1
874.0	20.5	885.7	-11.7	21.5	879.3	-5.3	22.5	888.3	-14.3
804.0	18.5	800.9	3.1	19.5	797.6	6.4	20.5	814.9	-10.9
733.0	16.5	714.3	18.7	17.5	714.6	18.4	18.5	739.1	-6.1
662.0	14.5	625.9	36.1	15.5	630.6	31.4	16.5	660.9	1.1
591.0	12.5	558.7	32.3	13.5	566.9	24.1	14.5	600.8	-9.8
σ		3.55×10^{-2}			2.87×10^{-2}			5.78×10^{-2}	

[a]Reference (Singh et al., 2002): [b]$a = 1.07 \times 10^5$ KeV, $b = 2.21 \times 10^{-4}$; [c]$a = 1.61 \times 10^5$ KeV, $b = 1.37 \times 10^{-4}$; [d]$a = 7.02 \times 10^4$ KeV, $b = 3.15 \times 10^{-4}$

the two fitting parameters (a and b) given in Table 1. These tables give successively the calculations for even-mass nuclei and even spin (Tables 17 to 20), odd-mass nuclei with odd spin (Tables 21 to 24). The fact that the

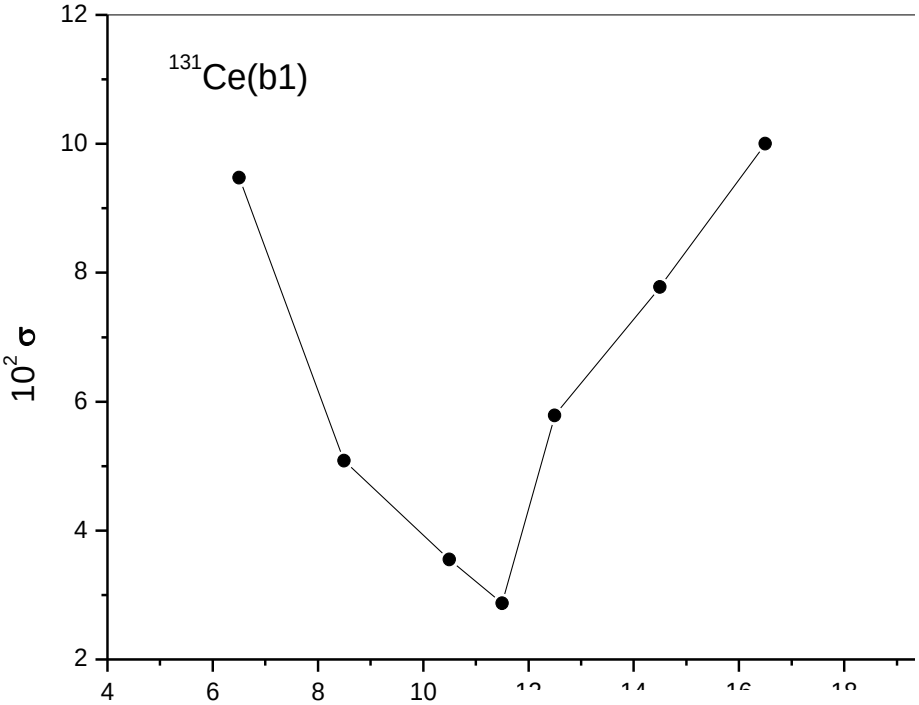

Figure 8. The rms deviation for various spin assignments in ^{131}Ce(b1). I_0 is the value prescribed to the lowest level observed [E $\gamma(I_0 + 2 \Longrightarrow I_0)$ = 591 KeV].

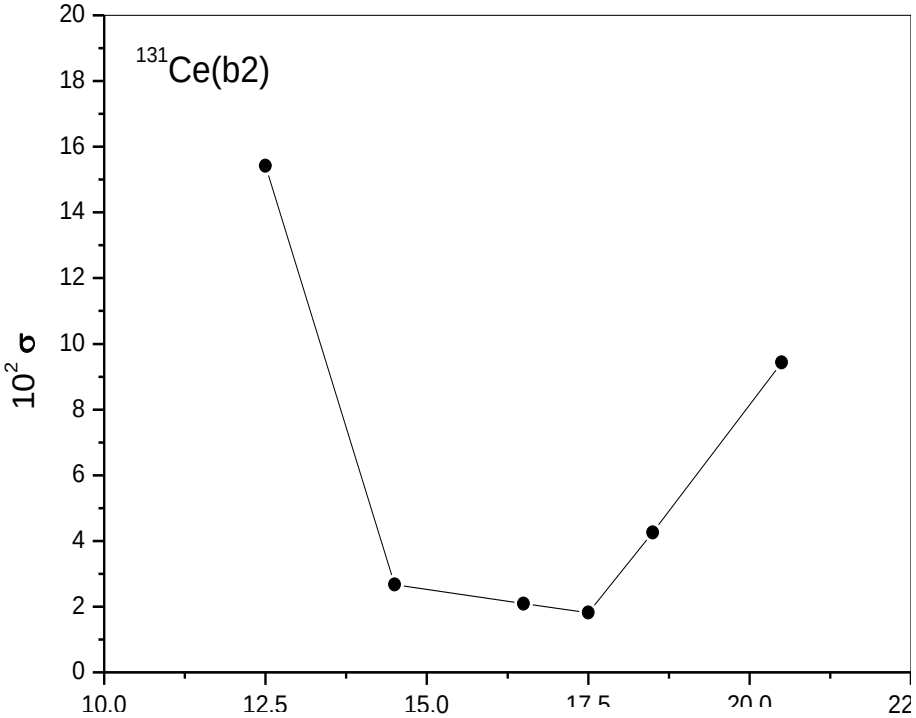

Figure 9. The rms deviation for various spin assignments in ^{131}Ce(b2). I_0 is the value prescribed to the lowest level observed [E $\gamma(I_0 + 2 \Longrightarrow I_0)$ = 847 KeV].

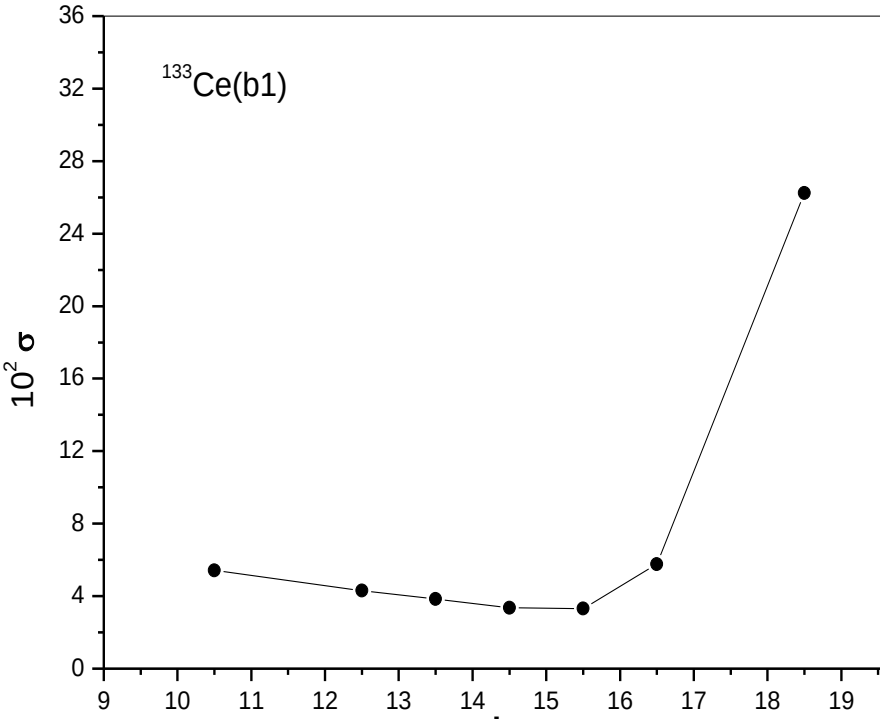

Figure 10. The rms deviation for various spin assignments in ^{133}Ce(b1). I_0 is the value prescribed to the lowest level observed [E $\gamma(I_0 + 2 \quad I_0)$ = 748 KeV].

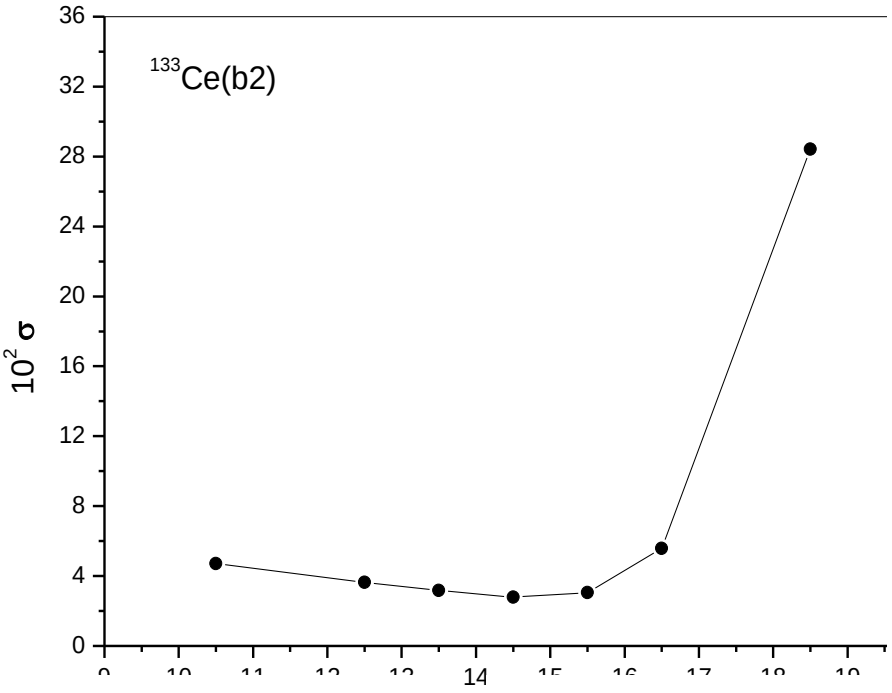

Figure 11. The rms deviation for various spin assignments in ^{133}Ce(b2). I_0 is the value prescribed to the lowest level observed [E $\gamma(I_0 + 2 \quad I_0)$ = 720.3 KeV].

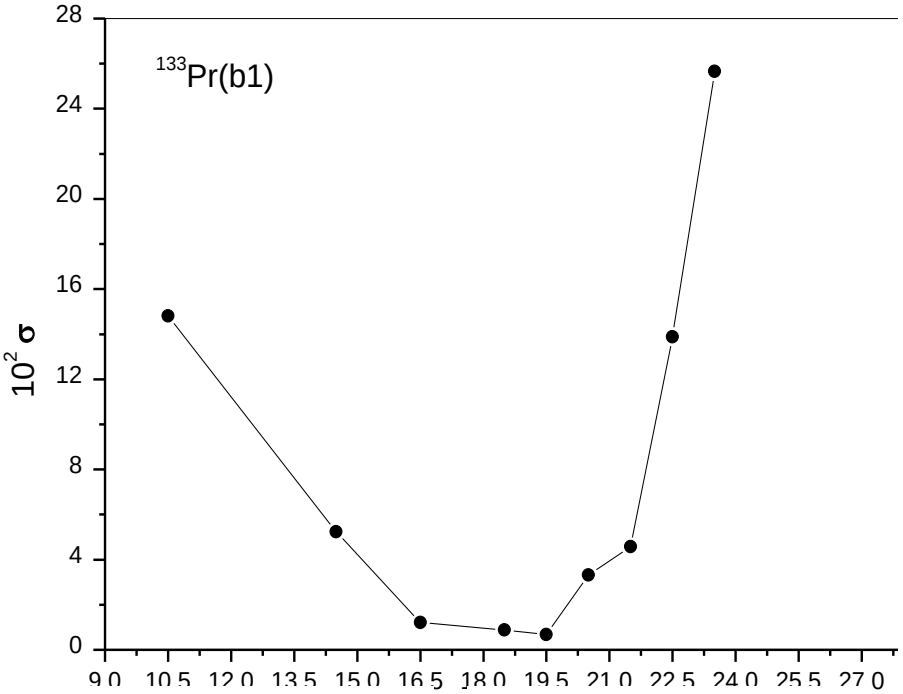

Figure 12. The rms deviation for various spin assignments in ^{133}Pr(b1). I_0 is the value prescribed to the lowest level observed [E $\gamma(I_0 + 2\ I_0)$ = 871.0 KeV].

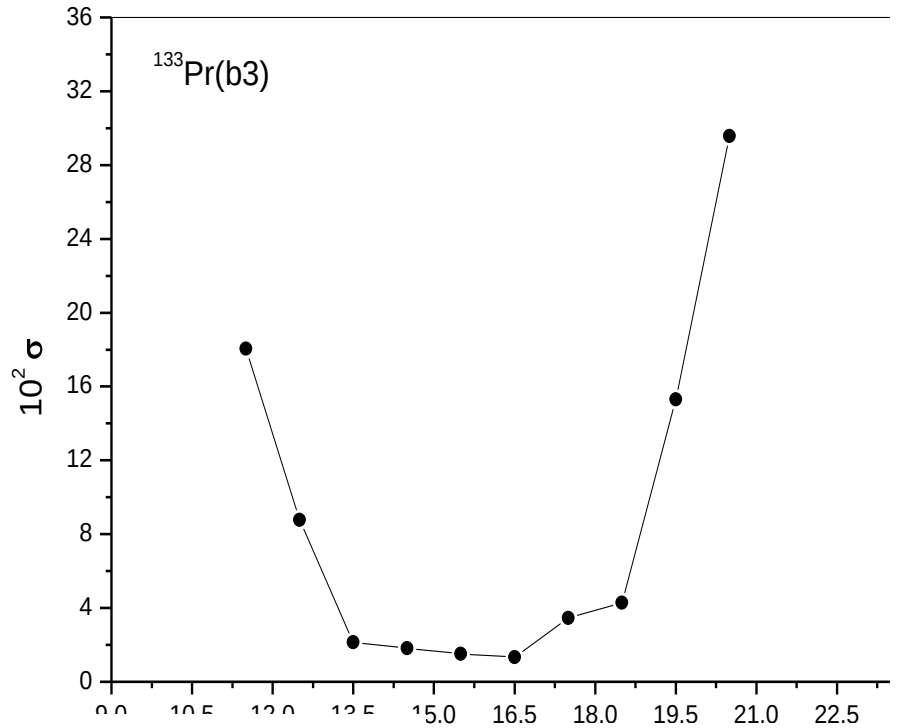

Figure 13. The rms deviation for various spin assignments in ^{133}Pr(b3). I_0 is the value prescribed to the lowest level observed [E $\gamma(I_0 + 2\ I_0)$ = 821.0 KeV].

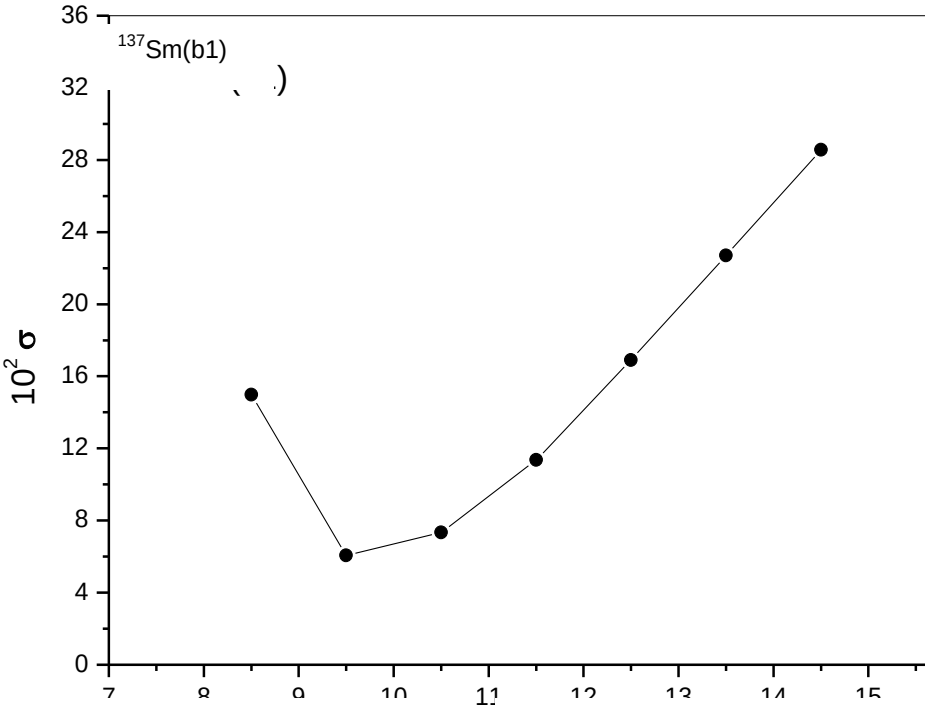

Figure 14. The rms deviation for various spin assignments in ^{137}Sm(b1). I_0 is the value prescribed to the lowest level observed [E $\gamma(I_0 + 2\ I_0)$ = 379.0 KeV].

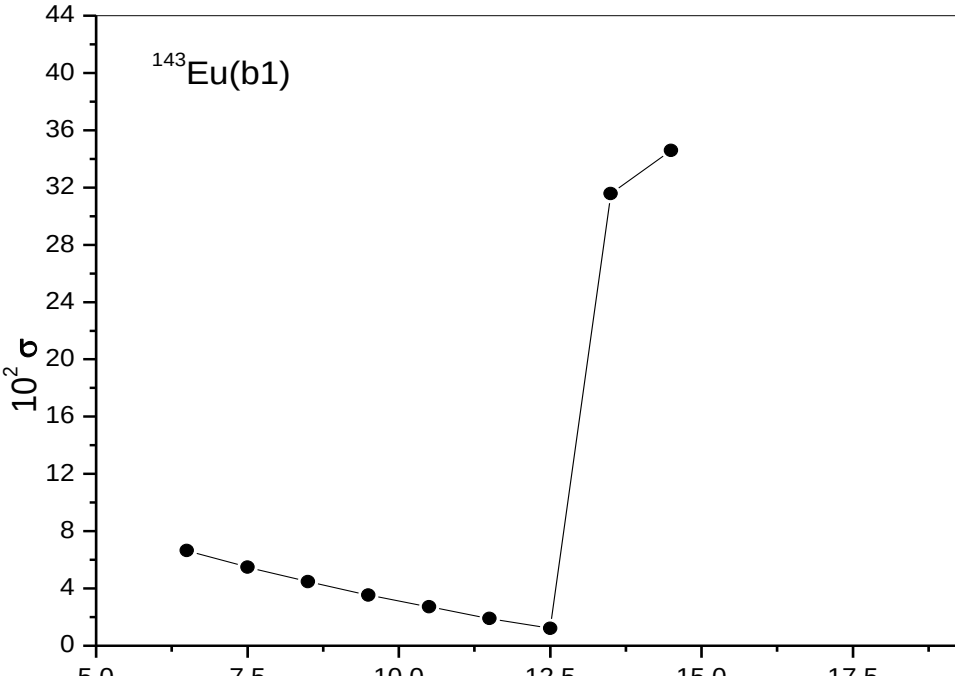

Figure 15. The rms deviation for various spin assignments in ^{143}Eu(b1). I_0 is the value prescribed to the lowest level observed [E $\gamma(I_0 + 2\ I_0)$ = 483.0 KeV].

Table 10. Spin determination for the SD band ^{131}Ce(b2). I_0 is the spin value prescribed to the lowest level observed. $E_\gamma(I) = E_\gamma(I \rightarrow I\text{-}2)$ is the transition energy from level I to I-2. $\delta = E_\gamma^{exp.}(I) - E_\gamma^{cal.}(I)$. σ is the rms deviation defined by Equation 4.

Observed[a] $E_\gamma(I)$ values (KeV)	Calculated $E_\gamma(I)$ values (KeV)								
	I_0=16.5[b]			I_0=17.5[c]			I_0=18.5[d]		
	I	$E_\gamma(I)$	δ	I	$E_\gamma(I)$	δ	I	$E_\gamma(I)$	δ
1723.0	42.5	1660.7	62.3	43.5	1672.1	50.9	44.5	1678.5	44.5
1635.0	40.5	1602.3	32.7	41.5	1611.9	23.1	42.5	1615.6	19.4
1552.0	38.5	1541.5	10.5	39.5	1549.6	2.4	40.5	1550.9	1.1
1471.0	36.5	1478.4	-7.4	37.5	1485.3	-14.3	38.5	1484.7	-13.7
1396.0	34.5	1413.0	-17.0	35.5	1418.8	-22.8	36.5	1416.7	-20.7
1322.0	32.5	1345.3	-23.3	33.5	1350.2	-28.2	34.5	1347.2	-25.2
1251.0	30.5	1275.2	-24.2	31.5	1279.5	-28.5	32.5	1276.1	-25.1
1181.0	28.5	1202.8	-21.8	29.5	1206.8	-25.8	30.5	1203.4	-22.4
1112.0	26.5	1128.2	-16.2	27.5	1132.1	-20.1	28.5	1129.3	-17.3
1043.0	24.5	1051.3	-9.3	25.5	1055.4	-12.4	26.5	1053.7	-10.7
976.0	22.5	972.3	3.7	23.5	976.8	-0.84	24.5	976.7	-0.72
908.0	20.5	891.2	16.8	21.5	896.5	11.5	22.5	898.4	9.6
847.0	18.5	808.2	38.8	19.5	814.4	32.6	20.5	818.9	28.1
σ		2.09×10^{-2}			1.82×10^{-2}			4.26×10^{-2}	

[a]Reference (Singh et al., 2002): [b]$a = 1.08\times10^{5}$ KeV, $b = 2.15\times10^{-4}$; [c]$a = 1.43\times10^{5}$ KeV, $b = 1.54\times10^{-4}$; [d]$a = 1.46\times10^{5}$ KeV, $b = 1.52\times10^{-4}$.

Table 11. Spin determination for the SD band ^{133}Ce(b1). I_0 is the spin value prescribed to the lowest level observed. $E_\gamma(I) = E_\gamma(I \rightarrow I\text{-}2)$ is the transition energy from level I to I-2. $\Delta = E_\gamma^{exp.}(I) - E_\gamma^{cal.}(I)$. σ is the rms deviation defined by Equation 4.

Observed[a] $E_\gamma(I)$ values (KeV)	Calculated $E_\gamma(I)$ values (KeV)								
	I_0=14.5[b]			I_0=15.5[c]			I_0=16.5[d]		
	I	$E_\gamma(I)$	δ	I	$E_\gamma(I)$	δ	I	$E_\gamma(I)$	δ
1928.0	48.5	1828.1	99.9	49.5	1815.0	113.0	50.5	1707.0	221.1
1833.0	46.5	1770.4	62.6	47.5	1759.6	73.4	48.5	1653.7	179.2
1743.0	44.5	1710.8	32.2	45.5	1702.5	40.5	46.5	1599.1	144.0
1655.0	42.5	1649.5	5.5	43.5	1643.6	11.4	44.5	1543.1	112.0
1570.0	40.5	1586.3	-16.3	41.5	1582.8	-12.8	42.5	1485.5	84.5
1489.0	38.5	1521.2	-32.2	39.5	1520.2	-31.2	40.5	1426.5	62.5
1411.0	36.5	1454.3	-43.3	37.5	1455.8	-44.8	38.5	1366.0	45.0
1337.0	34.5	1385.6	-48.6	35.5	1389.7	-52.7	36.5	1304.1	33.0
1267.0	32.5	1315.1	-48.1	33.5	1321.7	-54.7	34.5	1240.7	26.3
1198.0	30.5	1242.9	-44.9	31.5	1251.9	-53.9	32.5	1176.0	22.0
1132.0	28.5	1168.9	-36.9	29.5	1180.5	-48.5	30.5	1110.0	22.1
1068.0	26.5	1093.3	-25.3	27.5	1107.4	-39.4	28.5	1042.6	25.4
1003.0	24.5	1016.0	-13.0	25.5	1032.6	-29.6	26.5	974.0	29.1
937.0	22.5	937.3	-0.26	23.5	956.3	-19.3	24.5	904.1	33.0
873.0	20.5	857.0	16.0	21.5	878.6	-5.6	22.5	833.1	40.0
809.0	18.5	775.5	33.5	19.5	799.4	9.6	20.5	761.0	48.0
748.0	16.5	692.6	55.4	17.5	718.9	29.1	18.5	687.9	60.1
σ		3.36×10^{-2}			3.32×10^{-2}			5.75×10^{-2}	

[a]Reference (Singh et al., 2002), [b]$a = 1.49\times10^{5}$ KeV, $b = 1.48\times10^{-4}$; [c]$a = 1.44\times10^{5}$ KeV, $b = 1.50\times10^{-4}$; [d]$a = 1.61\times10^{5}$ KeV, $b = 1.21\times10^{-4}$.

calculated transition energies coincide with the observed results extremely well implies that the rotational spectrum in each SD band can be precisely described by Equation 1.

Conclusion

Fifteen Superdeformed bands observed in the nuclei of

Table 12. Spin determination for the SD band ^{133}Ce(b2). I_0 is the spin value prescribed to the lowest level observed. $E_\gamma(I) = E_\gamma(I \rightarrow I-2)$ is the transition energy from level I to I-2. $\delta = E_\gamma^{exp.}(I) - E_\gamma^{cal.}(I)$. σ is the rms deviation defined by Equation 4.

Observed[a] $E_\gamma(I)$ values (KeV)	Calculated $E_\gamma(I)$ values (KeV)								
	I_0=13.5[b]			I_0=14.5[c]			I_0=15.5[d]		
	I	$E_\gamma(I)$	δ	I	$E_\gamma(I)$	δ	I	$E_\gamma(I)$	δ
1731.3	45.5	1732.5	89.1	46.5	1749.3	72.3	47.5	1740.8	80.8
1731.3	43.5	1677.5	53.8	44.5	1690.3	41.0	45.5	1684.0	47.3
1643.0	41.5	1620.3	22.7	42.5	1629.5	13.5	43.5	1625.4	17.6
1557.3	39.5	1560.8	-3.5	40.5	1566.8	-9.5	41.5	1565.1	-7.8
1475.5	37.5	1499.1	-23.6	38.5	1502.4	-27.0	39.5	1503.0	-27.5
1397.9	35.5	1435.0	-37.1	36.5	1436.2	-38.3	37.5	1439.1	-41.2
1323.9	33.5	1368.7	-44.8	34.5	1368.3	-44.3	35.5	1373.4	-49.5
1253.2	31.5	1300.1	-47.0	32.5	1298.5	-45.3	33.5	1306.1	-52.9
1184.3	29.5	1229.3	-45.0	30.5	1227.1	-42.8	31.5	1237.0	-52.7
1118.2	27.5	1156.1	-38.0	28.5	1153.9	-35.7	29.5	1166.2	-48.0
1052.2	25.5	1080.8	-28.6	26.5	1079.2	-27.0	27.5	1093.8	-41.6
986.9	23.5	1003.4	-16.5	24.5	1002.8	-15.9	25.5	1019.9	-33.0
920.3	21.5	923.9	-3.6	22.5	925.0	-4.7	23.5	944.4	-24.1
854.2	19.5	842.4	11.8	20.5	845.8	8.4	21.5	867.5	-13.3
785.4	17.5	759.1	26.3	18.5	765.2	20.2	19.5	789.3	-3.9
720.3	15.5	674.1	46.2	16.5	683.4	36.9	17.5	709.7	10.6
σ		3.17×10^{-2}			2.78×10^{-2}			3.05×10^{-2}	

[a]Reference (Singh et al., 2002): [b]a = 1.09×10^{5} KeV, b = 2.11×10^{-4}; [c]a = 1.49×10^{5} KeV, b= 1.46×10^{-4}; [d]a = 1.45×10^{5} KeV, b = 1.47×10^{-4}.

Table 13. Spin determination for the SD band ^{133}Pr(b1). I_0 is the spin value prescribed to the lowest level observed. $E_\gamma(I) = E_\gamma(I \rightarrow I-2)$ is the transition energy from level I to I-2. $\Delta = E_\gamma^{exp.}(I) - E_\gamma^{cal.}(I)$. σ is the rms deviation defined by Equation 4.

Observed[a] $E_\gamma(I)$ values (KeV)	Calculated $E_\gamma(I)$ values (KeV)								
	I_0=18.5[b]			I_0=19.5[c]			I_0=20.5[d]		
	I	$E_\gamma(I)$	δ	I	$E_\gamma(I)$	δ	I	$E_\gamma(I)$	δ
1530.0	38.5	1513.2	16.8	39.5	1513.2	16.8	40.5	1540.9	-10.9
1450.0	36.5	1448.5	1.5	37.5	1446.5	3.5	38.5	1476.2	-26.2
1380.0	34.5	1381.8	-1.8	35.5	1378.2	1.8	36.5	1409.9	-29.9
1299.0	32.5	1313.2	-14.2	33.5	1308.6	-9.6	34.5	1342.0	-43.0
1228.0	30.5	1242.5	-14.5	31.5	1237.4	-9.4	32.5	1272.5	-44.5
1156.0	28.5	1169.9	-14.0	29.5	1164.9	-8.9	30.5	1201.5	-45.5
1085.0	26.5	1095.4	-10.4	27.5	1091.0	-6.0	28.5	1129.0	-44.0
1013.0	24.5	1019.1	-6.1	25.5	1015.9	-2.9	26.5	1055.0	-42.0
943.0	22.5	941.1	1.9	23.5	939.5	3.5	24.5	979.7	-36.7
871.0	20.5	861.4	9.6	21.5	862.0	9.0	22.5	903.1	-32.1
σ		8.85×10^{-3}			6.79×10^{-3}			3.32×10^{-2}	

[a]Reference (Singh et al., 2002): [b]a = 1.28×10^{5} KeV, b = 1.74×10^{-4}; [c]a = 1.81×10^{5} KeV, b = 1.16×10^{-4}; [d]a = 1.64×10^{5} KeV, b = 1.29×10^{-4}.

the mass region A~ 100-140 have been analyzed in terms of the expression for the γ-transition energies as a function of spin (ab formula). The use of direct expression of energy as a function of spin avoids necessary assumptions done in (Shalaby et al., 2012) about the values of quantities not directly measured in experiment like rotational frequency and dynamic moment of inertia. It is quite unexpected that so large a number of SD bands can be reproduced incredibly well by the simple two-parameter closed expression. It was found that the argument between the calculated and observed transition energies depends sensitively on the prescribed level

Table 14. Spin determination for the SD band ^{133}Pr(b2). I_0 is the spin value prescribed to the lowest level observed. $E_\gamma(I) = E_\gamma(I \rightarrow I\text{-}2)$ is the transition energy from level I to I-2. $\Delta = E_\gamma^{exp.}(I) - E_\gamma^{cal.}(I)$. σ is the rms deviation defined by Equation 4.

Observed[a] $E_\gamma(I)$ values (KeV)	Calculated $E_\gamma(I)$ values (KeV)								
	I_0=15.5[b]			I_0=16.5[c]			I_0=17.5[d]		
	I	$E_\gamma(I)$	δ	I	$E_\gamma(I)$	δ	I	$E_\gamma(I)$	δ
1656.0	39.5	1625.4	30.6	40.5	1637.0	19.0	41.5	1663.4	-7.4
1576.0	37.5	1561.8	14.2	38.5	1570.1	6.0	39.5	1597.1	-21.1
1500.0	35.5	1495.8	4.2	36.5	1501.3	-1.3	37.5	1529.0	-29.0
1420.0	33.5	1427.3	-7.3	34.5	1430.6	-10.6	35.5	1459.0	-39.0
1342.0	31.5	1356.3	-14.3	32.5	1358.0	-16.0	33.5	1387.3	-45.3
1264.0	29.5	1282.9	-18.9	30.5	1283.6	-19.6	31.5	1313.7	-49.7
1184.0	27.5	1207.1	-23.1	28.5	1207.3	-23.3	29.5	1238.4	-54.4
1110.0	25.5	1128.9	-19.0	26.5	1129.4	-19.4	27.5	1161.3	-51.3
1035.0	23.5	1048.4	-13.4	24.5	1049.7	-14.7	25.5	1082.7	-47.7
961.0	21.5	965.7	-4.7	22.5	968.4	-7.4	23.5	1002.4	-41.4
885.0	19.5	880.8	4.1	20.5	885.6	-0.64	21.5	920.7	-35.7
821.0	17.5	794.0	27.0	18.5	801.4	19.6	19.5	837.6	-16.6
σ		1.52×10^{-2}			1.33×10^{-2}			3.45×10^{-2}	

[a]Reference (Singh et al., 2002): [b]a = 1.09×10^{5} KeV, b = 2.21×10^{-4}; [c]a = 1.51×10^{5} KeV, b = 1.51×10^{-4}; [d]a = 1.57×10^{5} KeV, b = 1.44×10^{-4}.

Table 15. Spin determination for the SD band ^{137}Sm(b1). I_0 is the spin value prescribed to the lowest level observed. $E_\gamma(I) = E_\gamma(I \rightarrow I\text{-}2)$ is the transition energy from level I to I-2. $\delta = E_\gamma^{exp.}(I) - E_\gamma^{cal.}(I)$. σ is the rms deviation defined by Equation (4).

Observed[a] $E_\gamma(I)$ values (KeV)	Calculated $E_\gamma(I)$ values (KeV)								
	I_0=8.5[b]			I_0=9.5[c]			I_0=10.5[d]		
	I	$E_\gamma(I)$	δ	I	$E_\gamma(I)$	δ	I	$E_\gamma(I)$	δ
1115.0	28.5	936.2	178.8	29.5	1084.0	31.0	30.5	1012.4	102.6
1045.0	26.5	870.4	174.6	27.5	1014.4	30.6	28.5	949.1	95.9
970.0	24.5	804.4	165.6	25.5	943.7	26.3	26.5	885.0	85.0
890.0	22.5	738.2	151.8	23.5	872.1	18.0	24.5	820.1	69.9
806.3	20.5	671.7	134.6	21.5	799.5	6.8	22.5	754.5	51.8
719.7	18.5	605.1	114.6	19.5	726.1	-6.4	20.5	688.2	31.5
629.1	16.5	538.3	90.8	17.5	651.9	-22.8	18.5	621.2	7.9
538.5	14.5	471.4	67.1	15.5	576.9	-38.4	16.5	553.7	-15.2
451.0	12.5	404.2	46.8	13.5	501.4	-50.4	14.5	485.7	-34.7
379.0	10.5	337.1	42.0	11.5	425.2	-46.2	12.5	417.2	-38.2
σ		1.50×10^{-1}			6.06×10^{-2}			7.33×10^{-2}	

[a]Reference (Singh et al., 2002): [b]a = 7.06×10^{5} KeV, b = 2.39×10^{-5}; [c]a = 1.99×10^{5} KeV, b = 9.77×10^{-5}; [d]a = 2.14×10^{5} KeV, b = 8.17×10^{-5}.

Table 16. Spin determination for the SD band ^{143}Eu(b1). I_0 is the spin value prescribed to the lowest level observed. $E_\gamma(I) = E_\gamma(I \rightarrow I\text{-}2)$ is the transition energy from level I to I-2. $\delta = E_\gamma^{exp.}(I) - E_\gamma^{cal.}(I)$. σ is the rms deviation defined by Equation 4.

Observed[a] $E_\gamma(I)$ values (KeV)	Calculated $E_\gamma(I)$ values (KeV)								
	I_0=11.5[b]			I_0=12.5[c]			I_0=13.5[d]		
	I	$E_\gamma(I)$	δ	I	$E_\gamma(I)$	δ	I	$E_\gamma(I)$	δ
1743.0	55.5	1690.6	52.4	56.5	1707.9	35.1		2078.7	-335.7
1684.0	53.5	1644.5	39.5	54.5	1657.8	26.2		2030.9	-346.9
1623.5	51.5	1597.0	26.5	52.5	1606.7	16.8		1981.4	-357.8
1562.3	49.5	1548.2	14.1	50.5	1554.6	7.7		1929.9	-367.6
1502.2	47.5	1498.2	4.0	48.5	1501.6	0.06	49.5	1876.6	-374.4

Table 16. contd.

1442.7	45.5	1446.8	-4.1	46.5	1447.5	-4.8	47.5	1821.3	-378.6
1383.2	43.5	1394.0	-10.8	44.5	1392.6	-9.4	45.5	1764.0	-380.8
1324.1	41.5	1340.0	-15.9	42.5	1336.7	-12.6	43.5	1704.8	-380.7
1265.1	39.5	1284.6	-19.5	40.5	1279.8	-14.7	41.5	1643.5	-378.4
1206.5	37.5	1228.0	-21.5	38.5	1222.1	-15.6	39.5	1580.3	-373.8
1148.1	35.5	1170.1	-22.0	36.5	1163.5	-15.4	37.5	1514.9	-366.8
1089.9	33.5	1110.9	-21.0	34.5	1104.0	-14.1	35.5	1447.5	-357.6
1031.1	31.5	1050.5	-19.4	32.5	1043.8	-12.7	33.5	1378.1	-347.0
972.2	29.5	989.0	-16.8	30.5	982.7	-10.5	31.5	1306.7	-334.5
912.8	27.5	926.2	-13.4	28.5	920.9	-8.0	29.5	1233.3	-320.5
853.5	25.5	862.5	-9.0	26.5	858.3	-4.8	27.5	1158.0	-304.5
793.4	23.5	797.6	-4.2	24.5	795.0	-1.6	25.5	1080.8	-287.4
732.6	21.5	731.8	0.82	22.5	731.1	1.5	23.5	1001.8	-269.2
671.2	19.5	665.0	6.2	20.5	666.7	4.5	21.5	921.1	-249.9
609.0	17.5	597.4	11.6	18.5	601.6	7.4	19.5	838.7	-229.7
546.5	15.5	529.0	17.5	16.5	536.1	10.4	17.5	754.8	-208.3
483.0	13.5	460.0	23.0	14.5	470.1	12.9	15.5	669.5	-186.5
σ		1.91×10^{-2}			1.21×10^{-2}			3.16×10^{-1}	

[a]Reference (Singh et al., 2002): [b]$a = 1.54\times10^{5}$ KeV, $b = 1.16\times10^{-4}$; [c]$a = 2.31\times10^{5}$ KeV, $b = 7.32\times10^{-5}$; [d]$a = 1.33\times10^{5}$ KeV, $b = 1.71\times10^{-4}$.

Table 17. Calculation of the transition energies in Nd^{134}(b1) and Eu^{148}(b2).

Nd^{134}(b1)			Eu^{148}(b2)		
E_γ(I) (KeV) Exp[a]	Cal[b]	Assigned I	E_γ(I) (KeV) Exp[a]	Cal[b]	Assigned I
663.9	644.1	15	844.0	825.2	25
736.7	726.3	17	895.0	886.9	27
807.8	806.0	19	946.0	947.3	29
876.5	883.2	21	998.0	1006.4	31
942.2	957.8	23	1051.0	1064.2	33
1007.4	1029.7	25	1104.0	1120.7	35
1074.4	1098.8	27	1158.0	1175.8	37
1143.8	1165.1	29	1212.0	1229.6	39
1216.0	1228.5	31	1269.0	1281.9	41
1289.9	1289.1	33	1322.0	1332.8	43
1367.3	1347.0	35	1378.0	1382.3	45
1450.0	1402.2	37	1434.0	1430.4	47
			1489.0	1477.1	49
			1544.0	1522.4	51
	$\sigma = 1.86\times10^{-3}$			$\sigma = 1.17\times10^{-2}$	

spins. Therefore, the spins of each band levels can be determined.

For all fifteen SD bands, the spin values and also the corresponding parameters a and b are tabulated in Table 1. Of course, the spin assignments made in this paper remain to be confirmed from the future direct measurements.

It is seen from Table 1 that the values of the parameters a and b for all these bands are close to each other:

$a = (3.11 \pm 2.39) \times 10^{5}$ KeV,
$b = (1 : 3) \times 10^{-4}$

except for ^{136}Nd(b1) and ^{143}Eu(b1), where “b” is smaller than for the other SD bands. It is noted from these 15

Table 18. Calculation of the transition energies in Pd^{104}(b1) and Nd^{136}(b2).

Pd^{104}(b1)			Nd^{136}(b2)		
E_γ(I) (KeV) Exp[a]	Cal[b]	Assigned I	E_γ(I) (KeV) Exp[a]	Cal[b]	Assigned I
1263.0	1246.4	17	888.0	870.8	24
1381.0	1388.3	19	951.0	943.3	26
1511.0	1527.2	21	1017.0	1015.5	28
1638.0	1663.0	23	1081.0	1087.3	30
1763.0	1795.5	25	1151.0	1158.7	32
1919.0	1924.6	27	1221.0	1229.6	34
2079.0	2050.1	29	1290.0	1300.1	36
			1364.0	1370.1	38
			1438.0	1439.6	40
	$\sigma = 1.19 \times 10^{-2}$			$\sigma = 5.36 \times 10^{-3}$	

Table 19. Calculation of the transition energies in Ce^{132}(b1) and Sm^{142}(b1).

Ce^{132}(b1)			Sm^{142}(b1)		
E_γ(I) (KeV) Exp[a]	Cal[b]	Assigned I	E_γ(I) (KeV) Exp[a]	Cal[b]	Assigned I
808.0	740.2	17	680.0	643.2	17
864.0	826.0	19	739.0	716.9	19
928.0	910.5	21	800.0	789.4	21
993.0	993.7	23	860.0	860.4	23
1059.0	1075.3	25	920.0	929.9	25
1126.0	1155.4	27	981.0	997.8	27
1193.0	1233.9	29	1041.0	1074.0	29
1262.0	1310.3	31	1102.0	1128.5	31
1333.0	1385.7	33	1163.0	1191.3	34
1406.0	1458.9	35	1224.0	1252.2	35
1484.0	1530.4	37	1286.0	1311.4	37
1565.0	1599.9	39	1348.0	1368.8	39
1650.0	1667.6	41	1411.0	1424.3	41
1739.0	1733.6	43	1475.0	1478.1	43
1836.0	1797.6	45	1538.0	1530.1	45
1930.0	1859.7	47	1603.0	1580.3	47
2030.0	1920.0	49	1668.0	1628.7	49
			1733.0	1675.4	51
	$\sigma = 3.61 \times 10^{-2}$			$\sigma = 2.26 \times 10^{-2}$	

Table 20. Calculation of the transition energies in Eu^{148}(b1).

Eu^{148}(b1)		
E_γ(I) (KeV) Exp[a]	Cal[b]	Assigned I
748.0	723.41	22
798.0	786.06	24
848.0	947.58	26
900.0	907.91	28
951.0	966.99	30
1004.0	1024.77	32
1057.0	1081.23	34

Table 20. Contd.

1111.0	1136.34	36
1165.0	1190.06	38
1220.0	1242.40	40
1276.0	1293.33	42
1331.0	1342.84	44
1388.0	1390.95	46
1443.0	1437.65	48
1499.0	1482.96	50
1555.0	1526.89	52
	$\sigma = 1.71 \times 10^{-2}$	

Table 21. Calculation of the transition energies in Ce^{131}(b1) and Ce^{133}(b1).

Ce^{131}(b1)			Ce^{133}(b1)		
E_γ(I) (KeV) Exp[a]	Cal[b]	Assigned I	E_γ(I) (KeV) Exp[a]	Cal[b]	Assigned I
591.0	566.9	13.5	748.0	692.6	16.5
662.0	630.6	15.5	809.0	775.5	18.5
733.0	714.6	17.5	873.0	857.0	20.5
804.0	797.6	19.5	937.0	937.3	22.5
874.0	879.3	21.5	1003.0	1016.0	24.5
943.0	959.8	23.5	1068.0	1093.3	26.5
1011.0	1038.9	25.5	1132.0	1168.9	28.5
1080.0	1116.5	27.5	1198.0	1242.9	30.5
1151.0	1192.6	29.5	1267.0	1315.1	32.5
1225.0	1267.1	31.5	1337.0	1385.6	34.5
1301.0	1340.0	33.5	1411.0	1454.3	36.5
1381.0	1411.2	35.5	1489.0	1521.2	38.5
1464.0	1480.6	37.5	1570.0	1586.3	40.5
1550.0	1548.4	39.5	1655.0	1649.5	42.5
1640.0	1614.4	39.5	1743.0	1710.8	44.5
1732.0	1678.6	41.5	1833.0	1770.4	46.5
1822.0	1741.0	43.5	1928.0	1828.1	48.5
	$\sigma = 2.87 \times 10^{-2}$			$\sigma = 3.32 \times 10^{-2}$	

Table 22. Calculation of the transition energies in Pr^{133}(b1) and Sm^{137}(b1).

Pr^{133}(b1)			Sm^{137}(b1)		
E_γ(I) (KeV) Exp[a]	Cal[b]	Assigned I	E_γ(I) (KeV) Exp[a]	Cal[b]	Assigned I
871.0	903.1	22.5	379.0	425.2	11.5
943.0	979.7	24.5	451.0	501.4	13.5
1013.0	1055.0	26.5	538.5	576.9	15.5
1085.0	1129.0	28.5	629.1	651.1	17.5
1156.0	1201.5	30.5	719.7	726.1	19.5
1228.0	1272.5	32.5	806.3	799.5	21.5
1299.0	1342.0	34.5	890.0	872.1	23.5
1380.0	1409.9	36.5	970.0	943.7	25.5
1450.0	1476.2	38.5	1045.0	1014.4	27.5
1530.0	1540.9	40.5	1115.0	1084.0	29.5
$\sigma = 6.79 \times 10$-3				$\sigma = 6.06 \times 10^{-2}$	

Table 23. Calculation of the transition energies in Pr^{133}(b2) and Ce^{131}(b2).

Pr^{133}(b2)			Ce^{131}(b2)		
E_γ(I) (KeV) Exp[a]	Cal[b]	Assigned I	E_γ(I) (KeV) Exp[a]	Cal[b]	Assigned I
821.0	837.6	19.5	847.0	818.9	20.5
885.0	920.7	21.5	908.0	898.4	22.5
961.0	1002.4	23.5	976.0	976.7	24.5
1035.0	1082.7	25.5	1043.0	1053.7	26.5
1110.0	1161.3	27.5	1112.0	1129.3	28.5
1184.0	1238.4	29.5	1181.0	1203.4	30.5
1264.0	1313.7	31.5	1251.0	1276.1	32.5
1342.0	1387.3	33.5	1322.0	1347.2	34.5
1420.0	1459.0	35.5	1396.0	1416.7	36.5
1500.0	1529.0	37.5	1471.0	1484.7	38.5
1576.0	1597.1	39.5	1552.0	1550.9	40.5
1656.0	1663.4	41.5	1635.0	1615.6	42.5
			1723.5	1678.5	44.5
	$\sigma = 1.33 \times 10^{-2}$			$\sigma = 1.82 \times 10^{-2}$	

Table 24. Calculation of the transition energies in Ce^{133}(b2) and Eu^{143}(b1).

Ce^{133}(b2)			Eu^{143}(b1)		
E_γ(I) (KeV) Exp[a]	Cal[b]	Assigned I	E_γ(I) (KeV) Exp[a]	Cal[b]	Assigned I
720.3	683.4	16.5	483.0	470.1	14.5
785.4	765.2	18.5	546.5	536.1	16.5
854.2	845.8	20.5	609.0	601.6	18.5
920.3	925.0	22.5	671.2	666.7	20.5
986.9	1002.8	24.5	732.6	731.1	22.5
1052.2	1079.2	26.5	793.4	795.0	24.5
1118.2	1153.9	28.5	853.5	858.3	26.5
1184.3	1227.1	30.5	912.8	920.9	28.5
1253.2	1298.5	32.5	972.2	982.7	30.5
1323.9	1368.3	34.5	1031.1	1043.8	32.5
1397.9	1436.2	36.5	1089.9	1104.0	34.5
1475.5	1502.4	38.5	1148.1	1163.5	36.5
1557.3	1566.8	40.5	1206.5	1222.1	38.5
1643.0	1629.5	42.5	1265.5	1279.8	40.5
1731.3	1690.3	44.5	1324.1	1336.7	42.5
1821.6	1749.3	46.5	1383.2	1392.6	44.5
			1442.7	1447.5	46.5
			1502.2	1501.6	48.5
			1562.3	1554.6	50.5
			1623.5	1606.7	52.5
			1684.0	1657.8	54.5
			1743.0	1707.9	56.5
	$\sigma = 2.78 \times 10^{-2}$			$\sigma = 1.21 \times 10^{-2}$	

bands that the band head moment of inertia, $j_0 = \hbar^2/ab$, are close to each other, $j_0 \sim$ (25-60) $\hbar^2/MeV^{-1}$ and no evidence for odd-even difference is found. Moreover, the smallness of parameter b [~(1 : 3) x 10^{-4}, (Table 1)] implies the super-rigidity of these SD nuclei. The radius of convergence I_r for the I(I+1) expansion of Equation (1)

can be estimated as

$I_r \approx 1/\sqrt{b} \approx 58\text{-}100.$

Conflict of Interests

The author(s) have not declared any conflict of interests.

REFERENCES

Afanasjev AV, Konig J, Ring P (1996). Superdeformed rotational bands in the A~ 140 – 150 mass region. Nucl. Phys. A. 608(2):107-175. http://dx.doi.org/10.1016/0375-9474(96)00272-2, http://dx.doi.org/10.1016/0375-9474(96)00257-6

Becker JA, Roy N, Henry EA, Yates SW, Kuhnert A, Draper JE, Korten W, Beausang CW, Deleplanque MA, Diamond RM, Stephens FS, Kelly WH, Azaiez F, Cizewski JA, Brinkman MJ (1990a). Level spin and moments of inertia in superdeformed nuclei near A~ 194. Nucl. Phys. A. 520:187c-194c. http://dx.doi.org/10.1016/0375-9474(90)91146-I

Becker JA, Roy N, Henry EA, Yates SW, Kuhnert A, Draper JE, Korten W, Beausang CW, Deleplanque MA, Diamond RM, Stephens FS, Kelly WH, Azaiez F, Cizewski JA, Brinkman MJ (1990b). Observation of superdeformation in 192Hg. Phys. Rev. C. 41(1):R9-R12. http://dx.doi.org/10.1103/PhysRevC.41.R9 PMid:9966368

Bently MA, Ball GC, Cranmer-Gordon HW, Forsyth PD, Howe D, Mokhtar AR, Morrison JD, Sharpey-Sahafer JF, Twin PJ, Fant P, Kalfas CA, Nelson H, Simpson J, Sletten G (1987). Intrinsic quadrupole moment of the superdeformed band in 152DY. Phys. Rev. Lett. 59:2141-2144. http://dx.doi.org/10.1103/PhysRevLett.59.2141

Bohr A, Mottelson BR (1975. Nuclear Structure. (Benjamin, Reading, MA, II:4. Draper JE, Stephens FS, Deleplanque MA, Korten W, Diamond RM, Kelly WH, Azaiez F, Macchiavelli AO, Beausang CW, Rubel EC, Becker JA, Roy N, Henry EA, Brinkman MJ, Kuhnert A, Yates SW (1990). Spins in superdeformed bands in the mass 190 region. Phys. Rev. C42:R1791-R1795.

Flannery WH, Teukolsky BP, Vetterling WT (1992). Numerical Recipes in Fortran, (Cambridge University, Second edition, P. 683.

Hu ZX, Zeng JY (1997). Comparison of the Harris and ab expression for the description of nuclear superdeformed rotational bands. Phys. Rev. Lett. 56(5):2523-2527.

Harris SM (1964). Large-spin rotational states of deformed nuclei. Phys. Rev. Lett. 13(22):663-665. http://dx.doi.org/10.2172/4598915

Hegazi AM, Ghoniem MH, Khalaf AM (1999). Theoretical Spin Assignment for Superfeformed Rotational Bands in Mercury and Lead Nuclei. Egypt. J. Phys. 30(3):293-303.

Holmberg P, Lipas PO (1968). A new formula for rotational energies. Nucl. Phys. A117:552-560. http://dx.doi.org/10.1016/0375-9474(68)90830-0

Khalaf AM, El-Shal AO, Alam M, Sirag MM (2002). Spin prediction and Systematics of Moments of Inertia of Superdeformed Nuclear Rotational Bands in The Mass Region A~ 90. Egypt. J. Phys. 33(3):585-602.

Khazov Yu, Rodionov AA, Sakharov S, Singh B (2005). Nuclear Data sheets for A=132. J. Nuclear Data Sheets. 104(3):497-790. http://dx.doi.org/10.1016/j.nds.2005.03.001

Khazov Yu, Mitropolsky I, Rodionov A (2006). Nuclear data sheets for A=131. J. Nuclear Data Sheets 107(11):2715-2930. http://dx.doi.org/10.1016/j.nds.2006.10.001

Laird RW (2002). Quadrupole moments of highly deformed structures in the A~ 100 – 140 region: Probing the Single-Particle Motion in a Rotating Potential. Phys. Rev. Lett. 88:152501. http://dx.doi.org/10.1103/PhysRevLett.88.152501 PMid:11955192

Leoni S, Bracco O, Camera F, Million B, Algora A, Axeisson A, Bezoni G, Bergstrom N, Blasi N, Castoldi M, Frattini S, Gadea A, Herskend B, Kmiecik M, Biano GL, Maj A, Nyberg J, Pignanelli M, Styczen J, Vigezzi J, Zieblinski M, Zucchiatti A (2001). Quantum tunneling of the excited rotational bands in thr superdeformed nucleus 143Eu. Phys. Lett. B498:137-143. http://dx.doi.org/10.1016/S0370-2693(00)01367-8

Sevensson CE (1999). Decay out of the Doubly magic superdeformed band in the N=Z nucleus Z 60n. Phys. Rev. Lett. 82:3400-3403. http://dx.doi.org/10.1103/PhysRevLett.82.3400

Shalaby AS (2004). Spin determination for superdeformed rotational Bands in the A~ 60-90 Mass Region. Egypt. J. Phys. 35(2):221-235.

Shalaby AS, Al-Amry RW, Al-Full Z, Mahrous E (2012). Spin determination and study of the A~ 100-140 superdeformed mass region using three parameter empirical formula. J. Nonlinear Phenomena Complex Syst. 15(1):1-22.

Singh B, Firestone RB, Chu SYF (1996). Table of superdeformed nuclear bands and fission isomers. J. Nucl. Data Sheets 78:1. http://dx.doi.org/10.1006/ndsh.1996.0008

Singh B, Zywina R, Firestone RB (2002). Table of superdeformed nuclear bands and fission isomers. J. Nucl. Data Sheets. 97:241-592. http://dx.doi.org/10.1006/ndsh.2002.0018

Stephens FS (1990). Spin alignment in superdeformed rotational bands. Nucl. Phys. A520:91c-104c. http://dx.doi.org/10.1016/0375-9474(90)91136-F

Szymanski Z (1996). Identical rotational bands in the a~ 130 superdeformed region-analysed in terms of the pseudospin symmetry. Acta Phys. Pol. B27(4):1001-1010. Acta. Phys. Pol. B27:1001.

Twin PJ, Nyako BM, Nelson AH, Simpson J, Bentley MA, Cranmer-Gordon HW, Forsyth PD, Howe D, Mokhtar AR, Morrison JD, Sharpey-Sahafer JF, Sletten G (1986). Observation of a discrete-line superdeformed band up to 60ħ in 152Dy. Phys. Rev. Lett. 57:811-814. http://dx.doi.org/10.1103/PhysRevLett.57.811 PMid:10034167

Wu CS, Zeng JY, Xu FX (1989). Relations for the coefficients in the I(I+1) expansion for rotational spectra. Phys. Rev. C40(5):2337-2341. http://dx.doi.org/10.1103/PhysRevC.40.2337 PMid:9966232

Wu CS, Zeng JY, Xing Z, Chen XQ, Meng J (1992). Spin determination and calculation of nuclear superdeformed bands in A~ 190 region. Phys. Rev. C45(1):261-274. http://dx.doi.org/10.1103/PhysRevC.45.261 PMid:9967752

International Journal of Physical Sciences

Related Journals Published by Academic Journals

- *African Journal of Pure and Applied Chemistry*
- *Journal of Internet and Information Systems*
- *Journal of Geology and Mining Research*
- *Journal of Oceanography and Marine Science*
- *Journal of Environmental Chemistry and Ecotoxicology*
- *Journal of Petroleum Technology and Alternative Fuels*

academicJournals